Gianfredo Romano

Advanced experimental investigation and finite element analysis of rubber friction on model surfaces and rough substrates
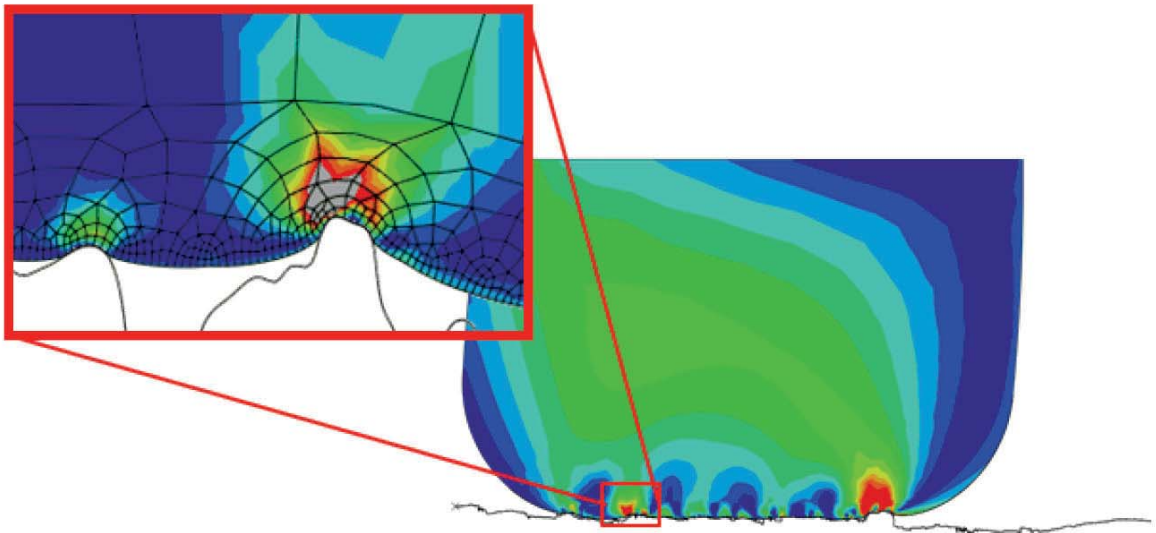
Advanced experimental investigations and finite element analysis
of rubber friction on model surfaces and rough substrates

Advanced experimental investigations and finite element analysis of rubber friction on model surfaces and rough substrates

Von der Fakultät für Maschinenbau
der Gottfried Wilhelm Leibniz Universität Hannover zur
Erlangung des akademischen Grades

Doktor-Ingenieur

genehmigte Dissertation

von

M. Sc. Gianfredo Romano

Geboren am 02.12.1988 in Neapel

2017

Acknowledgement

Firstly, I would like to express my sincere gratitude to my advisor Prof. Dr.-Ing. G. Poll for the opportunity to pursue my Ph.D.

I would like to thank Dr. T. Alshuth and Prof. Dr. M.Klüppel to have guided me throughout the related research, for their patience, motivation, and immense knowledge of rubber technology. I could not have imagined having better supervisors and mentors for my Ph.D study.

Besides my supervisors, I would like to thank the project partners P. Straffi and P. Agoretti for their insightful comments and support, but also for the hard questions which incented me to widen my research from various perspectives.

My sincere thanks also goes to the whole D.I.K staff who gave me access to the laboratory and research facilities, and in particular, the Elastomer Physics department which gave me the opportunity to join their team as intern. Without their precious support it would not be possible to conduct this research.

A special thanks also geos to A. Sarmukaddam and the other colleagues from EDV-Labor for their helpful introduction into the Finite Element Analysis.

I would like moreover to express my sincere thanks to my colleagues and friends M. Ludwig and A. Lang for the stimulating discussions and all the fun we have had together. In particular I am infinitely grateful to A. Lang for the endless support and enlightening me, as a big brother, in both personal and technical aspects. A big part of the work has been possible only thanks to his help.

Last but not least, I would like to thank my family for supporting me spiritually and standing by my side throughout the most important moments of my life.

Abstract

Friction between rubber and rough surfaces is a complex topic which has been intensively studied during the recent years, due to its outstanding potential to realize products which can meet the always more and more demanding technological needs. Nevertheless, a model capable to describe or predict the friction interaction for practical applications is still a big challenge for the scientific community. In this work the fundamentals of rubber friction and contact mechanics have been investigated by use of advanced experimental methods and finite element analysis. The main objective of the thesis has been the hysteresis friction, since, in most cases, it is recognized to be the dominant factor.

Specific friction tests have been developed to clarify the viscoelastic nature of hysteresis friction. The velocity dependence of the friction coefficient has been studied using model substrates, characterized by a regular wavy geometry, and vulcanized rubber compounds. The deformation, occurring in the rubber sample during sliding friction, has been analyzed by optical metrology technique and correlated with the measured hysteresis friction. As a result, a detailed analysis of the correlations existing between friction and geometrical parameters of the substrate has been carried out.

In order to study the effects of different substrate morphologies on hysteresis friction a finite element model has been used. Thanks to finite element analysis a deeper insight into the contributions given by different length scales could be provided. The finite element simulations have been validated by experimental measurements and turned out to be capable to predict the hysteresis friction even in case of rough surfaces.

In the last part, the heat build-up generating in the rubber during sliding due to the viscoelastic losses in case of wet friction has been investigated. The temperature increase, estimated by a theoretical model, proved to be in fair agreement with the IR-thermography, thus confirming the crucial importance of viscoelasticity for a full understanding of rubber friction.

Keywords: rubber friction, contact mechanics, finite element analysis

Kurzfassung

Die Reibung zwischen Gummi und einer rauen Oberfläche ist ein komplexes Thema, das in den letzten Jahren bereits intensiv untersucht wurde. Dennoch stellt die Entwicklung eines allgemein gültigen Modells, mit welchem sich die Elastomerreibung für praktische Anwendungen beschreiben und vorhersagen lässt, noch immer eine große Herausforderung für die Wissenschaft dar. In dieser Arbeit wurden die Grundlagen der Gummireibung sowie der Kontaktmechanik durch den Einsatz modernster experimenteller Methoden in Kombination mit der Finiten-Elemente-Analyse untersucht. Das Hauptaugenmerk war dabei die Analyse und Beschreibung der Hysteresereibung, die in den meisten praktischen Fällen der dominierende Faktor ist. Zum Verständnis des Zusammenhangs zwischen den viskoelastischen Eigenschaften und der Elastomerreibung wurden spezielle Messmethoden eingesetzt. Die Geschwindigkeitsabhängigkeit des Reibkoeffizienten vulkanisierter Gummimischungen wurde zunächst mit Modellsubstraten untersucht. Die während des Reibprozesses auftretende Verformung der Gummiprobe wurde durch optische Messtechnik analysiert. Dadurch konnten die Zusammenhänge zwischen Reibung und den geometrischen Parametern des Substrats detailliert aufgeklärt werden.

Dank der Finiten-Elemente-Analyse konnte ein tieferer Einblick über die Auswirkungen von unterschiedlichen Substratmorphologien auf die Reibung gewonnen werden. Insbesondere die Abhängigkeit der Hysteresereibung von der betrachteten Rauheitsskala konnte durch nummerische Simulationen ausgearbeitet werden. Durch experimentelle Messungen konnten zudem die Simulationsergebnisse validiert und darüber hinaus die Hysteresereibung auch auf rauen Oberflächen vorhergesagt werden.

Im letzten Teil wurde der Wärmeaufbau untersucht, der durch die viskoealstische Verluste im Kautschuk während des Gleitens auf nasser Oberfläche erzeugt wird. Die zuvor durch ein theoretisches Modell abgeschätzte Temperaturerhöhung erwies sich in guter Übereinstimmung mit den experimentell ermittelten Daten, wodurch die elementare Bedeutung der Viskoelastizität für ein vollständiges Verständnis der Gummi Reibung bestätigt werden konnte.

Schlagworte: Elastomerreibung, Kontaktmechanik, Finite Elemente Analyse

Contents

List of symbols and abbreviations

γ	Shear deformation
ε	Strain
ζ	Entropy
η	Viscosity
Θ	Absolute temperature
κ	Thermal diffusivity
λ_0	Wavelength of sinusoidal substrate
$\lambda_1, \lambda_2, \lambda_3$	Principal extension ratio
μ_A	Adhesion friction coefficient
μ_H	Hysteresis friction coefficient
ρ	Density
σ	Engineering stress
τ	Relaxation time
τ_s	Interfacial shear strength
ω	Angular frequency
ψ	Helmholtz energy

A_0	Nominal contact area
A_c	Real contact area
a_T	WLF shifting factor
f	Excitation frequency
F_A	Adhesion friction force
F_H	Hysteresis friction force
F_N	Normal force
G	Shear modulus
G^*	Complex shear modulus
G'	Storage modulus
G''	Loss modulus
H	Height of sinusoidal asperity

I_1, I_2, I_3		First, second, third invariant of the stretch tensor
K		Thermal conductivity
L		Linear momentum
m		Mass
M		Torque
q		Heat flux vector
$\dot{Q}$		Heat rate production per unit time and volume
R		Asperity radius
t		Time
T		Temperature
$tan\ \delta$		Loss factor
u		Internal energy
v		Velocity
V		Volume
v_c		Critical velocity (adhesion friction)
W_F		Friction work

BR	Butadiene rubber
FEA	Finite Element Analysis
FEM	Finite Element Method
HDC	Height difference correlation
NR	Natural rubber
Phr	Parts per hundred rubber
SBR	Styrene-Butadiene rubber
WLF	Williams Landel and Ferry

1.   Introduction and objectives

Friction is the resistance that one body encounters when sliding over another. In many daily activities and in most industrial processes friction plays a key role. Without friction, it would not be possible to walk, grip objects and drive a car, just to mention some of the several common tasks performed every day. On the other hand, in some cases like moving machine parts, bearings, seals etc., reduced friction is desired in order to minimize the energy loss and the consequential heating up that, in the worst case, could even lead to machinery breakdown. In his 1966 report, the father of tribology P. Jost, analysed the role of friction in modern society considering its impact on the economy. He estimated the loss due to tribology ignorance to be about 6% of the USA gross national product. It is clear then that, if high efficiency and quality are to be achieved, friction interactions need to be carefully studied and optimized according to the specific application.

Despite its importance, the prediction of frictional behavior is a far from easy task because of the wide range of variables related to contact mechanics and tribology that involve the disciplines of physics, mechanics and material science. Therefore, friction was a matter of interest already for the ancient civilizations, like the Egyptian, who figured out that the pulling force to drag a heavy slab stone on sand could be dramatically reduced by adding a certain amount of water just in front of the progressing edge. The first documented scientific study concerning friction was done thousands of years later by Leonardo Da Vinci (1452-1519). He measured the force required to move a body on a plane depending on its shape and nature. Experimentally, he found that the friction coefficient, defined as the ratio between the force parallel to the moving direction needed to start the sliding of the body and the normal load acting on it, was independent of the material and always equal to a constant value. Since then, many other scientists and researchers have investigated the friction interaction and demonstrated that, in opposition to Da Vinci's finding, the friction coefficient may strongly vary according to material properties, temperature, nominal contact pressure, sliding velocity, presence of a third medium in the contact, surface roughness and morphology.

Friction is generally classified into the following categories [1] [2] [3]:

- *Dry friction* when contact takes place between two solid surfaces

- *Lubricated friction* is when a lubricant is present between two solid surfaces
- *Fluid (or hydrodynamic) friction* describes the interaction between layers of fluids moving relative to each other
- *Skin friction* is the drag caused by the friction of fluid when a body is moving through it
- *Internal (or hysteresis) friction* is the force resisting the motion between the elements making up a solid material while it undergoes deformation.

Due to the complexity of a system involving all these contributions a general predictive formulation of friction forces does not yet exist and, in many cases, empirical formulations and trial and error testing are still used to estimate friction behavior. The trend in recent years has been to develop models based on more or less sophisticated physical formulations, capable to estimate the friction coefficient for a specific case which can be used by engineers as a guideline during the design phase of new machines and devices. In this way, laborious trial and error procedures as well as rigorous expensive "on site" testing can be minimized.

Of course a detailed understanding of the basic phenomena taking place during the sliding of bodies is required. The aim of the present work is to investigate the fundamental contact mechanics in case of dry and wet friction between a rubber body and a rigid substrate with specific emphasis on the effects of both substrate morphology and compound properties. The friction interaction was investigated using innovative experimental techniques, analytical physical approach and computational modeling.

The thesis is structured as follows:

In chapter 1, an overview of rubber properties is provided, with a special focus on mechanical behavior and viscoelasticity, since they are a prerequisite to understand friction mechanisms. The main features of the polymers used for the investigation will be also briefly described.

The state of the art for rubber friction is introduced in chapter 2, whit an overview of the most acknowledged friction theories. The mechanisms involved in rubber friction will be presented and a particular interest is given on hysteresis and adhesion.

In chapter 3 an introduction to continuum mechanics with respect to finite elements analysis is reported. The constitutive material models used for the investigation will be then described together with the numerical implementation of viscoelasticity. The contact mechanic algorithms used to calculate friction interactions is given in the same section.

In chapter 4, the materials and methods used for the experimental investigation will be presented, with a particular interest in optical analysis and finite elements modeling.

Chapter 5 deals with the results and their discussion. The first part will concentrate more on the mechanical characterization of the compounds and friction measurements in case of sinusoidal model substrates. In the second part, a deep analysis of hysteresis friction for both sinusoidal and rough model substrates by use of finite element analysis will be presented. The simulations will be finally compared with experimental measurements.

In chapter 6, the results will be summarized in conclusion of the work.

1.1. Elastomers and general properties

Rubber is a generally soft material characterized by a remarkable elasticity, namely the ability to recover its original shape and dimensions after being substantially deformed. Rubber is not only elastic, but also resilient, resistant to tearing, waterproof and a good electrical and thermal insulator. All these properties make rubber a very interesting material capable of fulfilling a huge number of engineering requirements. Rubber materials are polymers, which are high molecular weight compounds consisting of long chains of one or more types of molecules, the monomers. Consequently, the name elastomer (elastic polymer) is commonly used as a synonym for rubber.

One should point out that all the above mentioned characteristics are related to rubber at room temperature, which is the most common environmental condition. In case the material is cooled down below a certain temperature, rubber becomes harder and brittle, like glass. For this reason such a temperature, which for rubber is typically below zero degree, is called glass transition temperature, or in short Tg. This transition is something that only happens to polymers and makes them unique materials.

Nowadays there are several types of rubber available, each of them showing different features. The type of rubber with the longest history of use is polyisoprene, the constituent of natural rubber (NR), which is the concentrated and purified form of latex extracted from a tree, most usually the Hevea Brasiliensis, cultivated in tropical regions, mostly South East Asia. In the 1940s several synthetic rubbers were developed to provide an alternative to natural rubber. The ones used most are styrene-butadiene rubber (SBR) and polybutadiene rubber (BR), which are derived from the synthesis of petroleum and natural gas products. The process of synthesis often consists in a free radical emulsion polymerization, whereby a vinyl monomer is polymerized by itself or combined with another monomer to create a high molecular weight polymer. In recent years, the anionic polymerization in solution with use of alky lithium catalysts has become very important to manufacture SBR, which in this case is known as S-SBR, and is widely used in the tire industry.

Although historically natural latex has always enjoyed a cost benefit advantage over synthetic versions, the great advantage of synthetic rubbers is the possibility to obtain products with specifically tailored properties. Hence, a clear comprehension of rubber molecular structure is essential for an understanding of its physical properties.

1.1.1. Natural rubber (NR)

The rubber hydrocarbon component of NR consists of over 99.99% of linear cis-1.4 polyisoprene (Fig. 1.1) and its average molecular weight ranges from 200,000 to 400,000 with a relatively broad molecular weight distribution [4]. As a result NR has a peculiar processing behavior.
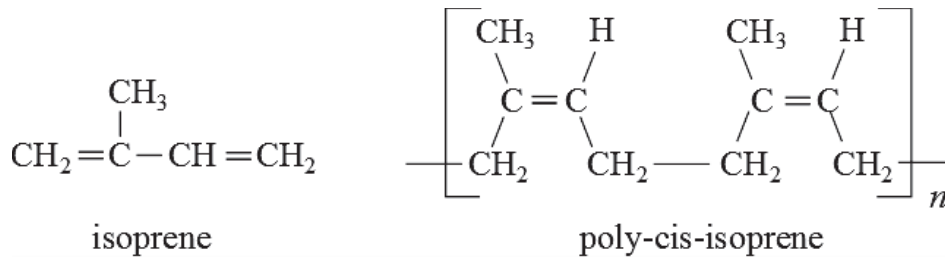

Fig. 1.1: Chemical structure of isoprene and poly-cis-isoprene which is the main constituent of natural rubber.

The double bonds present in the isoprene unit are reactive group for vulcanization reactions with sulphur, but double bonds can also react readily with oxidizing agents, like oxygen and ozone, thus making NR very sensitive to oxidations processes which can significantly degrade its properties (aging). In order to obtain a good aging resistance it is necessary to use protective agents in the compound, and use thiazol accelerators in short cure cycles with not too high temperatures. Nevertheless, even under optimum conditions, the aging and heat resistance of NR vulcanizates does not reach that of most SBR and BR vulcanizates.

Concerning its compounding, NR is too hard to be directly processed and therefore it has to be masticated first. The mastication process consists of high shear mixing under the influence of small amounts of oxygen. In this way a scission of polymer chains takes place and the molecular weight is broken down to facilitate the processing of the material [5]. NR vulcanizates show very interesting mechanical properties [6]. In particular, when NR is stretched more than 80 % of its original length, crystallization occurs due to the orientation of the polymer chains (strain crystallization). As a consequence a high tensile strength is observed along the axis of deformation, about 20 MPa or more, contrary to most

types of synthetic rubbers [7] [8]. The ultimate elongation is generally about 500 to 1000 %.

NR is suitable for dynamic applications since it is characterized by low heat build-up and high elasticity. Moreover, tear resistance is also influenced by strain crystallization and is therefore very good, as well as the dynamic fatigue resistance [9] [10].

Being non-polar, NR can be easily blended with a great number of other non-polar rubbers. Blends with SBR and BR are intensively exploited. In this case a product which exhibits both high performance of NR and synthetic rubbers can be obtained [11]. Because of this and the all above mentioned properties NR results to be indispensable in several applications, despite the availability of a great number of synthetic rubbers.

1.1.2. Butadiene rubber (BR)

Butadiene Rubber (BR) is composed of butadiene units which can have joined linearly by 1.4, as well as by 1.2-addition, see Fig. 1.2. The average molecular weight of commercial BR is in the range of 250,000 to 300,000. The microstructure can be strongly influenced by the catalysts using during the polymerization. More specifically, the higher is the cis-1.4 content of BR, the lower is its glass transition temperature, T_g. The T_g raises linearly as the concentration of 1.2 structure (vynil content) increases (see Fig. 1.4) [12]. The ratio between 1.2 and 1.4 content determines also the material performances in terms of abrasion resistance, wet grip and tensile strength. In particular, as 1.2 content increases the abrasion resistance becomes poorer while wet traction improves. Hence, a compromise needs to be found based on the specific case.
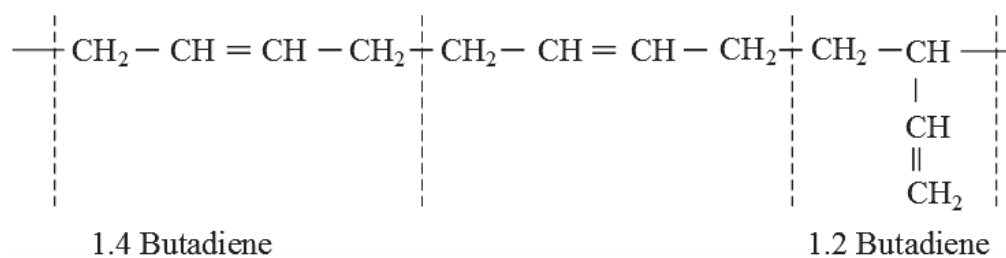

Fig. 1.2:   Chemical structure of BR.

The tensile strength of vulcanizates from BR with high cis-1.4 is considerably lower than that of comparative SBR and NR vulcanizates. However, in blends with them BR can satisfy technically demanding properties for high quality products.

1.1.3. Styrene-Butadiene rubber (SBR)

SBR is a general purpose synthetic rubber, produced from the copolymerization of styrene and butadiene, as illustrated in Fig. 1.3. The styrene content ranges usually from about 20 to 40 %.
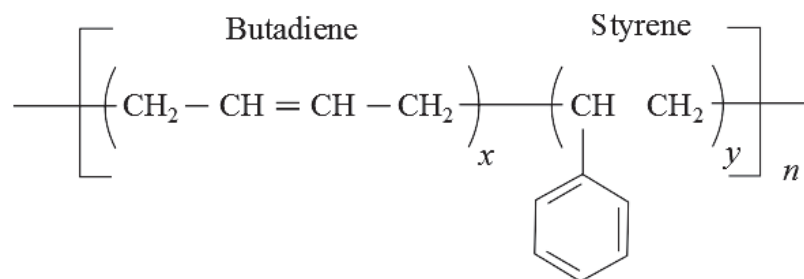
Fig. 1.3:   Chemical structure of SBR.

The largest share by far of SBR is produced in emulsion (E-SBR) using redox initiators, but solution SBR (S-SBR) is steadily gaining in importance [13]. In case of E-SBR the small difference of chemical reactivity between styrene and butadiene implies that the monomers are statistically arranged along the polymer chain. The butadiene unit can be present in different configurations, as in the case of BR, according to the polymerization temperature. As a consequence material properties, like the Tg can be strongly affected by the overall arrangement of the copolymer micro structure. The strongest influence is given by the styrene content. As the styrene content in the SBR increases, the glass transition temperature becomes higher, while abrasion resistance and resilience become smaller (see Fig. 1.4). A similar effect is induced by varying the amount of vinyl groups. Good dynamic properties, aging and heat resistance as well as abrasion resistance make SBR product of high versatility for many technological application.

Fig. 1.4:   Dependence of the glass transition temperature on the styrene and the 1.2-component of BR. Several cases of synthetic rubbers are reported as example (from [14]).
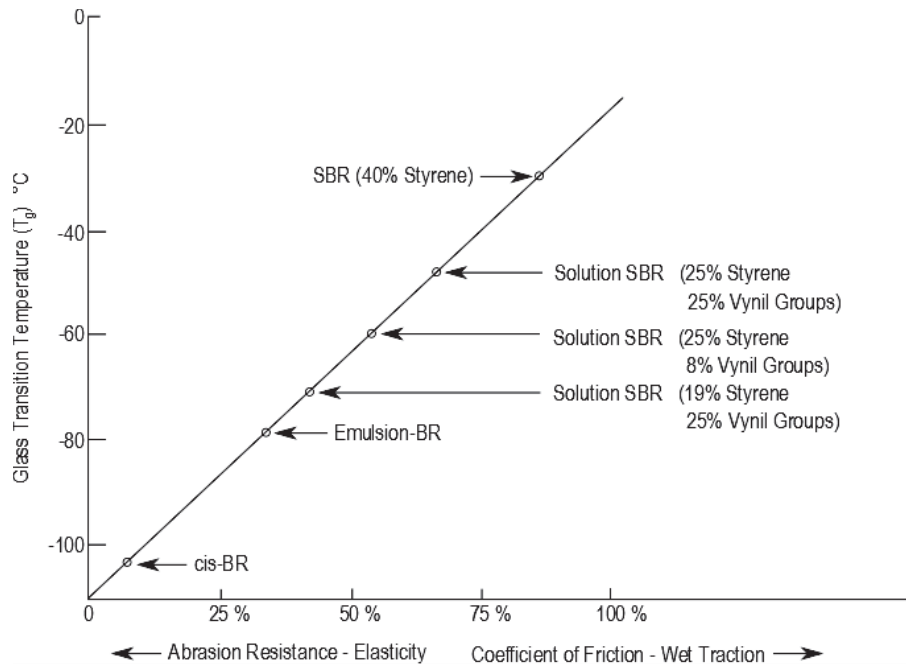
Compared with E-SBR, S-SBR has the advantage to be produced in stereospecific combinations thanks to catalysts based on organo-metallic compounds. This means that is possible to obtain a custom-made SBR with a wide range of specific properties by choosing appropriate polymerization systems and conditions. Thus for high performances products S-SBR is usually preferred to E-SBR [15].

1.1.4.   Vulcanization and filler reinforcement

In raw state, both natural and synthetic rubber show poor mechanical properties, as they are brittle when cold and become sticky when hot. Therefore crude rubber is not suitable for most applications we know nowadays. Thanks to the so-called vulcanization process, discovered in 1839 by Goodyear, mechanical properties and thermal stability can be improved [16] [17]. During a typical vulcanization process, sulfur together with various chemical additives is added to raw rubber and the mixture is then heated. Sulfur atoms create a series of chemical links between the intricate network of polymer chains [18]. Such cross-links prevent the slippage of the randomly coiled polymeric chains, thus giving the

material increased elasticity and stiffness as well as better resistance to heat, cold, abrasion and oxidation. This process is also called crosslinking or curing.

The vulcanization reaction is determined in large measure by the type of vulcanizing agents, the temperature and time. The number of crosslinks formed, also referred to as crosslink density or degree of vulcanization, has an influence on the final properties of rubber vulcanizates [19] [20].

For nearly all engineering applications a reinforcing filler, usually carbon-black or silica, is added to give to the rubber compound the desired mechanical properties. Tensile strength, abrasion resistance and tear resistance can be strongly improved by the interaction between rubber and filler [21].
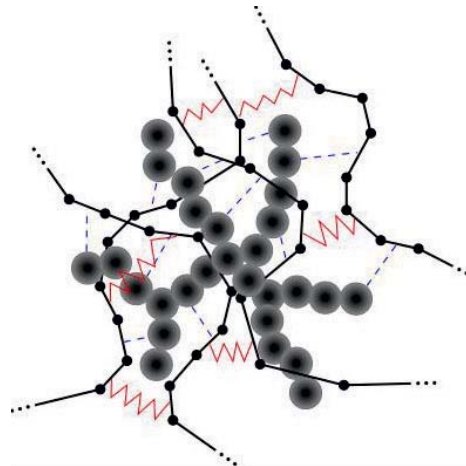
Fig. 1.5: Microstructure for a filled rubber vulcanizate. Grey circles: filler particles. Black lines: polymer chains. Blue dashed lines: Filler-Polymer interaction. Red zigzag lines: crosslinks.

The fine filler particles form a structure within the material leading to both physical and chemical bonds with the polymer chains after vulcanization (see Fig. 1.5.). Such a structure acts like a stiff network which provides increased strength to the rubber compound [22]. Hardly any filler will enhance all mechanical properties at the same time to the same optimal degree. In order to obtain the desired reinforcing effect the filler-rubber interaction and the filler structure must be considered. As an example, the activity of fillers in BR, SBR is often quite more pronounced because of their lack of strain crystallization than in NR [23]. In addition to this the chemical composition and the structure of the filler's surface are of importance as they influence the interaction with the polymer chains [24]. Therefore

the quantity and the type of filler, to be added to the rubber compound, must be carefully selected in order to achieve a product featuring the desired properties.

1.2. Mechanical properties of elastomers

As already mentioned, rubber consists of many polymer molecules interpenetrated with each other, thus, strong limitations of mobility occur, especially for translational motions of molecular center of gravity. Usually, the microstructure of a polymeric material is visualized as a spaghetti coil. The main effect which determines the mechanical behavior of such a system under an external force is the presence of entanglements, which tie the spaghetti together and prevent large movement when loads are applied [25]. In Fig. 1.6 a schematic representation of an entanglement, between two macromolecules with linear chain, is shown.
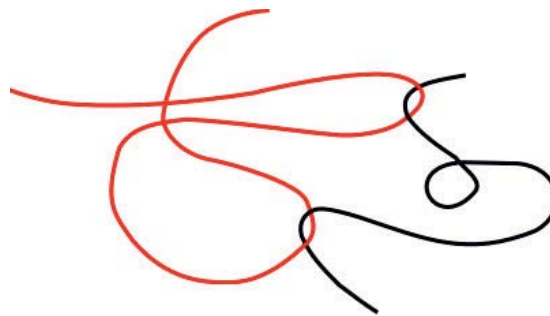
Fig. 1.6:   Example of entanglement between molecular chains.

Such bond between chains has nothing to do with the chemical covalent bond. These bonds are merely physical and can reform in other places keeping its effect just from a statistical point of view. The polymer chain result then confined in a tube-like structure by all the entanglements [26] [27]. Based on the time scale any chain can disentangle from its neighbours by slipping along the tube and therefore a macroscopic flow of material is sometimes observed [28].

This special micro-structure is responsible of the particular and complex mechanical behavior of elastomers at macroscopic scale. In the undeformed state the long polymer chains, entangled and, in case of cured rubber, crosslinked with each other, are arranged in a high entropy random coil configuration [29]. When external stresses are applied, the

equilibrium end-to-end distance of the chains changes, and they thus adopt a less probable conformation. The consequential reduction of entropy generates retraction forces trying to bring the chains back to their original unstretched state as illustrated in Fig. 1.7 [30].

Fig. 1.7:   Changes of the rubber network upon stretching. Red dots represent crosslinks.

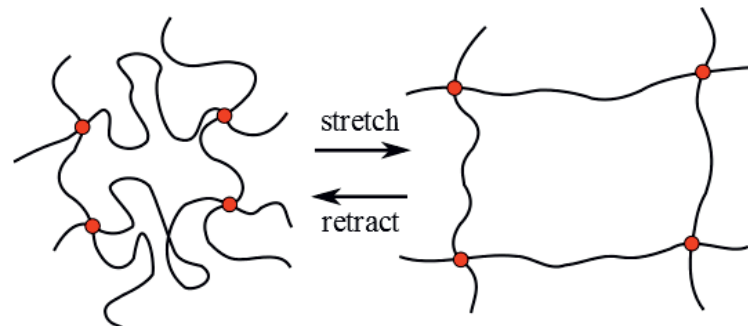Continuing stretching the rubber, chain segments approach their extensibility limit and uncoiling is prevented thanks to the crosslinks action. If further tension is applied, the stresses will be carried directly on the C-C polymer bonds and an increase of stiffness is usually observed in the ultimate branch of the stress-strain curve. When the force becomes great enough, the C-C bonds will break and rubber will snap [31]. Even if rubber strength is comparable with other materials, the stiffness is lower and the extension range is much larger. The latter, however, may significantly vary according to the number of crosslinks and the chemical structure of the polymer chains. A typical value of the Young's Modulus for a vulcanized rubber is around 1 MPa and a general trend of the stress-strain behavior is depicted in Fig. 1.8. During a deformation loop, the loading and the unloading curve follow a different path because the energy introduced into the system is partially dissipated. This phenomenon is known as hysteresis and the area between the curves, the hysteresis loop, is equal to the dissipated energy per unit volume [32]. This mechanical behavior, characteristic for rubber materials can be explained considering that micro-slippages and breaking of weak chains or crosslinks (as well as filler-rubber network in case of filled rubber) occur at a high stage of deformation, resulting in energy dissipation, or to be precise, in a transformation of mechanical energy into heat energy.

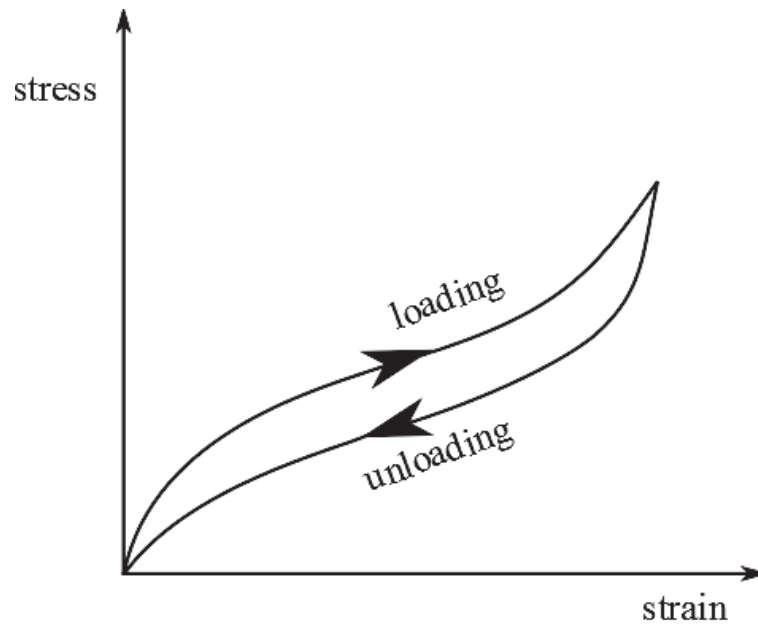Fig. 1.8:   Typical stress-strain behaviour for rubber materials. The different path
            followed by the loading and unloading curve is known as hysteresis.

This means that, in reality, rubber does not show an ideal elastic behavior and if subjected to a certain stress, its mechanical response is a combination of an elastic solid and a viscous fluid, thus the term viscoelastic [33] [34].

1.2.1. Dynamic-mechanical properties

Whenever rubber is subjected to dynamic solicitations its dynamic mechanical behavior plays a crucial role. One typical example is the pneumatic tire, where three of the main tire properties (wet traction, wear resistance, rolling resistance) strongly depend on the dynamic mechanical properties of the tread compound [35] [36] [37]. If dynamically excited, rubber behaves both like an elastic solid and a viscous fluid, thus the term viscoelastic. Viscoelasticity is undoubtedly one of the properties which characterizes the complexity and peculiarity of rubbers. Since models which can describe in a proper way rubber viscoelasticity would require very complex mathematical formulations, in most cases the approximation of linear viscoelasticity is used

1.2.1.1.   Linear viscoelasticity

Linear viscoelasticity can be applied to viscoelastic solids which do exhibit time dependent mechanical properties but independent of the strain amplitude. In order to better understand this special behavior, one might consider the case of a body undergoing a dynamic oscillatory excitation, where the material is subjected to sinusoidal strain and its consequential stress response is analyzed. In particular, let us consider a sinusoidal shear deformation $\gamma(t)$ with angular frequency ω_0:

$$\gamma(t) = \gamma_0 \, sin(\omega_0 t) \tag{1}$$

Where t and γ_0 are time and maximum amplitude of the strain, respectively. The shear stress response $\sigma(t)$ can vary depending on the material properties, as shown in Fig. 1.9. For an elastic material Hooke's law applies, and the stress is proportional to the strain (Fig. 1.9.a):

$$\sigma(t) = \sigma_0 \, sin(\omega_0 t) \tag{2}$$

Elastic solids have, in fact, a well-defined shape and reach a new form of equilibrium when deformed by external forces. This kind of material stores all the energy coming from the work done by the external forces during deformation and this energy is then available to return the solid to its original shape after the removal of external forces. Unlike elastic solids, viscous fluids do not have a definite shape and flow irreversibly under application of external forces. For such materials the stress response is 90° out of the strain phase (Fig. 1.9.c).
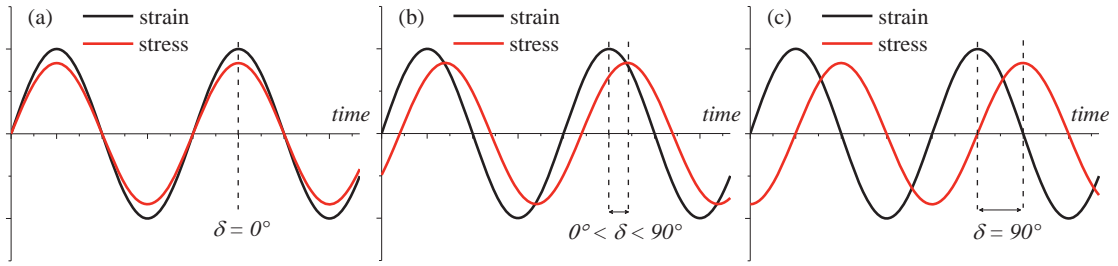
Fig. 1.9:   Examples of phase angle present between stress and strain during cyclic excitation for different materials: (a) 100% elastic; (b) visco-elastic; (c) 100% viscous.

Rubber, as already mentioned, is viscoelastic, thus exhibits an intermediate phase difference δ (Fig. 1.9.b) [31]:

$$\sigma(t) = \sigma_o \sin(\omega_0 t + \delta) = (\sigma_o \cos \delta) \sin \omega_0 t + (\sigma_o \sin \delta) \cos \omega_0 t \qquad (3)$$

If we consider $G' = (\sigma_o / \gamma_o) \cos \delta$ and $G'' = (\sigma_o / \gamma_o) \sin \delta$, Eq. (3) becomes:

$$\sigma(t) = \gamma_o (G' \sin \omega_0 t + G'' \cos \omega_0 t) \qquad (4)$$

Thus, the overall response $\sigma(t)$ can then be understood as the sum of two contributions: the first, in phase with the deformation, due to the elastic component of the material; the second, out-of-phase of 90°, due to its viscous component. The terms G' and G'' are defined as storage modulus and loss modulus, respectively.

The ratio between the loss and storage moduli (G''/G') gives the useful quantity known as the loss factor, $\tan \delta$, which is a measure of the amount of deformational energy that is dissipated as heat during each cycle.

The relationship between these quantities can be illustrated by means of an Argand diagram (see Fig. 1.10), commonly used to visualize complex numbers, which shows that G' and G'' represent the real and imaginary components of the complex modulus G^* and δ is the phase angle in between:

$$\left| G^* \right| = \left| G' + iG'' \right| = \sqrt{\left| G'^2 + G''^2 \right|} \qquad (5)$$
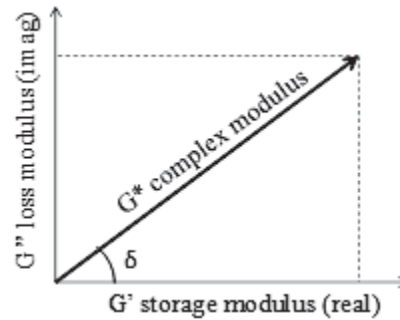
Fig. 1.10: Argrand diagram for dynamic moduli.

The reasoning made so far for the shear modulus applies in an analogous manner to the tensile modulus *E*. The relation between shear and tensile moduli can be defined trough the following equation:

$$E = \frac{G}{2(1+v)}$$

(6)

Where v is Poisson's coefficient, which for rubber is close to 0.5 as it is almost incompressible.

1.2.1.2.   *Linear viscoelastic models*

One convenient way to deal with linear viscoelasticity is to consider models consisting of a suitable combination of elastic springs and viscous dashpots, so that the time dependent behavior can be expressed by means of a constitutive equation. The constitutive equation for a linear viscoelastic solid must possess the following mathematical properties:

- Linearity: linear superposition of stress or strain, known as Boltzmann superposition principle;
- Continuity: continuity between stress and strain;
- Translation-invariance: the behavior of the material remaining invariable with time;
- Non-retroactivity: identical histories in a material producing identical states of stress-strain in the material.

More specifically, springs are characterized by the elastic constant *G*, therefore the stress strain relationship, in line with Hooke's law, is:

$$\sigma = G\gamma$$

(7)

Where σ is the stress and γ is the strain that occurs under the given stress. The viscous component, on the other hand, can be modeled as dashpots. The stress-strain rate relationship of such elements obeys Newton's viscosity law:

$$\sigma = \eta \frac{d\gamma}{dt} \tag{8}$$

Where η is the viscosity of the material, and $d\gamma/dt$ is the time derivative of strain [38].

Based on the arrangement of springs and dashpots we may have different models to reproduce typical viscoelastic phenomena like creep or stress relaxation [39].

The Maxwell model can be represented by a purely viscous damper and a purely elastic spring connected in series, as shown in Fig. 1.11 [40]. When a load is applied, the stress is the same in both elements, while the overall deformation γ_T is equal to the sum of γ_D and γ_S, where the subscripts D and S stand for dashpot and spring respectively.

The model can be represented by the following equation:

$$\frac{d\gamma_T}{dt} = \frac{d\gamma_D}{dt} + \frac{d\gamma_S}{dt} = \frac{\sigma}{\eta} + \frac{1}{G}\frac{d\sigma}{dt} \tag{9}$$

So, if the material is kept under constant strain, the stress gradually relaxes with the following exponential law [39]:

$$\sigma(t) = \gamma_T G \exp(-t/\tau) \tag{10}$$

The time required to reach the stress relaxation of the element is then called relaxation time and is equal to $\tau = \eta/G$.
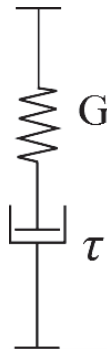
Fig. 1.11: Schematic representation of the Maxwell model.

The Maxwell model predicts that the stress decays exponentially with time, which is accurate for most polymeric materials like rubber, but its limitation is that it does not predict creep accurately [41]. In fact, under constant stress, the strain has two components: an elastic component that occurs instantaneously, plus a viscous component that grows linearly with the time in which the stress is applied.

If the viscous damper and the elastic spring are arranged in parallel the so called Kelvin–Voigt model, also known as the Voigt model, is obtained, as shown in Fig. 1.12. In this case when a load is applied, both elements experience the same deformation while the total stress is the sum of the stresses in each element [39].

Fig. 1.12: Schematic representation of the Kelvin–Voigt model.

The constitutive relation is expressed as a linear first-order differential equation:

$$\sigma(t) = G\gamma(t) + \eta \frac{d\gamma(t)}{dt} \tag{11}$$

This model represents a solid undergoing reversible, viscoelastic strain. Upon application of a constant stress, the material deforms at a decreasing rate, asymptotically approaching

25

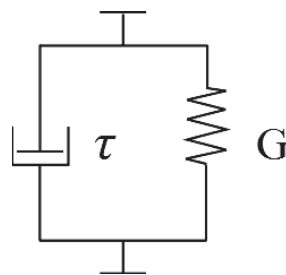the steady-state strain equal to σ/G as time approaches infinity. When the stress is released, the material gradually relaxes to its undeformed state in agreement with the behavior typically shown by elastomers. Therefore, the model is extremely good to predict creep in materials, but contrary to the Maxwell model, the relaxation response is not well predicted.

However, the simple models mentioned above, featuring a single exponential response function, do not well approximate the behavior of real rubber materials. Specifically, a single exponential relaxation function undergoes most of its relaxation over about one decade in time scale, while real materials relax or creep over many decades. Hence, the representation of the behavior for most viscoelastic materials requires models with a large number of elements. Such models can be derived from the extension or generalization of the Maxwell and Voigt models. One of the most frequently used models in polymer physics is the generalized Maxwell model where a finite number of Maxwell elements are arranged in parallel with an elastic spring (Fig. 1.13) [42]. This group of elements represents a discrete spectrum of relaxation times, each time τ_k being associated with a spectral strength G_k. Since in a parallel arrangement, forces or equivalently stresses are additive, it is possible to obtain the overall stress response considering the sum of N Maxwell elements [43]

$$\sigma(t) = G_\infty \gamma_T + \sum_{k=1}^{N} G_k \exp(-t/\tau_k)\gamma_T \tag{12}$$

Where G_∞ is the long-term modulus, obtained after a period of time long enough to reach all dashpots relaxation.
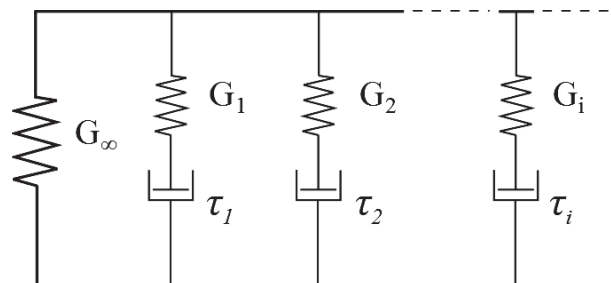

Fig. 1.13:   Schematic representation of the generalized Maxwell model.

The formulations valid for the time dependent behavior apply at the same manner for dynamic oscillatory test. In fact, although sometimes a distinction is made between stress relaxation and dynamic tests, in reality, they both depend on the same viscoelastic principles. Therefore the transition to one aspect to the other is every time possible using the Fourier transform and its inverse, respectively defined as:

$$\Im\{f(t)\} = \bar{f}(i\omega) = \int_0^\infty e^{-i\omega t} f(t) dt \tag{13}$$

$$\Im^{-1}\{\bar{f}(i\omega)\} = f(t) = \frac{1}{\pi} \int_0^\infty e^{i\omega t} \bar{f}(i\omega) d\omega \tag{14}$$

Such Fourier transform pair, indeed, allows the conversion from time to frequency domain and vice versa. Therefore, applying Eq. (13) to (12) the analytical form of the complex modulus, as a function of the angular frequency, for a viscoelastic solid whose constitutive equation is based on the generalized Maxwell model can be obtained [44]:

$$G^*(i\omega) = i\omega \int_0^\infty \left[G_\infty + \sum_{k=1}^N G_k e^{-t/\tau_k} \right] e^{-i\omega t} dt =$$

$$= i\omega \left[G_\infty \int_0^\infty e^{-i\omega t} dt + \sum_{k=1}^N G_k \int_0^\infty e^{-\left(\frac{1+i\omega\tau_k}{\tau_k}\right)t} dt \right] \tag{15}$$

Solving the integrals the complex modulus becomes:

$$G^*(i\omega) = G_\infty + \sum_{k=1}^N G_k \frac{i\omega\tau_k}{1+i\omega\tau_k} =$$

$$= G_\infty + \sum_{k=1}^N G_k \frac{\omega^2\tau_k^2}{1+\omega^2\tau_k^2} + i\sum_{k=1}^N G_k \frac{\omega\tau_k}{1+\omega^2\tau_k^2} \tag{16}$$

According to Eq (5), the real and the imaginary part of Eq. (16) represent the expressions for the storage and loss modulus, respectively, in dependence of the excitation frequency. This transformation will be useful for the derivation of material parameters necessary to perform finite element simulations.

However, it should not be forgotten that this model is valid only for linear viscoelastic materials, but in reality storage and loss modulus are significantly varying with strain

amplitude. Moreover, the time scales as well as the frequencies of excitation depend on the temperature at which the rubber body is working. An insight into these aspects will be therefore presented in the next sections.

1.2.2.   Frequency and temperature dependence

The dependence of dynamic moduli on the frequency, or time, at which the strains are applied, results from the chain and the segment mobility in rubber compounds [43]. At low frequency, all rubber polymer chains are capable of following deformation without delay and the energy loss during one cycle of deformation is low [27]. As the frequencies of strain increase, the polymer entanglements are no longer able to follow the strain during one cycle of deformation. As a result, entanglements act as crosslink points, thus implying an increase in the elastic modulus [45]. Based on the excitation frequency, some defined zones or regions can be distinguished to describe the behavior of the storage and loss modulus for a rubber compound, as shown in Fig. 1.14 [46].

In the plateau region, a constant storage modulus and the minimum loss modulus can be seen since many movements are still possible on the micro scale and, therefore, an almost ideal elastic behavior is still taking place. After the rubber plateau region, with further frequency increase, rubber compounds reach the transition state between the rubbery state and the glassy state, corresponding to restricted polymer mobility in comparison with the low frequency state. Finally, rubber compounds reach the glassy state, so-called because rubber behaves like a glassy material. In this region, polymer chains are unable to move flexibly enough to follow the applied strain rate, except for small local polymer chain motions, resulting in a very high plateau of the storage modulus, and the energy dissipation is very high.
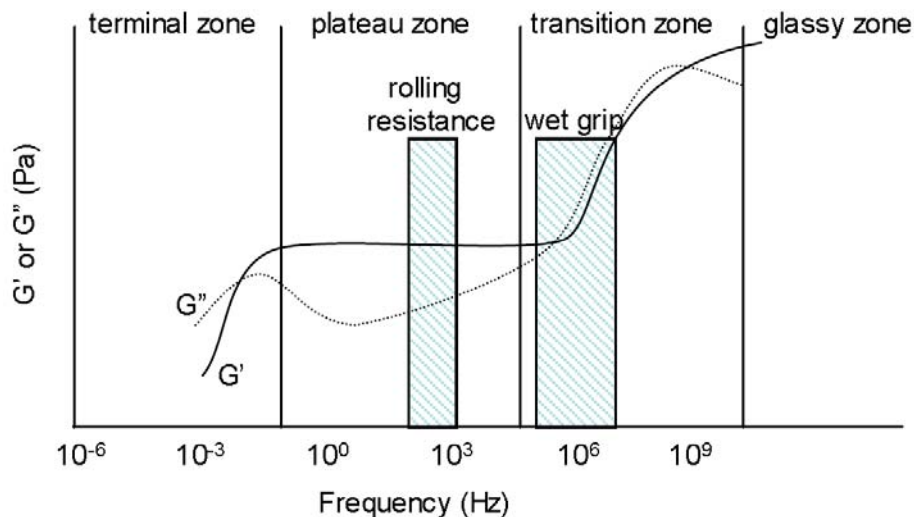
Fig. 1.14: Frequency dependence of shear storage modulus G' and loss modulus G" for
            a typical visco-elastic polymer from [47] [48].

This behavior of rubber has direct consequences on tire performance (Fig. 1.14). In fact, the rolling resistance is related to the loss tangent of rubber compounds in the low frequency region within the rubbery state [49] [50]. This low frequency region more or less corresponds to the typical angular velocity of a rolling tire. It is generally known that a lower loss tangent at low frequency leads to lower rolling resistance. On the other hand, wet traction is related to the loss tangent at high frequency. In most cases, the higher the loss tangent at high frequency, the higher is wet traction [34].

On the other hand, it is well known that viscoelastic processes are strongly dependent on temperature and that a relation exists between frequency and temperature in dynamic measurements. The reason for this that an increase in temperature at a given frequency results in an increase in the free volume and that in turn implies higher polymer chain mobility. Therefore, rubber behaves very similarly to the conditions of low-frequency stress. At very low temperature instead, rubber is in a condition of "frozen" molecular structure as in case of very high frequency. Thus, it can be concluded that a temperature change is consequently equivalent to a change in inverse frequency and a shifting of the viscoelastic behavior is produced along the frequency axis, whenever a temperature change occurs (Fig. 1.15).
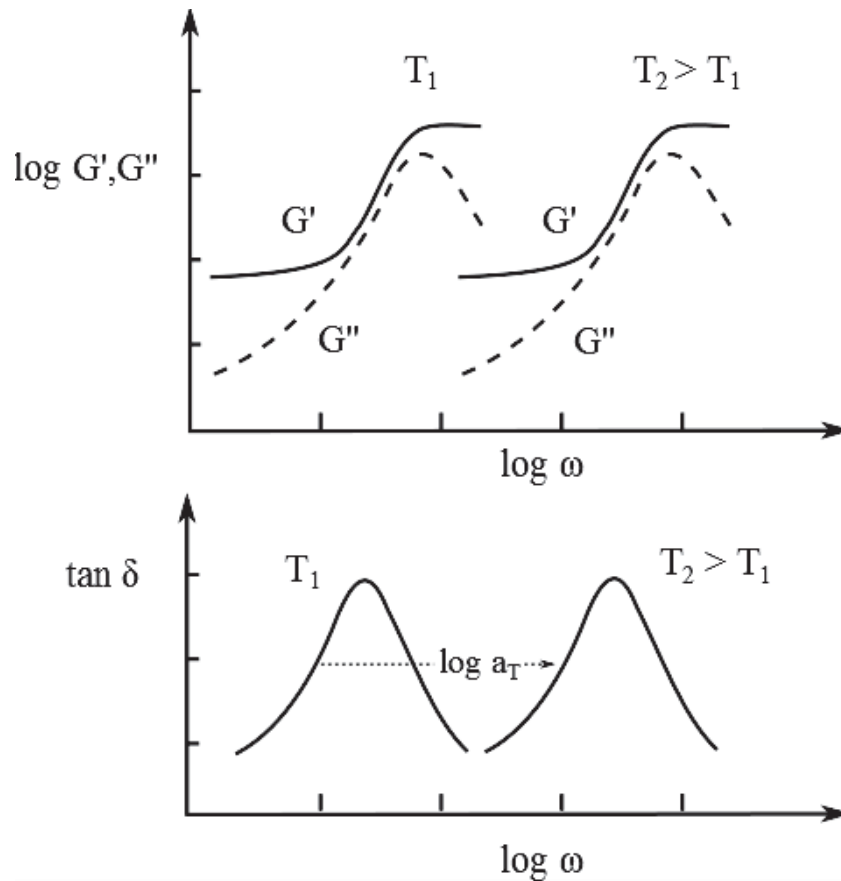
Fig. 1.15: Dynamic properties of rubber as a function of frequency and temperature. The curves are displaced along the frequency axis by a distance log a_T given by the WLF relation. Adapted from [35].

Thanks to this correlation, it is possible to extrapolate the viscoelastic properties for a frequency range much larger than the one which could be investigated using any equipment at a defined temperature. In particular, by using the so called time-temperature superposition (or frequency-temperature superposition), measurements can then made over a limited frequency range at many different temperatures to be then superimposed by horizontal shifts along the logarithmic frequency axis to construct a "master-curve", representing the expected response over an extremely wide frequency range at the chosen reference temperature. The degree of horizontal shifting required to shift a given set of data can be mathematically described with respect to temperature. The model commonly used is the well-known Williams-Landel-Ferry (WLF) equation [51]:

$$\log a_T = \frac{-C_1(T-T_0)}{C_2+(T+T_0)} \tag{17}$$

In this equation, T_0, is the reference temperature at which the mastercurve is evaluated, C_1 and C_2 are constants, T is the measurement temperature, and a_T is the shift factor. A WLF time-temperature superposition can be applied to most polymers in a temperature range between Tg and Tg + 100°C [52]. An example of mastercurve construction is shown in Fig. 1.16.
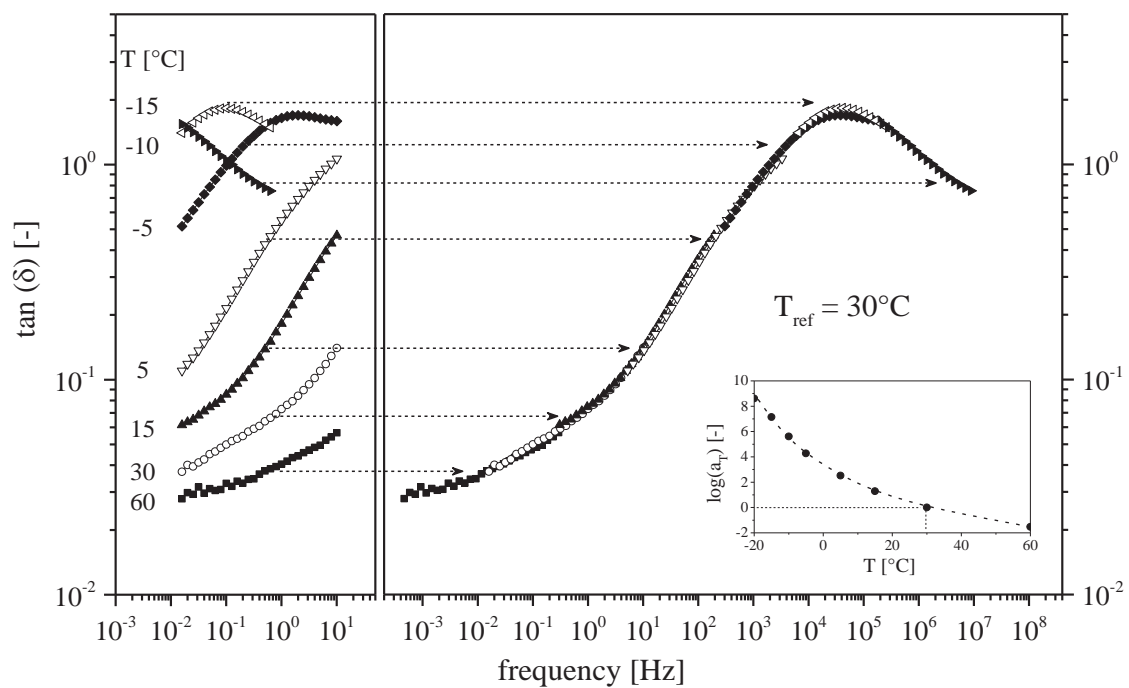
Fig. 1.16: Example of mastercurve construction for a SBR rubber. Reference temperature 30°C. In the insert the shifting factor as a function of the temperature is shown.

1.2.3. Payne effect

The strain amplitude dependence, also known as the Fletcher-Gent or Payne effect [53] , is generally not as well-known as the time-temperature dependence, although in many cases this effect can be of the same importance. The effect of the amplitude dependence for a harmonically loaded rubber is illustrated in Fig. 1.17. As can be seen in this figure, a constant value for the modulus is observed only for very small strain amplitudes, but, when the strain is increased (about 0.5-1%), the storage modulus decreases up to a strain level as around 15-20%. For higher amplitudes, a plateau-like behavior is observed again. The damping factor, on the other hand, generally shows a peak generally in the range between 1 and 10 % of strain, thus confirming that the strain amplitude has a different effect on G' and G''.

Fig. 1.17:   General strain amplitude dependence of dynamic shear modulus and damping for a filled rubber.

The entity of the modulus variation depends on the type and amount of filler. From a micro-mechanical point of view, the amplitude dependence is traditionally attributed to the breakdown and reforming of the filler structures and it is fully reversible [54].

1.2.4.   Mullins effect

The Mullins effect can be considered as an instantaneous and irreversible softening of the stress-strain curve occurring 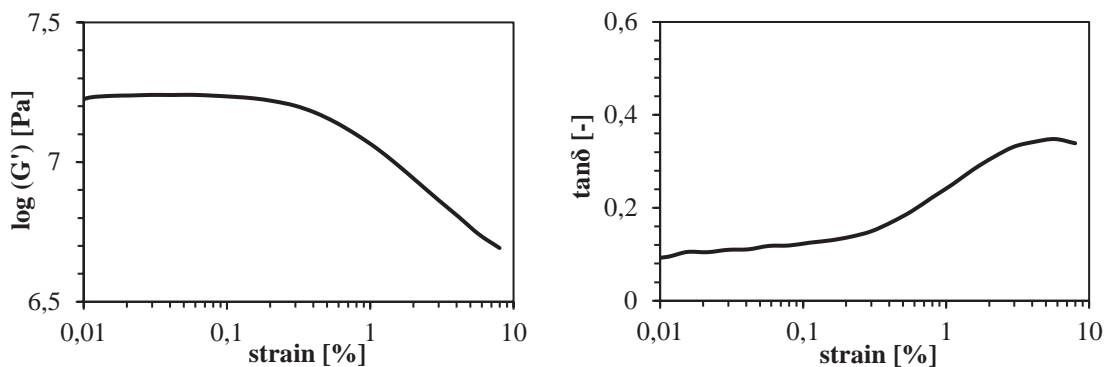whenever the load increases beyond its prior all-time maximum value, as illustrated in Fig. 1.18 [55]. In case of a cyclic load, the Mullins effect is a reduction in the stiffness measured during the first few load cycles. Repeated stretching produces successively smaller effects, indicating an approach to an equilibrium stress/strain curve. This is often referred to as "mechanical conditioning" of the rubber. The origins of this mechanism are not yet completely clear. Some author explain it on the basis of a breakdown or slippage and disentanglements of bonds between filler and rubber [56] [57] [58], some others with strain induced crystalllization-decrystallization [59] [60] or rearrangement of network chain junctions in filled systems [61].

Contrary to the Payne effect, Mullins effect is not fully reversible, but, if the material is let alone for a couple of hours or more, it will heal and the stiffness of the virgin material will be at least partially restored. Considering an unconditioned virgin material, an increase of the strain amplitude will lead to a decreasing modulus partly due to Mullins effect and partly due to the previously mentioned Payne effect. It follows that an accurate estimation of the maximum strain reached by the rubber component or test piece must be taken into account to analyze its mechanical behavior.
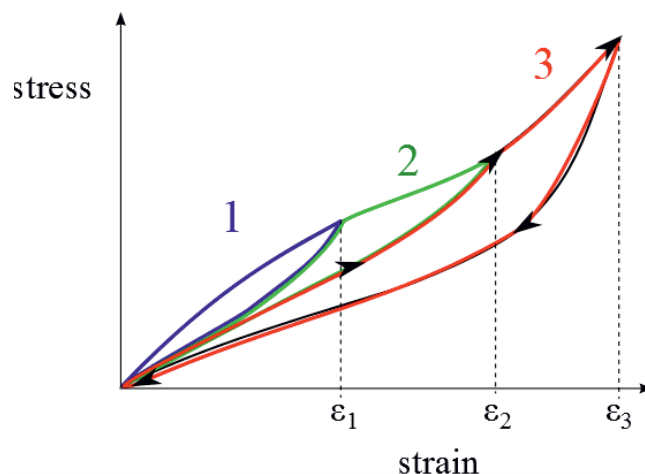

Fig. 1.18:   General stress/strain curves trend for filled rubber showing the Mullins effect.

2.   Rubber friction

The friction coefficient μ between two bodies is defined as the proportionality factor between the frictional force contrasting the motion F_F and the normal load F_N acting on the bodies. Despite quite often μ is expressed as a coefficient, in real application friction is a much more complex phenomena which cannot be described by a linear relation. In case one of the friction partners is made of rubber, indeed, the friction coefficient is not a constant value but it depends rather on both external factors, such as surface roughness and internal factors associated with rubber's viscoelastic properties.

The present work is focused in understanding the contact mechanics with a particular interest in friction between rubber and rigid rough substrates. Generally the following mechanisms are admitted for friction forces generating between rubber and a rigid surface:

- *Adhesion*, friction force generating on molecular length scale between the surfaces which come into a close contact;
- *Hysteresis*, friction caused by the energy loss occurring during the indentation of an asperity. As rubber is viscoelastic, a part of the work done to deform it is not given back, resulting in a resistance to the movement;
- *Abrasion*, mechanical failure induced by high stresses generating in presence of sharp asperities. The energy required to cut out material generates a friction force;
- *Viscous*, friction force caused by the shearing of a viscous medium present in the contact zone.

A schematic illustration of the above mentioned mechanisms is provided in Fig. 2.1. Based on friction conditions (compound, substrate nature and morphology, loads, velocity, temperature) one mechanism can prevail on the others. Adhesion, for instance, is dominant for smooth, dry and clean surfaces, where molecular attractive forces can be established over a large contact area. In case of rough counter surface, the actual area of contact will be reduced and the rubber will be deformed by the asperities. In this case, generally a reduction of the adhesion contribution in favor of hysteresis is observed. If loads are high and the asperities are sharp enough, abrasion and wear phenomena can dominate, especially at low temperatures or very high sliding velocities where rubber exhibits a fragile behavior. Viscous friction takes place when the bodies are separated by a thin fluid film which is then

sheared during the movement. This mechanism becomes important when high viscosity mediums are used and high sliding speeds are realized [62]. However, viscous friction is typically very small compared with the other mechanisms.
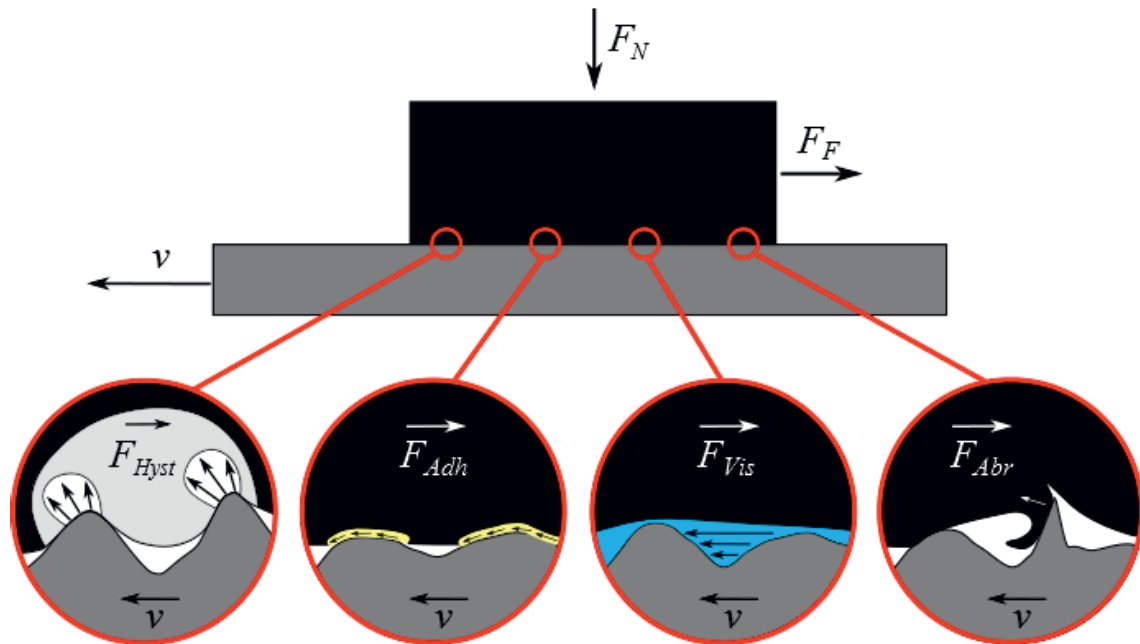
Fig. 2.1:   Main mechanisms of friction between rubber and rough substrates.

In real cases, it can happen that more than one of the above presented mechanisms can occur at the same time. If we think about friction between tire and asphalt, there we have all four phenomena acting. Indeed, it is a common experience that, in addition to hysteresis and adhesion, tire tread are wearing while running and, if water is present on the road, viscous fluid friction could be also present. However, some of these mechanisms have major influence on ordinary tire operating conditions, like braking and cornering.

Kummer already in the 60's estimated that the friction contribution coming from abrasive wear is less than 1% [63]. Based on the tread passenger car tires and the breaking performances at that time, he showed that, to break an average sized car from 80 km/h, more than half tread should be removed to provide enough frictional resistance. Because such wear is not observed, he theorized that other rubber friction mechanisms predominate.

Greenwood and Tabor [64] were the firsts who divided rubber friction into the components of adhesion and hysteresis. They also established that under lubricated circumstances the hysteretic friction part plays much more important role. This means, the presence of a

lubricant usually does not imply a significant viscous friction but can significantly reduce the adhesive interactions between surfaces in contact. The first systematic experimental investigation about rubber friction was carried out by Grosch [65]. He proved in his pioneering studies that the friction force has two main contributions as adhesion and hysteresis, respectively. More specifically, he measured the friction coefficient on both smooth wavy glass and silicon carbide abrasive paper. In order to get rid of adhesion interactions and to obtain a measure of hysteresis, he dusted the substrates with alumina powder as lubricant. A general trend of the overall friction coefficient as a function of the sliding velocity is shown in Fig. 2.2. The friction curve shows two peaks, one at lower velocities coming from the adhesion component, and another one at higher velocities, due to the hysteresis component.
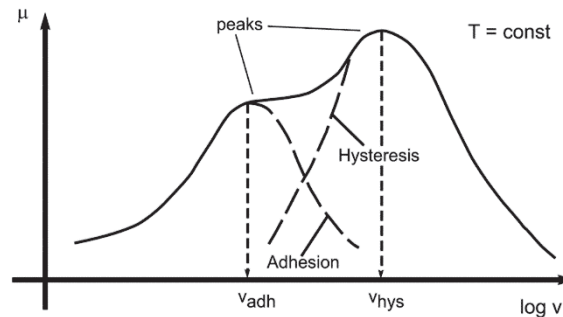
Fig. 2.2:   General trend of the friction coefficient between rubber and a rigid rough surface as a function of the sliding velocity, from [66]. The overall friction corresponds to the sum of hysteresis and adhesion [65].

Grosch also gave the first valuable results on the temperature and velocity dependence of rubber friction, which is closely coupled with the WLF theory. In fact, he proved that, similarly to viscoelastic moduli, also friction can also be extrapolated outside the machine measurement range using mastercurves based on the time-temperature superposition [65].

Comparing the results obtained for a lubricated rough surface with a dry and apparently smooth surface, he observed a shifting of the friction curve to much lower speeds, as schematically illustrated in Fig. 2.3. Therefore he could conclude that such a shifting is induced by the different characteristic distance between the asperities, which in case of a dry smooth surface is much smaller than macroscopic rough surfaces.
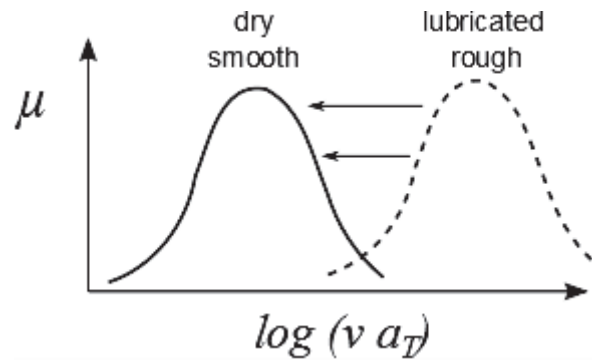
Fig. 2.3:   Comparison between dry friction on smooth surfaces and lubricated friction
on rough surfaces, adapted from [65].

Research studies carried out successively to Grosch's investigation showed that both micro-texture and macro-texture of the countersurface have a strong effect on friction coefficient. In particular, referring to Fig. 2.4, the micro-texture produces a higher grip level, especially at low sliding speed. This effect is even stronger in case of wet friction, where the micro asperities produce significant hysteresis and exert high pressure capable to break through the water film [67] [68] [69]. On the other hand rougher macro-texture implies a better grip level at high sliding velocities.
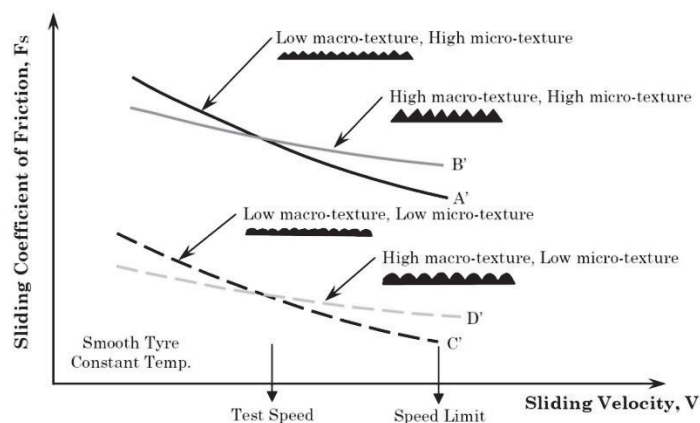
Fig. 2.4:   Effect micro-texture and macro-texture on friction between rubber and rough
substrates at different sliding speeds. Adapted from [70].

In recent times Persson and Klüppel-Heinrich developed sophisticated models capable to describe friction between rubber and rough surfaces in terms of adhesion and hysteresis as two distinct contributions independent from each other [71] [72]. In their models the surfaces are considered to have fractal character and through the power spectra density the contact realized on different length scales is taken into account. They also provide

37

experimental validations of their theoretical models, like shown in Fig. 2.5. The shape of the friction curves is in agreement with the one presented by Grosch, but the lubricant in this case is a mixture of water and soap instead of a solid powder [73] [74].
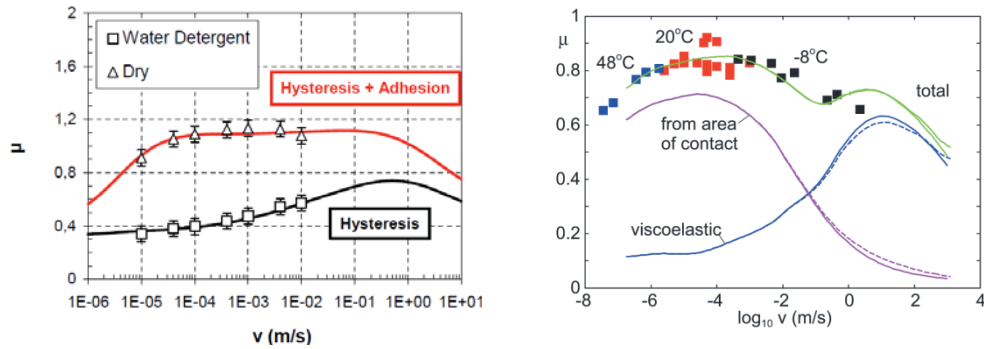
Fig. 2.5: Typical trend of the friction coefficient and his component of adhesion and hysteresis according to Klüppel-Heinrich theory (left) [73] [85] and Persson theory (right) [74].

Based on the presented state of the art, it was decided to investigate the two mechanisms of adhesion and hysteresis, as mainly responsible for friction. A deeper insight into these mechanisms will be given in the following sections.

2.1. Adhesion friction

When the gap between two surfaces is small enough molecular forces appear. In fact, at micro- and nano-scale levels of the surface roughness, the gap size can be comparable with the radius of adhesive forces action. These interactions defined by a specific potential of molecular interaction (Derjaguin et al., 1975 [75]) lead to tangential traction giving the adhesion component of the friction force. The macroscopic adhesion friction force, F_A, can be generally described by the formula:

$$F_A = \tau_S A_c \qquad (18)$$

where τ_s is the interfacial shear strength of the adhesion bonds formed at contact area A_c. Since surfaces are never perfectly smooth the contact area to consider is not the nominal one, A_0, but the real contact area A_c where the intimate contact is actually realized. In fact,

even if rubber is a soft material, only a small part of it is capable to fill in the cavities of the rough surface, like shown in Fig. 2.6. Moreover, the amount of real contact area, for a given contact pair, is dependent not only on normal load, but also on temperature and sliding velocity, because of rubber viscoelasticity.
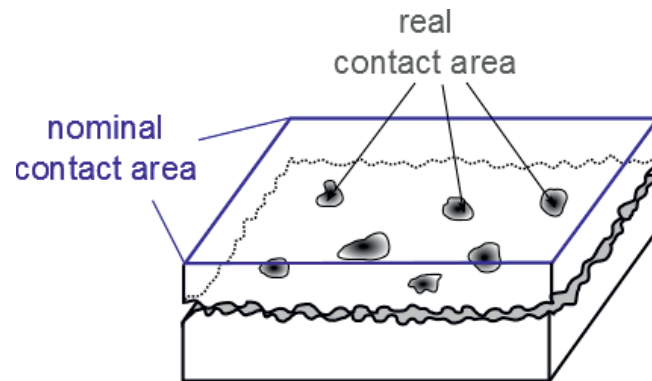
Fig. 2.6:   Nominal and real contact area for rubber in contact with a rough surface. Intimate contact is realized only on a small fraction.

The other crucial parameter interested in adhesive friction is the interfacial shear strength. The physics of this term is not so easy to describe and therefore a comprehensive explanation can be provided starting from the case of a single asperity situation. Similarly to the contact between a cylinder rolling on a flat surface, the contact between an asperity and rubber in relative motion can be regarded as an adhesive junction bounded by two cracks moving in the same direction at the same speed [76]. In particular, one crack is continuously closing in front of the asperity movement, where the surfaces are brought in contact, while at the trailing edge of the contact, where the surfaces are separated, a crack is opening, as illustrate in Fig. 2.7.
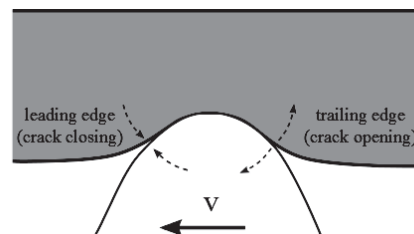
Fig. 2.7:   Adhesion mechanism between an asperity and rubber, based on the crack propagation principle.

Based on this mechanism, energy is gained when the interface is created from two free surfaces and at the same time energy is required to separate contact. However, the energy recovered from reforming the joint is negligible compared with the energy dissipated in breaking the contact and this would explain why an adhesive friction force is generated [77] [78] [79]. The process of the surfaces separation can be described on the basis of peeling off mechanism, where the energy involved to bring apart the surfaces can be estimated in terms of surface energy balance [80]. The effective surface energy, γ_{eff}, in particular must be considered to determine the kinetics of peeling adhesion. For rubber-like materials γ_{eff} may strongly vary with peeling rate and temperature [81]. As illustrated in Fig. 2.8, for small separation rates, v_0, the effective surface energy has a constant value equal to the static surface energy γ_0. By increasing the peeling velocity always more energy is required to break the contact until a critical velocity, v_c, is reached, above which a plateau is observed. The effective surface energy as a function of the peeling rate can be described by a power law, which depends on the material properties. More specifically, the step height is proportional to the ratio between the modulus in the glassy state and rubbery state, E_{∞}/E_0, and the slope, n, can be evaluated from the relaxation time spectra of the polymer [82].
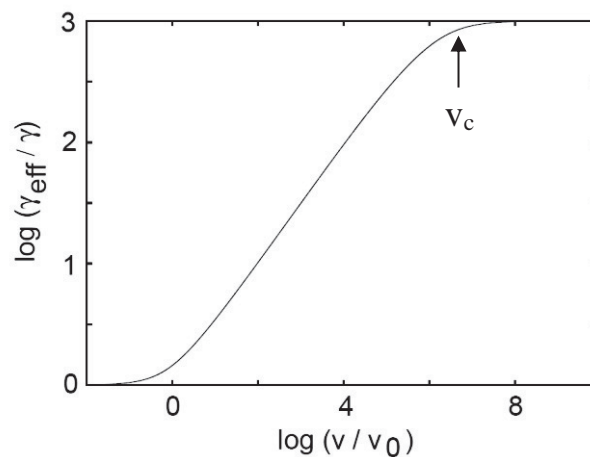
Fig. 2.8:   Dependence of the effective surface energy on the peeling rate or equivalently crack opening velocity from [82]

Based on the concept presented so far, an empirical formulation for the adhesive interfacial shear strength can be derived [83]:

$$\tau_S = \tau_{S,0}\left(1 + \frac{E_\infty / E_0}{(1 + (v_c / v))^n}\right)$$ (19)

Using this formula together with Eq. (18) the adhesive friction component, μ_A, can be expressed as follows:

$$\mu_A = \frac{F_A}{F_N} = \frac{\tau_S}{\sigma_0}\frac{A_c}{A_0} = \tau_{S,0}\left(1 + \frac{E_\infty / E_0}{(1 + (v_c / v))^n}\right)\frac{1}{\sigma_0}\frac{A_c}{A_0}$$ (20)

Where σ_0 is the nominal contact pressure, equal to the ratio between the nominal contact load F_N and the nominal contact area A_0.

41

2.2. Hysteresis friction

Rubber is a soft material and therefore when pressed against a rigid body, it tends to adapt to the interface contour. If sliding is taking place, the rough surface will dynamically excite the layer of rubber which is in contact with it. As rubber is viscoelastic, each local deformation cycle is characterized by a respective hysteresis with a consequential loss of energy. For this reason, the deriving friction force is called hysteresis friction.

In order to better understand this mechanism, a single asperity should be taken in consideration. Consider Fig. 2.9, where the asperity is moving at a particular speed regard to rubber. The part of material located in front of the motion is pushed and slides over the asperity. Since rubber is not perfectly elastic, it does not relax instantaneously once the surface irregularity has been overcome and therefore it can't push on the downstream surface as hard as it pushes on the upstream surface. This unsymmetrical pressure distribution, coming from the hysteretic behavior of rubber, results in friction forces even if surfaces are lubricated and no adhesive interactions are acting.
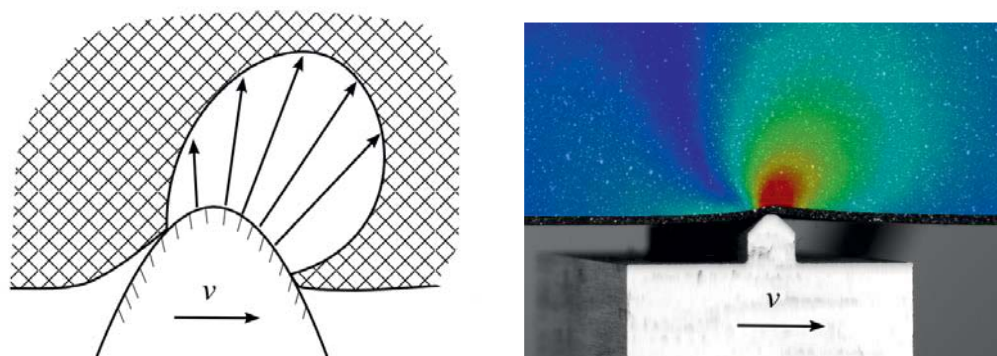
Fig. 2.9:   Concept of unsymmetrical pressure distribution generated by hysteresis friction (left) and deformation analysis performed by optical technique (right).

As previously mentioned, a fundamental study of hysteresis friction was carried out by Grosch in the 60's [65]. A relevant part of his studies focused on measuring the friction on a wavy glass surface. In this special case, during sliding, each surface undulation excites the rubber dynamically at a frequency related to the length of the undulation. The correlation found between the velocity dependence of μ and the frequency dependence of $tan\delta$, [84] confirmed the viscoelastic nature of rubber friction, see Fig. 2.10
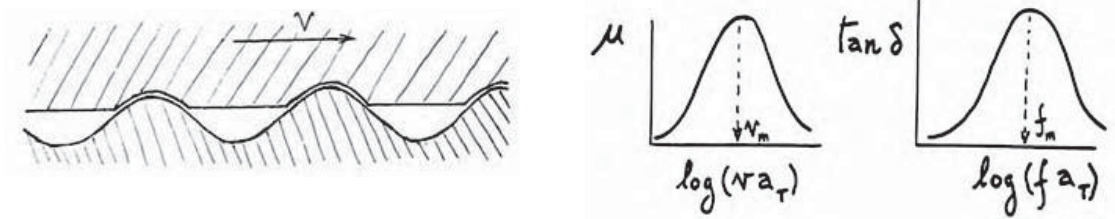
Fig. 2.10: Sliding friction for a viscoelastic material over a sinusoidal surface with a qualitative comparison between friction mastercurve and *tanδ* mastercurve [35]

However, real surfaces have a much more complex structure, and show usually not single asperities irregularities but rather a roughness spectrum. The physical models developed by Klüppel et al. [72] [83] [85] and Persson [71] in recent years demonstrate that hysteresis takes place over all roughness length scales down to the micrometre scale, as long as rubber can fill the cavities. They describe the surfaces with statistical and fractal methods and consider that for each roughness scale corresponds a certain excitation frequency for a given velocity. By integration over the frequency range of the loss modulus it is possible to calculate the hysteresis contribution to friction.

Besides analytical models, finite elements models are becoming always more used. Among these, Wriggers [86] and Kaliske [87] present an innovative approach to calculate hysteresis friction. The method is based on a multi-scale calculation, which consists in reconstructing the surface roughness as a sum of sinusoidal functions by means of the Fourier spectrum. The contact homogenization technique is used to generate the friction law on the smallest scale [88]. This friction law is then incorporated in the finite element formulation on the next larger scale with a specific coupling technique. The resulting friction is again used as input for the next scale. The model proceeds iteratively at the same way until the macroscopic scale has been reached. All the contributions are finally summed up to obtain the overall friction.

Despite the above introduced models provide generally a reasonable description of hysteresis friction, the analytical models are in some cases overestimating the friction coefficient for velocities higher than 10 mm/s and, in any case, they cannot predict the friction curves but just describe it. Concerning the FEM models, it is still not clear how many and which sinusoidal functions one has to choose for an appropriate result. Moreover

43

the coupling method between different roughness scales has not yet been entirely validated by experimental results.

With the present work the fundamentals of hysteresis friction will be investigated, starting from the case of model sinusoidal surfaces up to rough surfaces. Both advanced optical measurement technique and FEM models will be used to provide a deeper knowledge of the phenomena occurring during sliding friction. Each theoretical result will be validated by appropriate experimental measurements.

2.2.1. Hysteresis Friction for model surfaces

Let's consider the general case of a rubber part in contact with a rigid rough substrate. If F_N is the normal load applied, the friction work, W_F, required to realize the sliding at a constant velocity v, can be expressed by the following formula:

$$W_F = \mu F_N v t \tag{21}$$

Where μ is the friction coefficient and t is the sliding time.

As previously mentioned, in case a lubricant is present at the interface and neglecting phenomena of boundary lubrication and fluid shear friction, μ is coincident with the hysteresis component, μ_H. Thus, assuming that the friction work is equal to the energy dissipated in the bulk of the rubber, ΔE_{diss}, Eq. (21) can be rearranged in the following way:

$$\mu_H = \frac{\Delta E_{diss}}{F_N v t} \tag{22}$$

In case of a sinusoidal surface with one main wavelength, the excitation induced in the rubber will be cyclic and the angular frequency is defined by $\omega_0 = v/\lambda_0$, with λ_0 equal to the sinusoidal wavelength. Assuming linear viscoelastic behavior for rubber, the energy loss for each cycle is expressed by the following formula:

$$\Delta E_{diss} = \pi V E''(\omega, \varepsilon)\varepsilon^2 \tag{23}$$

Where V is the deformed volume and E'' is the loss modulus, which is in turn a function of the angular frequency ω and the strain ε. If we consider the sliding process over a multi-

asperity sinusoidal surface, the strain within the rubber sample will be not uniform. The material located near the contact interface is expected to undergo higher excitation compared with the material located in the bulk. Nevertheless, the continuous strain field can be discretized in several regions, each of that characterized by homogeneous strain level, as illustrated in Fig. 2.11. Based on this assumption, from Eqs. (22) and (23) it is possible to write a formula that estimates the hysteresis friction coefficient for a defined sliding velocity:

$$\mu_{H,v} \cong \frac{\pi}{F_N \lambda_0} \sum_i V_{\varepsilon i} E''(\varepsilon_i, \omega_0) \varepsilon_i^2 \tag{24}$$

Where the dissipated energy is calculated as a sum of the contributions coming from the ith volume $V_{\varepsilon i}$ in which the strain ε is assumed to be constant.
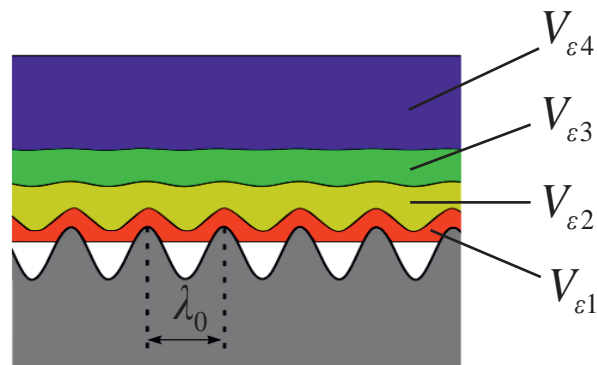
Fig. 2.11: Discretization and homogenization of the strain field occurring in the rubber during the sliding over a sinusoidal substrate

This approach is very important, as one objective of the present work is to verify the correlation between bulk deformation and hysteresis friction and quantify the contributions coming from the different deformed volumes. For this purpose a study of the deformation, occurring in a rubber while sliding over a sinusoidal rigid surface, has been carried out using both optical metrology and finite element model.

3. Introduction to continuum mechanics with respect to Finite Element Analysis

This chapter contains a summary of the continuum mechanics background which is needed for the finite element formulation of solid mechanics and structural problems. In particular, the fundamental balance principles will be briefly discussed, as they need to be considered in all branches of continuum mechanics. Then an overview of the constitutive equations and finite element analysis working principles will be given.

Since the finite element analysis is only a part of the dissertation, a full treatment of the underlying theory will not be formulated. For a more detailed insight the reader can refer to standard books like Altenbach (1994) and Holzapfel (2000) [89] [90].

3.1. Basic balance equations

As first balance we consider is the balance of mass. Each body possesses a mass m which is continuously and homogeneously distributed over an arbitrary region Ω. Assuming that the change of mass has to be zero for every process ($\dot{m} = 0$), both the reference configuration Ω_0 and current configuration Ω must have the same mass:

$$m(\Omega) = m(\Omega_0) \tag{25}$$

Eq. (25) represents the general form of the conservation of mass. If the infinitesimal mass element dm is considered, the rate form of mass continuity in spatial form can be expressed as follows:

$$\dot{\rho}(\mathbf{x},t) + \rho(\mathbf{x},t)div\mathbf{v}(\mathbf{x},t) = 0 \tag{26}$$

Where ρ is the space and time dependent mass density during a motion $\mathbf{x}$, and $\mathbf{v}$ is the velocity field. This principle will be always valid in our calculations, since during the motion no mass will be supplied or absorbed/desorbed within the system.

Another essential principle in continuum mechanics is the balance of linear momentum. The linear momentum is defined in the current configuration as follows:

$$\mathbf{L} = \int_\Omega \rho(\mathbf{x},t)\mathbf{v}(\mathbf{x},t)dV \qquad (27)$$

The balance of momentum states that the rate of change of momentum for a material volume is equal to the sum of external forces acting on the material volume, and it can be mathematically expressed by:

$$\dot{\mathbf{L}} = \int_\Omega \rho\mathbf{b}dV + \int_{\partial\Omega} \mathbf{t}ds \qquad (28)$$

Where $\mathbf{b} = \mathbf{b}(\mathbf{x},t)$ is the body force vector field (e.g. gravitational force) and $\partial\Omega$ is the boundary surface of the region Ω, which is subjected to the Cauchy traction vector $\mathbf{t}$. The stress traction vector can be expressed in terms of stress tensor $\boldsymbol{\sigma}$ through the relation with the surface normal $\mathbf{n}$ (Cauchy's theorem): $\mathbf{t} = \boldsymbol{\sigma}\,\mathbf{n}$. Therefore, using the divergence theorem, which converts the surface integral into a volume integral, the local balance equation of linear momentum is derived from Eq. (28) with reference to the current configuration Ω:

$$div\boldsymbol{\sigma} + \rho\mathbf{b} = \rho\dot{\mathbf{v}} \qquad (29)$$

The stress tensor $\boldsymbol{\sigma}$ is called Cauchy stress tensor and $\rho\dot{\mathbf{v}}$ describes the inertial forces, which can be neglected in case of purely static investigation. In our working framework we also considered the balance of the angular momentum and the symmetry of the Cauchy stress tensor:

$$\boldsymbol{\sigma} = \boldsymbol{\sigma}^T \qquad (30)$$

The body forces can be instead neglected, as self-weight or gravity loading per unit volume have no relevant effects on the analysis.

Besides mechanical balances, the conservation of energy in a thermodynamic process is another important principle necessary to define. The law that postulates such principle is the first law of thermodynamics:

$$\dot{E} = P + Q \qquad (31)$$

This means that the change in time of the total energy E is equal to the sum of mechanical power P of all external loads plus the heat supply Q. After several mathematical transformations the local form of the first law of thermodynamics can be obtained:

47

$$\rho \dot{u} = \boldsymbol{\sigma} \cdot \mathbf{d} + \rho r - div\mathbf{q} \tag{32}$$

Where $\dot{u}$ is the time derivative of the internal energy u. The term $\boldsymbol{\sigma} \cdot \mathbf{d}$ is called specific stress power, while the inner heat source r and the heat flux vector $\mathbf{q}$ derive from the heat component. In our case the terms of Eq. (32) are zero, since neither heat is generated within the body nor external sources of heat are considered. Although in reality some heat development occurs during friction tests, all analysis have been carried out considering isothermal conditions, since the most important factor of the investigation was the pure mechanical behavior.

Still in the thermodynamic context the entropy inequality law must be considered, as it describes the direction of an energy transfer process. In principle the inequality is based on the second law of the thermodynamics, which states that heat flows always from the warmer to the colder region of a body and that mechanical energy can be transformed into heat by friction, but this can never be converted back into mechanical energy. At this point is convenient to introduce the Helmholtz energy ψ:

$$\psi = u - \zeta\Theta \tag{33}$$

Where ζ denotes the entropy of the system and Θ is the absolute temperature. The Clausius-Duhem inequality can be then expressed as follows:

$$\boldsymbol{\sigma} \cdot \mathbf{d} - \rho\dot{u} + \Theta\dot{\eta} - \frac{1}{\Theta}\mathbf{q}grad\Theta \geq 0 \tag{34}$$

The last term in Eq. (34) determines the entropy production by conduction heat. As already mentioned in the present work any thermal effect was neglected on purpose, but the inequality is needed to compute the energy dissipation due to viscoelastic losses and mechanical deformations.

In addition to the presented equations, a relation between stresses and displacements, based on the material properties, needs to be defined to perform finite element analysis. This topic will be discussed in the following section.

3.2. Constitutive material modeling

Unlike in classical elastic materials like metals, due to the nonlinear nature of the stress-strain behavior and the time dependent viscoelasticity, it is still challenging to derive a general-purpose constitutive model for rubber. The rapid development of the computer and Finite Element Methods (FEM) programs offered the opportunity to solve equations capable to describe complex mechanical behavior of several materials, including rubber. Commercial FEM software, like ABAQUS have already included, by default, several material models and some of them can be adapted for rubber-like materials. Rate-dependent materials are often modeled in Finite Element Analysis (FEA) as a combination of hyperelasticity and viscoelasticity (visco-hyperelastic model). The hyperelastic behavior is based on invariant based continuum mechanics, while viscoelasticity is modeled through the Prony series. Each of these material models refers to various authors and scientific publications. An overview will be provided in the following paragraphs.

3.2.1. Stress-strain relationship for hyperelasticity

Most treatments of rubber elasticity begin with the fundamental basics of continuum mechanics for an isotropic, hyperelastic material, which is that the strain energy density, W, must depend on stretch via one or more of the three invariants I_i of the stretch tensor:

$$I_1 = \lambda_1^2 + \lambda_2^2 + \lambda_3^2 \tag{35}$$

$$I_2 = \lambda_1^2 \lambda_2^2 + \lambda_2^2 \lambda_3^2 + \lambda_1^2 \lambda_3^2 \tag{36}$$

$$I_3 = \lambda_1^2 \lambda_2^2 \lambda_3^2 \tag{37}$$

Where λ_1, λ_2, λ_3 are the extension ratios in the three principal axis [30].

In this work, rubber is approximated to be incompressible, thus I_3 is assumed to be constant and equal to 1 and does not contribute to the strain energy. Rivlin [91] proposed a general representation of the strain energy density function using a polynomial expression with two variables [92]. The so called generalized polynomial model is usually written as following:

49

$$W = \sum_{i,j=0}^{\infty} C_{ij}(I_1 - 3)^i (I_2 - 3)^j \tag{38}$$

where C_{ij} are the material parameters. In the simplest case, only the first term of the polynomial is considered, so that the Neo-Hooke model is obtained:

$$W = C_{10}(I_1 - 3) \tag{39}$$

Despite its simplicity, this model has some advantages. First, this model can be derived from statistical thermodynamic considerations of a Gaussian distribution of long-chain molecules [93] [94]. But the most significant advantage is that this model is unconditionally stable for positive C_{10}. This means, a fit of the model to the stress-strain curve in one strain state is often adequate for predicting stress-strain curves in other strain states, at least for small and moderate strains. In terms of engineering stress and strain, the Neo-Hooke model exhibits a softening curve i.e. decreasing stiffness with increasing strain, which is also typically exhibited by rubbers at low and moderate strains. At large strains, however, the rubber stress-strain curve exhibits significant elastic stiffening and the Neo-Hooke model cannot capture this behavior.

Adding the second term of Eq. (38), the equation first derived by Mooney [95] is obtained:

$$W = C_{10}(I_1 - 3) + C_{01}(I_2 - 3) \tag{40}$$

This is the so called Mooney-Rivlin model. Mooney derived Eq. (40) by determining an expression for the strain energy that would provide a constant modulus in shear (a modulus that does not depend on the shear strain). The model has some deficiencies. For example Arruda and Boyce [96] [97] show that the Mooney-Rivlin model can potentially strongly overestimate or underestimate stresses at moderate to large deformations. Therefore one must be careful to adapt the model outside the range of the fitting with experimental data.

So still according to the strain energy function proposed by Rivlin in Eq. (38), an extension of the Neo-Hooke model can be derived, by just considering higher order terms of I_1 and in some cases I_2 to improve its accuracy at large stretches. One model belonging to this category is the Yeoh model [98] [99]:

$$W = C_{10}(I_1 - 3) + C_{20}(I_1 - 3)^2 + C_{30}(I_1 - 3)^3 \tag{41}$$

The Yeoh model is a cubic function in I_1. It is thus a version of the generalized polynomial model, but here the number of coefficients is reduced. Based on the similarities between the formulas, it can be said that the Neo-Hooke model is a special case of the Yeoh model, which in turn is a reduced polynomial model. No physical basis for this model is claimed, but it turns out to work well in capturing data from multiple strain states at moderate to large deformations.

As previously mentioned, the stress-strain formulation for the above presented models can be derived from the strain energy density function. The strain energy density can be interpreted as the area under the stress-strain curve. Thus, from the differential of W with respect to the strain the stress-strain behavior can be determined. Stress-strain curves are commonly studied for convenient and simple tests, mostly: uniaxial, biaxial and pure shear or compression. For these cases, the computation of the invariants can be strongly simplified, since correlations exist between the extension ratios in the three main directions. Therefore, the stress-strain formulations of the two models used in the present work (Neo-Hooke and Yeoh) can be calculated considering that:

- for uniaxial tension: $\lambda_1 = \lambda$ and $\lambda_2 = \lambda_3 = 1/\sqrt{\lambda}$;
- for equi-biaxial tension: $\lambda_1 = \lambda_2 = \lambda$ and $\lambda_3 = 1/\lambda^2$;
- for pure shear: $\lambda_1 = \lambda,\ \lambda_2 = 1$ and $\lambda_3 = 1/\lambda$;

So, for Neo-Hooke, considering Eq. (39) and the above introduced correlations in case of uniaxial tensile tests:

$$\sigma = \frac{\partial W}{\partial \lambda} = 2C_{10}\left(\lambda - \frac{1}{\lambda^2}\right) \tag{42}$$

In case of equi-biaxial tests:

$$\sigma = \frac{\partial W}{\partial \lambda} = 2C_{10}\left(\lambda - \frac{1}{\lambda^5}\right) \tag{43}$$

In case of pure shear tests:

$$\sigma = \frac{\partial W}{\partial \lambda} = 2C_{10}\left(\lambda - \frac{1}{\lambda^3}\right) \tag{44}$$

51

At the same way the equations for Yeoh model can be retrieved using Eq. (41) for the strain energy density. In case of uni-axial tests:

$$\sigma = \frac{\partial W}{\partial \lambda} = 2\left[C_{10} + 2C_{20}\left(\lambda^2 + \frac{2}{\lambda} - 3\right) + 3C_{30}\left(\lambda^2 + \frac{2}{\lambda} - 3\right)^2 \right]\left(\lambda - \frac{1}{\lambda^2}\right) \tag{45}$$

In case of equi-biaxial tests:

$$\sigma = \frac{\partial W}{\partial \lambda} = 2\left[C_{10} + 2C_{20}\left(2\lambda^2 + \frac{1}{\lambda^4} - 3\right) + 3C_{30}\left(2\lambda^2 + \frac{1}{\lambda^4} - 3\right)^2 \right]\left(\lambda - \frac{1}{\lambda^5}\right) \tag{46}$$

In case of pure-shear tests:

$$\sigma = \frac{\partial W}{\partial \lambda} = 2\left[C_{10} + 2C_{20}\left(\lambda^2 + \frac{1}{\lambda^2} - 2\right) + 3C_{30}\left(\lambda^2 + \frac{1}{\lambda^2} - 2\right)^2 \right]\left(\lambda - \frac{1}{\lambda^3}\right) \tag{47}$$

3.2.2. Numerical implementation of viscoelasticity

In order to understand the constitutive equations governing the time-dependent behavior of polymers, implemented in ABAQUS, it is convenient to preliminary recall the viscoelastic theory in case of small strains. The most general constitutive equation that satisfies linear viscoelasticity for stress-relaxation tests is typically written using the Stieltjes convolutions as the Boltzmann equation:

$$\sigma(t) = \int_0^t \Gamma(t - s)\frac{d\gamma}{ds}ds \tag{48}$$

Where $\Gamma(t - s)$ is the relaxation function defined as [100]:

$$\Gamma(t - s) = G_\infty + \sum_{i=1}^N G_i e^{(-t/\tau_i)} \tag{49}$$

Where G_∞ is the long-term modulus and G_i is the modulus of the ith spring, with reference to the generalized Maxwell model, previously discussed in sec. 1.2.1.2. Indeed, one possible approach implemented in ABAQUS is that to describe the rate dependent behavior on the basis of the generalized Maxwell model. In particular, the viscous component of the model can be defined by a Prony series expansion, considering the dimensionless form of the relaxation function of Eq. (49):

$$g_R(t-s) = \frac{\Gamma(t-s)}{G_0} = g_\infty + \sum_{i=1}^{N} g_i^P e^{-(t-s)/\tau_i^P} \tag{50}$$

Where G_0 is the instantaneous modulus, $g_\infty = G_\infty/G_0$; g_i^P and τ_i^P are respectively the dimensionless modulus and the relaxation time of the ith Prony element (therefore the superscript P). Therefore, Eq. (48) becomes [101]:

$$\sigma(t) = \int_0^t \left[g_\infty + \sum_{i=1}^{N} g_i^P e^{-(t-s)/\tau_i^P} \right] \frac{d\sigma_0(\varepsilon)}{ds} ds \tag{51}$$

Where σ_0 is the true stress. The convolution integral can be computed using a numerical algorithm based on finite time increments (Kaliske and Rothert 1997 [100]) and considering that the newest versions of ABAQUS (from v 6.10 on) operate with the nominal stress $\bar{\sigma}_0$, a final formulation for the viscoelastic model can be written as follows [102]:

$$\sigma(t) = \lambda(t) \int_0^t \left[g_\infty + \sum_{i=1}^{N} g_i^P e^{-(t-s)/\tau_i^P} \right] \frac{d\bar{\sigma}_0(\varepsilon)}{ds} ds \tag{52}$$

Notice that the stretch ratio $\lambda(t)$ has been introduced to convert the nominal stress term into the true stress after the integration. True stress and nominal stress are related through [103]:

$$\sigma_0(t) = \bar{\sigma}_0(t)\lambda(t) \tag{53}$$

Eq. (52) expresses the viscoelastic model adopted by ABAQUS and is valid only in case of small deformation. The combination of rate dependent and rate independent behavior can be seen, as the nominal stress $\bar{\sigma}_0$ is obtained from hyperelasticity, that in the current work, it is represented by Eq. (42) or (45) depending if Neo-Hooke or Yeoh model is used.

3.2.3.   Material parameters identification

Rubbery material behavior in ABAQUS is represented by a stored energy function combined with a time-dependent function. Therefore, modeling a rubber compound means mostly finding the proper material parameters for the long term behavior as well as for the more important time dependent behavior. As the effectiveness of the calculations is directly related to the quality of the input material data, these need to be determined with the highest accuracy possible. These data can be generated by measuring the material under different conditions and fitting the resulting mechanical properties with a proper material model. The process of applying a suitable material model and finding the parameters, which can best describe the behavior of a given rubber compound, is the crucial aspect of material modeling.

For the current investigation it was assumed that the method described in sec. 3.2.2., which is valid for linear viscoelastic solids and small deformation, could be adapted also for larger strains without committing large errors. Therefore, the material parameters have been retrieved making a separate fitting of quasi static measurements, for the long term behavior, and dynamic mechanical mastercurves, for the time-dependent behavior. Concerning the quasi static measurements, elastomeric compounds, even under very low testing speed always show hysteretic behavior. For this reason, the middle line between loading and unloading cycle has been calculated so that an average stress-strain behavior of the material could be obtained. Because of the Mullins effect, each time the fifth loading/unloading cycle has been considered so that the material could reach a stable mechanical behavior. The procedure is illustrated in Fig. 3.1.

Then, the material parameter fitting consists in obtaining the optimum set of coefficients, for the selected hyperelastic model, that will lead to the minimum error between experimental and theoretical results for each strain mode (uniaxial, biaxial and pure shear) simultaneously.
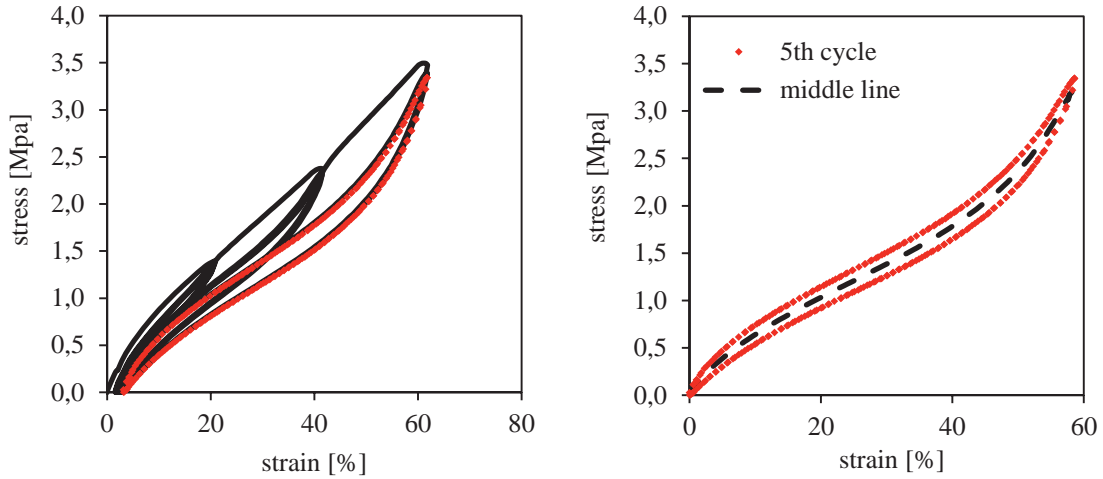
Fig. 3.1: Example of quasi-static behaviour extrapolation for a filled SBR rubber. Left: Mullins effect and the red curve is the 5th loading-unloading cycle identified as reference cycle. Right: middle line calculation of the selected stress-strain cycle (right).

For the time-dependent behavior, the relaxation parameters can be defined including in the program creep or relaxation test data but also through a direct specification of the Prony series parameters. This latter method was used in our case and required the test data to be fitted using an external program. Although the fitting is usually performed with stress-relaxation tests over the time domain, relaxation times ranging between 10^{-4} s and 10^{-7} s are very difficult to be measured using the traditional test methods. For fast dynamic problems, like friction, this could represent a strong limit in obtaining correct simulations results. Therefore, in these cases, it is more convenient to fit dynamic test data, like viscoelastic moduli mastercurves, over the frequency domain up to the GHz region. The Prony series terms can be also calibrated using frequency-dependent test data. In this case ABAQUS uses analytical expressions that relate the Prony series relaxation functions to the storage and loss moduli:

$$G'(\omega) = G_0\left[1 - \sum_{i=1}^{N} g_i^P\right] + G_0 \sum_{i=1}^{N} \frac{g_i^P \tau_i^2 \omega^2}{1 + \tau_i^2 \omega^2} \tag{54}$$

$$G''(\omega) = G_0 \sum_{i=1}^{N} \frac{g_i^P \tau_i \omega}{1 + \tau_i^2 \omega^2} \tag{55}$$

These expressions can be obtained by converting the Prony series terms from the time domain to the frequency by making use of Fourier transforms, as introduced in sec. 1.2.1.1.

So, the measured mastercurve has been used for the fitting of the Prony series parameters, which was performed in Excel using the method of the least squares. More elements per frequency decade have been used to obtain a smooth a more accurate possible fitting.

3.3. Finite Element Analysis: fundamental concepts and terminology

Finite element analysis (FEA) is a valuable computerized tool to solve complex structural analysis problem without the necessity of developing and applying sophisticated equations. Therefore using a software interface the engineer can solve complicated problem just defining carefully the type of analysis and the input parameters. The analysis is based on finite element methods (FEM) which consists in breaking down a real object into a large number of finite elements, usually triangular or rectangular in shape for two dimensional models. Mathematical equations are solved by the FEA software to predict the behavior of each element. A computer then adds up all the individual behaviors to calculate the behavior of the actual object. More in detail, the set of elements constitutes the mesh on which the analysis is performed. Each node of the mesh can move in various directions, specifically translation or rotation, which are known as the degrees of freedom (DOF). By applying boundary conditions, like loads or displacements constraint, to the nodes the range of DOF can be defined, as shown in Fig. 3.2. In mechanical analysis the mesh deformation is calculated thanks to a force displacement equation given by [104]:

$$[K]\{U\} = \{F\} \tag{56}$$

Where [K] is a square matrix or stiffness matrix derived from the models geometry and material properties, {U} and {F} are the vectors of nodal displacements and the vector of applied forces, respectively. When the displacements are applied the (unknown) forces can be calculated and in case forces are applied the above relationship can be inverted to calculate the (unknown) displacements. The FEA software is then capable to solve the equation for each node of the system and reconstruct the body deformation. The more are the elements and the higher will be the accuracy of the solution, even if a too complex model can have unreasonable computational costs. For this reason simplifications can be done using symmetries of the body so that the model can be reduced from three to two

dimensions. In this case plane stress or plane strain analysis can be performed. The first one is used when the model has one dimension negligible if compared with the other two and the loads are in plane with the body, while plane strain is used when the body is long and both geometry and loadings do not vary significantly along the longitudinal direction.
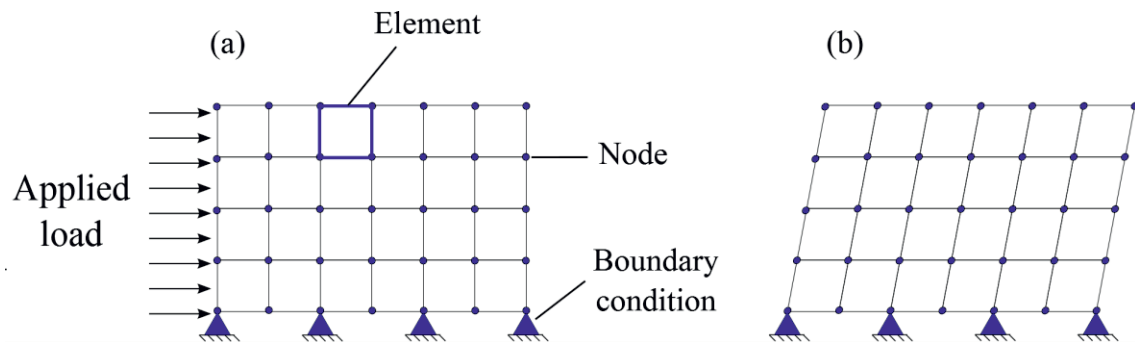

Fig. 3.2: Example of a two dimensional mesh consisting of joined elements (a) and deformed mesh after analysis (b).

A FEA consists usually of three principal steps [105]:

1. *Preprocessing*: the user defines the geometry of the model and the element properties based on the type of analysis (structural, thermal, viscous) and the problem dimension (2D, 3D). In this step the meshing is also performed, normally by overlaying it on a preexisting CAD geometry, and the material properties are assigned. The boundary conditions are finally specified.

2. *Analysis*: The dataset prepared by the preprocessor is used as input to the finite element code itself, which constructs and solves a system of linear or nonlinear algebraic equations. In ABAQUS, the solution is subdivided into small time steps, specified by the user. The state of each incremental step is updated from time t to $t + \Delta t$, so that the state of a following increment at $t + \Delta t$ is determined based on information at t. By this, the equilibrium solution is calculated. However, equilibrium throughout the whole calculation is not guaranteed especially in conditions when an instability is approached. An automatic time step control is introduced, which decreases the time increment whilst it tries to find a minimum energy solution [106].

3. *Postprocessing*: the calculated results can be graphically presented so that the analysis can be easily interpreted. A typical postprocessor display overlays on the

model colored contours representing stress or strain levels. Specific information like forces, displacements, contact area and energy, can be of course quantified for a single node as well as for the whole body.

3.3.1. Contact modeling in FEA

A friction simulation requires that an interaction exists between the two bodies. ABAQUS has many possibilities to simulate contact interactions. The most suitable contact formulation for friction between rubber and a rigid substrate, is the surface-to-surface and finite sliding formulation. The first step is to define the contact pair surfaces, identified as master surface and slave surface. Generally the master surface has to be chosen as the surface of the stiffer body, which in our case would be the substrate, while the slave surface will belong to the rubber part [107]. Then the contact needs to be established between the bodies. As far as it might look an obvious aspect, the contact formulation in the FEA is not an easy task. In fact, in order to avoid interpenetration of surfaces and identify the sliding direction the code has to be capable to distinguish if and where the contact occurs.

Generally contact is split into normal and tangential contact. Normal contact can be formulated as a geometrical constraint, which describes the non-penetration condition of two bodies in contact. This is the so-called Signorini contact description, which models the non-penetrability of the bodies in contact with the following relations. For contact it holds that $g_N = 0$ and $p_N < 0$, where g_N is the gap distance and p_N is the normal pressure. In case a gap is present between the bodies the pressure is equal to zero. This can be formulated as: $g_N \geq 0; \; p_N \leq 0; \; g_N \, p_N = 0$. This formulation states that only compressive forces can be transmitted if there is contact (no adhesion) and forms the basis of contact problems.

For ABAQUS simulations a hard kinematic contact was used. This means, in each increment of the analysis, ABAQUS first advances the kinematic state of the model into a predicted configuration without considering any contact condition and then determines which slave nodes, in the predicted configuration, penetrate the master surface. The depth of the node penetration and the time increment are used to calculate the force required to oppose the penetration. The slave surface, namely the rubber surface, will then be deformed so that its nodes will lie exactly on the master surface. The iteration of the calculation is schematically shown in Fig. 3.3. However, in case of hard kinematic contact it is still

58

possible for the master surface to penetrate the slave surface, but using a sufficiently refined mesh on the slave surface will minimize such penetrations.

In addition to normal contact, tangential contact needs to be defined in the FEA code, too. ABAQUS calculates the tangential behavior in a contact interaction using the local tangent directions as reference orientation. The response in the tangential direction can be modelled in several ways. Mainly a distinction is made between interaction with or without friction. Friction means that the nodes of master and slave surfaces are hold together as long as a certain magnitude of shear stress is reached. Above this critical shear stress, sliding of surfaces starts as a function of the contact pressure between the surfaces. In case of the simple Coulomb model, a linear function exists between normal pressure and tangential stress, and the proportionality factor is the friction coefficient. Several others approaches are available in ABAQUS which can describe more complex situations and even a temperature, velocity or pressure dependence of the friction coefficient can be implemented. Nevertheless, in the present study the frictionless interaction resulted to be the most interesting. The aim was indeed to calculate the friction forces generated by viscoelastic losses due to hysteresis deformation occurring while sliding. For this purpose introducing a local tangential friction as input in the model would be not meaningful.
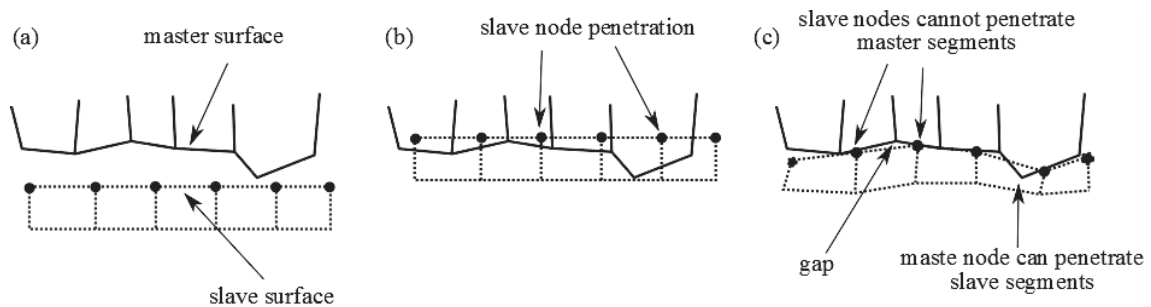

Fig. 3.3: Step iteration for kinematic contact in ABAQUS. In the first step the surfaces are not yet in contact (a); then the configuration without contact is predicted and in the final step the contact solution is achieved (c).

4. Materials and methods

In this chapter the materials and the experimental equipment and techniques adopted to carry out the investigation will be presented. In the first part the rubber compounds will be described, while in the second part an insight of the single machines mechanisms and physical principles will be provided.

4.1. Model rubber compounds

Four rubber compounds have been used for the investigation and can be grouped in two categories. One group characterized by simpler composition, namely, a single polymer and lower filler content, and a second group, characterized by a blend of polymers and higher filler content.

Table 1: Chemical composition and glass transition temperature of the rubber used for the investigation. T_g evaluated by DSC.

Name	styrene (%)	vinyl(%)	Tg (°C)
Buna VSL VP PBR 4041	25.6	46.7	-23
Buna VSL 2525-0	25	25	-49

Table 2: Formulation of the first compound group.

Ingredient (phr)	compound name	
	A	*B*
S-SBR VSL VP PBR 4041	100	-
S-SBR VSL 2525-0	-	100
Silanized silica - Coupsil 8113	25	25
Carbon black - N375	5	5
Stearic acid	1	1
Zn Oxide	3	3
Sulfur	2	2
TBBS	2	2
DPG	2	2

For the first group of compounds, two different styrene-butadiene rubbers, characterized by different glass transition temperatures (Table 1) were chosen and mixed with 25 phr of silanized Silica (Coupsil 8113®) and 5 phr carbon black (N375), see Table 2. Lower

amount of filler was adopted in order to have model material characterized by reduced non-linearity and at the same time withstand multiple friction tests without excessive abrasion. Five phr carbon black were added to the compound just to obtain black color useful to get a better contrast for the optical investigation.

The general composition of the second compound group is presented in Table 3. Even if the exact formulation is not reported because of confidential agreements, the idea was to have blend systems featuring more filler content in order to enhance non linearity. The names *S* and *H* have been used to recall the soft or hard mechanical behavior exhibited by the materials.

Table 3:   Formulation of the second compound group.

Ingredient (phr)	compound name	
	S	*H*
SBR	80	-
BR	20	75
NR	-	25
CB	30	55
Silica	70	-
Silane	7	-
Oil	40	-
Stearic acid	2	2
Zn Oxide	2	2
Sulfur	4	6
Accelerator	4	4

4.2. Dynamic mechanical analysis

In dynamic tests the rubber sample is subjected to a cyclic deformation pattern from which the stress strain behavior is calculated. As already discussed in the introduction, thanks this kind of tests it is fundamental to evaluate the viscoelastic moduli of rubbery materials. The method used in the present work is force vibration in which the oscillation is maintained by an external means.

The compounds used for the present study have been characterized using a Rheometric Scientific ARES mechanical spectrometer. The storage and loss moduli as a function of frequency, temperature and amplitude have been evaluated performing dynamical torsion excitation on 2 mm rubber strip samples. A picture showing the clamping of the sample is reported in Fig. 4.1. In particular the upper clamp is rigidly connected to the force transducer while the lower one applies the dynamic excitation to the specimen through a rotation. The sample is longitudinally pretensioned during the test with 1 N force so that no buckling or instabilities can occur. The system can be enclosed in a temperature chamber, in order to have the environmental control.

Fig. 4.1:   Detail of the sample during a torsion dynamical test performed by the ARES.

For torsion the deformation is essentially in shear and for a strip much wider than its thickness the shear modulus G can be calculated considering that the torque M is:

$$M = \frac{k_1 b t^3 G \beta}{L} \tag{57}$$

Where k_1 is a function of the width and thickness of the strip, b is the strip width, t the strip thickness, β the twist angle and L the strip length.

Dynamic properties are strongly dependent on temperature and frequency so preferably results should be obtained over the widest possible range of frequencies and temperatures. Since the operating excitation frequency range of the machine is limited between 0.001 and 80 Hz, the time temperature superposition can be adopted to extend the material properties over higher larger or smaller decades. For the friction properties the high frequency range (> 1000Hz) is very important and therefore, in order to estimate the storage and loss modulus frequency/temperature sweeps have been performed. The temperature range was +60°C to -15°C, with 5°C step and the excitation frequency spanned from 0.01 to 10 Hz. The strain amplitude is constant for the whole test. Then the mastercurve could be constructed shifting the isothermal measurements along the frequency axis.

Strain sweep tests up to 10%, using 1 Hz as excitation frequency, at room temperature have been also performed to measure the dependence of the loss modulus on the strain amplitude.

For the validation of the material model frequency sweep tests have been performed in compression suing another dynamic mechanical machine which works following the same principle of the ARES: the Explexor Gabo 500N. This machine, contrary to the ARES, is characterized by an electromagnetic shaker which can apply longitudinal dynamic excitations. This allows besides shear tests also tension and compression tests. Hence, it was possible to perform frequency sweep tests on prism shaped rubber specimen in compression under force control and extrapolate the hysteresis stress-strain loops.

4.3.   Quasi-static stress-strain measurement

The quasi-static tests are used to determine the relationship between an applied force and the resulting deformation. Generally the measured quantities are expressed as stress, (force per unit of cross sectional area) and strain (deformation referred to the initial dimension). The term "quasi-static" is applied to distinguish this group of tests from the dynamic or cyclic tests. The meaning has to be understood referring to tests in which the deformation time is much greater than the time required for the molecular network to respond to an applied stress. Therefore these tests allow the estimation of the material stiffness with almost no viscoelastic features in it. Such peculiarity is very important when a proper material model needs to be determined, like for the case of Finite Element methods.

The tests were carried out at room temperature under uni-axial, equi-bi-axial and pure shear mode using a Zwick universal testing machine with a crossbar speed of 5 mm/min. The uniaxial test has been performed using the well-known dumbbell specimen stretched along its axial direction. The tensile samples have been cut from the vulcanized 2 mm thickness sheet, according to the geometry indicated in the ISO 37 norm [108].

Fig. 4.2:   Pure shear test seen from the front. Sample stretched at 30%.

A good approximation to pure shear test condition is obtained with a strip test piece stretched perpendicular to its length as shown in Fig. 4.2. The strip thickness must be small compared with its width and the width small compared to its length of a factor 10 as suggested by the norm BS 903-5. Therefore a vulcanized strip of 200 mm x 20 mm x 2 mm was used for the investigation.

Biaxial tests are often preferred to produce data for input to finite element programs. Although currently there is no ISO standard for such a test the British standard BS903-5 for finite element analysis on rubber outlines an approach based on the equi-biaxial stretching of a flat sheet. The biaxial straining rig has two members to which the specimen is attached by gripping links. The two members slide past each other when a force is applied by the crossbars, hence stretching the specimen in two directions, like illustrated in Fig. 4.3. The roller bearings installed on the grippers ensure that the pull force remains normal to the edges during the test.

In all cases, in order to avoid the distortion of the clamped zone, the deformation is evaluated considering the optical extensometer which follows the marks on the sample with a light beam.

Fig. 4.3:   Equi-biaxial test performed in the Zwick machine.

4.4. Friction measurements

The friction measurements have been carried out using the tribometer self-developed by the DIK in collaboration with the IMKT department of the University of Hannover. The testing principle of the machine is quite simple. The sample is placed in contact with the substrate and a force transducer records the friction forces generating when the the relative motion between the two friction partners is created. As illustrated in Fig. 4.4, the substrate is linearly driven by a motor at a desired speed (from 5 μm/s to 300 mm/s) for a distance up to a maximum of 300 mm. The sample is directly connected to the force transducer and is pressed against the substrate thanks to weights applied on the rotating shaft installed to the static part of the machine. The shaft can freely rotate so that the sample can follow the surfaces irregularities. The normal load is applied with a dead weight system up to a maximum of 500 N.
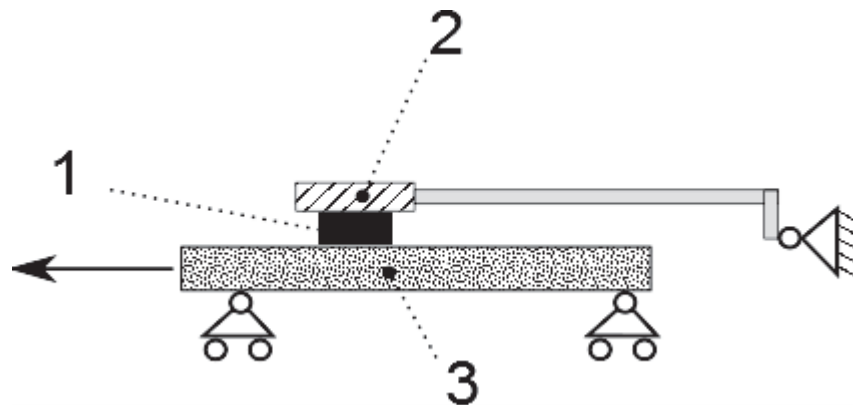

Fig. 4.4:   Scheme of the friction machine. 1: sample; 2: force transducer; 3: substrate.

A typical friction measurement is qualitatively described in Fig. 4.5. During the first part of the test the sample is sticking on the surfaces and the friction forces raise until the shear stresses are high enough to reach the sliding regime. During sliding a scatter of the force is generally observed due to vibrations and surface irregularities. When the motion terminates the sample relaxes slowly back to the initial condition. The friction coefficient can be calculated dividing, by the normal load, the average friction force measured during the pure sliding regime. The temperature can be also controlled thanks to a climate chamber, within which the whole friction machine, except the engine of the driving motor, is installed.
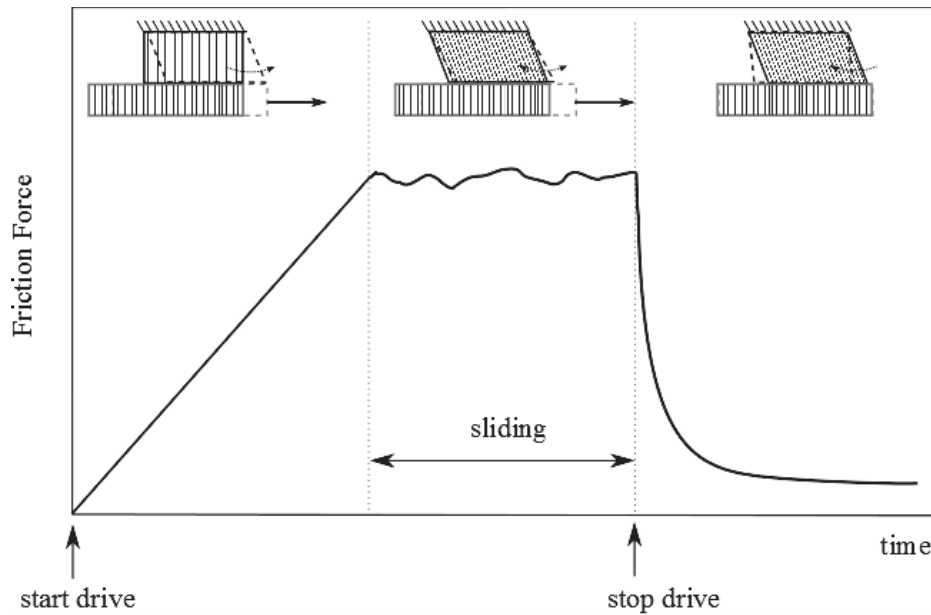
Fig. 4.5: Qualitative trend of a friction measurement. The friction coefficient is calculated from the average values of the friction forces in the sliding regime.

4.4.1. Substrates

In order to understand the fundamental mechanisms of rubber friction model sinusoidal multi-indenters have been used in the first part of the investigation. In particular, two different multi-asperity indenters made of aluminum have been used. They were built to have a different distance between the asperities. The bigger one with a size in the millimeter scale, while the smaller one rescaled of a factor three. A detailed sketch of the indenter's geometry is shown in Fig. 4.6.
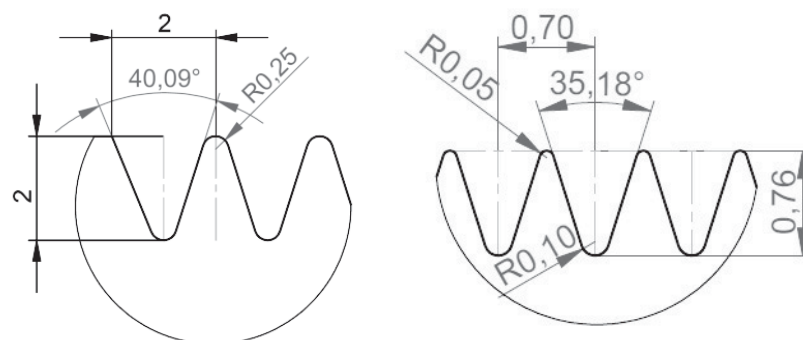

Fig. 4.6: Technical draw of the multi-indenters geometry used for the friction tests

Additionally to the model substrates also the effects of rough substrates on friction were considered. For this reason two pavers presenting homogenous and regular roughness but a different surface morphology have been selected from a local stone supplier.

4.5.   White light interferometer – roughness

For the characterization of the surface roughness an optical device based on white light interferometry has been used. The MicroProf® is equipped with a particular sensor FRT CWL based on a patented method which makes use of the chromatic aberration (in principle the wavelength dependent refractive index) of optical lenses. This measuring method can be described as follows: The sample is illuminated by focused white light while a xy table is moving so that profile or surfaces can be analyzed. By meeting a surface, the focused light – in contrast to the unfocused components of the beam - will be optimally reflected (Fig. 4.7).It gets into a miniaturized spectrometer via the same lens through a glass fiber cable. A passive lens with larger chromatic aberration fans out the white light vertically in different colored focal points. The wavelength (color) of the reflected light is matched with a calibration table and gives the resulting distance between the sensor and the sample.
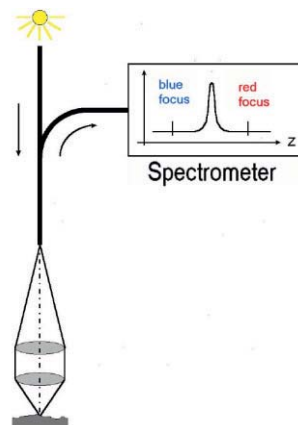

Fig. 4.7:   Measurement principle of the optical sensor (from MicroProf manual)

The lateral resolution is about 250 nm, while the size of the light spot projected on the sample is 1μm. The local z-resolution of the sensor is 50 nm and the maximum vertical range for a single layer measurement is approximately 300 μm. For sample structure higher than 300 μm, the MicroProf® allows the measurement via the so-called "layer by layer"

(vertical stitching) mode. For that purpose, the sensor is automatically moved upwards with the z-axis between each measurement of a 300 µm layer. The measured data of the layer will be stitched together in the computer, leading to an overall picture ("extended topography"), like shown in Fig. 4.8.
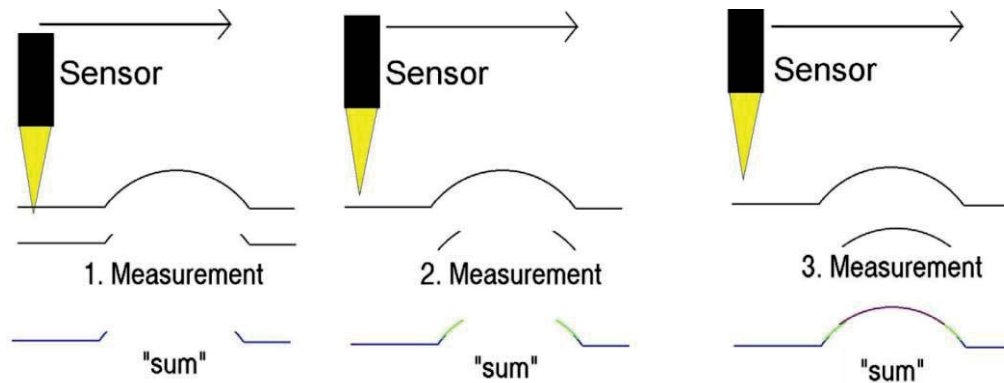

Fig. 4.8:   Principle of the layer by layer measuring method to allow measurements of complex sample's structures with a roughness higher than 300 µm.

4.6.   Optical measuring technique

This measuring technique consists in processing the digital images of the sample deformation, acquired by a camera, to calculate strain and local displacements of the material.

The analysis presented in this work has been performed using the ARAMIS system from GOM. This is a non-contact optical 3D deformation measuring system which analyses and calculates deformation. In particular, the software recognizes the surface structure of the measuring object in digital camera images and allocates coordinates to the image pixels. Once the undeformed image is defined, the ARAMIS compares the digital images recorded during the measurement and calculates the displacement and the consequential deformation of the object characteristics. A graphical representation of the results can be also obtained to provide an optimum understanding of the behavior of the measured object. The object characteristics are identified by the ARAMIS by means of a proper surface preparation of the sample, which usually consists in applying a good contrasting white and black spray pattern.

The fundamental principle of ARAMIS for 2D analysis is based on the fact that the distribution of grey scale values of a rectangular area (facet) corresponds in the same area of the undeformed and the deformed state. In Fig. 4.9 a starting point is defined in the reference image (left image), which must also be defined as a starting point for the deformed state (right image). The following relation exists between the grey values at these two points:

$$g_1(x, y) = g_2(x_t, y_t) \tag{58}$$

The pixels of the facet in the reference image are then transformed into the deformed image as follows:

$$x_t = a_1 + a_2 x + a_3 y + a_4 xy$$
$$\tag{59}$$
$$y_t = a_5 + a_6 x + a_7 y + a_8 xy$$

The values a_1 and a_5 describe the translation of the facet's center; the others describe the rotation and deformation of the facets.
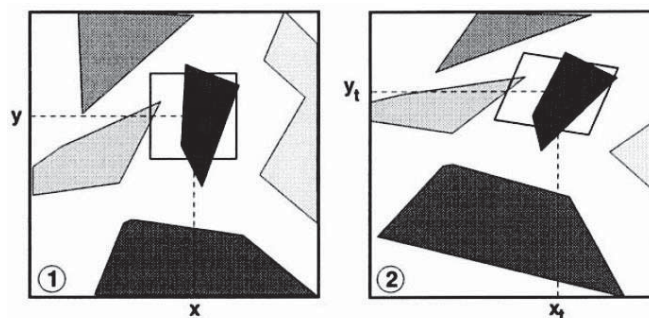

Fig. 4.9:   Facets in the undeformed (1) and deformed (2) state, from [109].

For the current investigation this system has been adopted to calculate the deformation of the sample during friction tests. In particular the images have been recorded using a high speed camera Y4 model from MotionPro and ARAMIS version 6.1.

4.7. IR-thermography

A thermographic camera is a device capable to create images from the thermal radiation of the bodies. The operating principle is that each body, with a temperature above the absolute zero (-273.15°C = 0 Kelvin), emits an electromagnetic radiation from its surface, which is proportional to its intrinsic temperature. A part of this so-called intrinsic radiation is infrared radiation, which can be used to measure a body's temperature. This radiation penetrates the atmosphere and with the help of a lens (input optics) can be focused on a detector element, which generates an electrical signal proportional to the radiation. The signal is amplified and, using successive digital signal processing, is transformed into an output signal which correlates with the object temperature. A typical visualization result is shown in Fig. 4.10.

This technique has been used to investigate the temperature increase induced in the sample due to frictional heating. The measurements have been carried out using the VarioTHERM camera from InfraTec ® and for the image analysis the software IRBIS plus v2.2 was used. The camera was positioned at approximately 50 cm from the sample in order to have the best focus on it during the sliding.
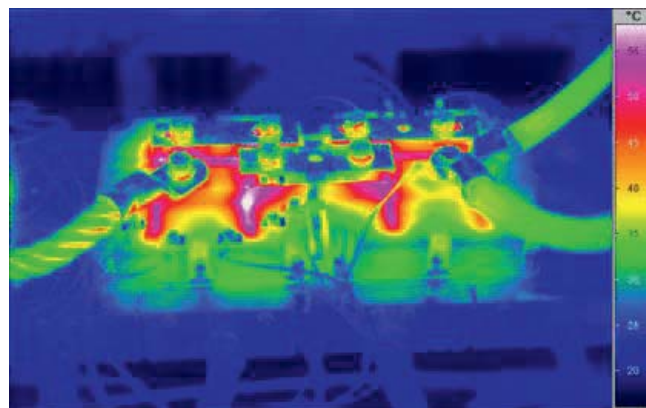

Fig. 4.10: Example of IR-thermography. Test on a power semic-conductor (from InfraTec ® website)

5. Results and discussion

5.1. Mechanical analysis

The compounds, selected for the investigation, have been tested under both quasi-static and dynamic conditions. The first type of measurement gives information about the long term behavior of the material, which are then useful, especially for the case of FEA material modelling (sec. 3.2). The dynamic mechanical tests provide information about the viscoelastic behavior which is of crucial importance for friction.

5.1.1. Quasi-static measurements

The quasi-static measurements have been carried out for the 4 model compounds and the uni-axial test result is shown in Fig. 5.1. From the stress-strain behavior it is possible to see a clear distinction between the materials. Samples A and B show almost pure elastic linear behavior and small hysteresis because of their low filler content, while the other 2 model compounds, H and S, show both higher hysteresis because of the higher filler content. The compound S, despite its highest amount of filler (30 phr CB + 70 phr Si), has the lowest stiffness due of the presence of the softener (40 phr) in the mixture. The reinforcement effect is remarkable if we consider the sample H, which has an amount of filler (55 phr CB) that allows to reach the percolation threshold, with consequential increase of stiffness.
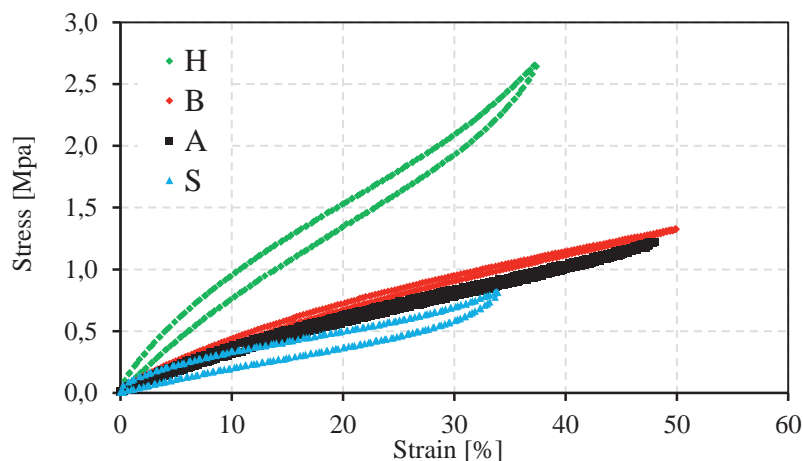

Fig. 5.1:   Stress-strain curves obtained with uni-axial quasi static test. Crossbar speed 5 mm/min and room temperature

To facilitate the reader to follow the results, it was decided to name H (Hard) the material with the highest stiffness and S (Soft) the compound with the lowest one, so that a connection between material properties and sample name can be easily kept in mind.

5.1.2. Dynamic mechanical analysis

As already mentioned in the previous sections, the properties of rubbery material are strongly dependent on frequency and temperature of excitation. We also saw that to extrapolate the dynamic behavior over several decades, one of the most commonly used method is the mastercurve construction through the WLF Eq. (17), which is the approach applied also in the present work. More specifically, the isothermal measured curves of *tanδ* have been shifted along the frequency axis, so that they could match each other. In order to get a proper mastercurve, shifting factors a_T have been applied to the small strain amplitude measurements (0.1 %), as the material exhibits a linear behavior, and then adjusted until they could fit a WLF based equation. From the fitting it was possible to obtain coefficients C_1 and C_2, see Fig. 5.2, which were then used to shift *G'* and *G''* curves for larger strain amplitude measurements (2.5 %). In case of the high filled systems, a vertical shifting was then required to compensate the gap between high temperature branches, caused by the presence of a filler network [110]. The coefficients C_1 and C_2 calculated for the investigated compounds are listed in Table 4 and an example of measurement and mastercurve construction is shown in Fig. 5.3.
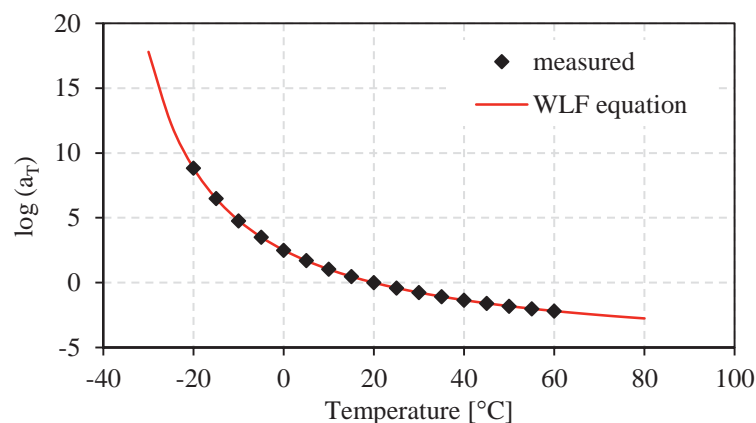

Fig. 5.2:   Fitting between the shifting factors applied to the compound A measured at 0.1 % strain, from +60°C to -20°C.

Table 4:   Coefficient used for WLF transformation in K^{-1} considering a reference temperature of 20°C.

sample	C1	C2
A	5.8	66.3
B	5.0	99.0
H	4.8	123.6
S	12.0	169.0

The calculated mastercurves of *G'* and *tanδ* for the model compounds used in the present work, are plotted in Fig. 5.4 and Fig. 5.5, respectively. The different trend of dynamic mechanical properties between the 4 compounds results from their different formulations. Compounds A and B, which are both SBR based compounds with lower amount of filler, show, indeed, a similar behavior [111].
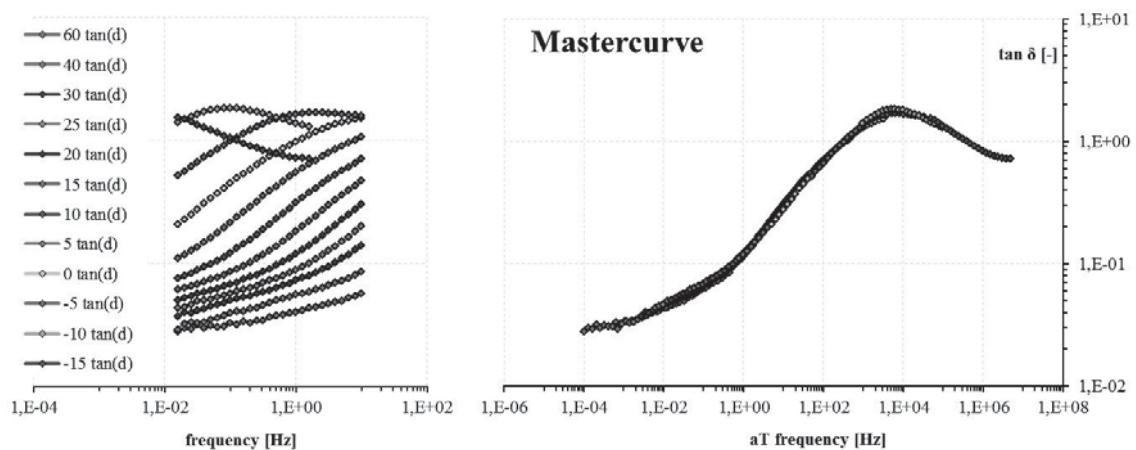

Fig. 5.3:   Mastercurve construction of tanδ for the sample A using the WLF coefficients $C_1 = 5.8$ and $C_2 = 66.3$, at 20°C reference temperature. Measurement conditions: 0.01 to 10 Hz; +60°C to -15°C; 2.5% strain.

The lower T_g of compound B implies mainly just a shifting of the glass transition to higher frequency compared with compound A. The other two compounds show their glass transition to even higher frequency ($10^6 - 10^7$ Hz) because of the presence of polymers with lower T_g like BR, for S; while for the compound H, NR was used in place of SBR. However, differences can be observed between the two blend systems, especially on *tanδ* mastercurve (Fig. 5.4). SBR/BR blends, like compound S, show, in addition to a shifting of the T_g also a broadening of the glass transition [112]. This effect derives from the miscibility of the two polymers due to their chemical affinity [113]. Compound H which consists of NR/BR

74

blend shows a double peak because of the polymer immiscibility [114] [115] [116] (in the investigated range just the beginning of the second transition can be seen around 10^{10} Hz).

Analyzing G' mastercurves is furthermore possible to see the reinforcement effect of the filler, which produces higher stiffness for compounds S and H in the rubbery regime. By extrapolating the curves for very long time, that means very small frequency ($< 10^{-5}$), a correlation with the quasi static measurements could be observed, thus confirming the reliability of the master curve construction.
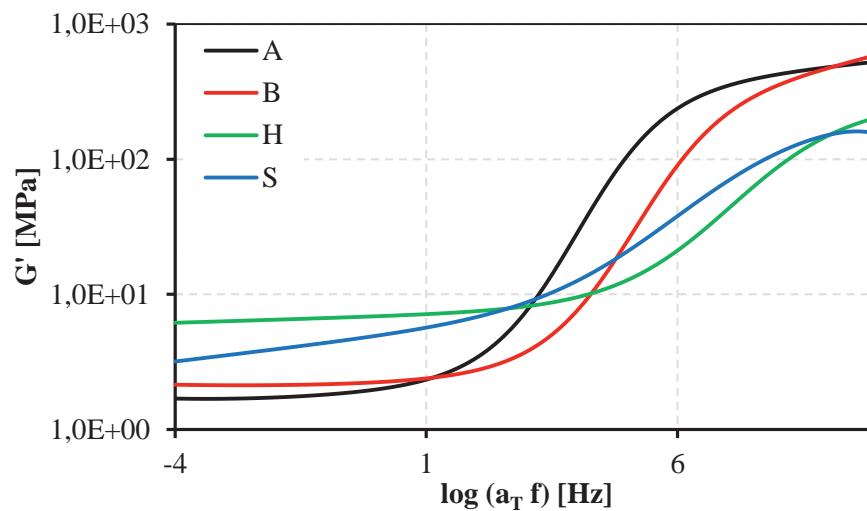

Fig. 5.4: Storage modulus mastercurves of the model compounds for 20°C reference temperature, 2.5 % strain.
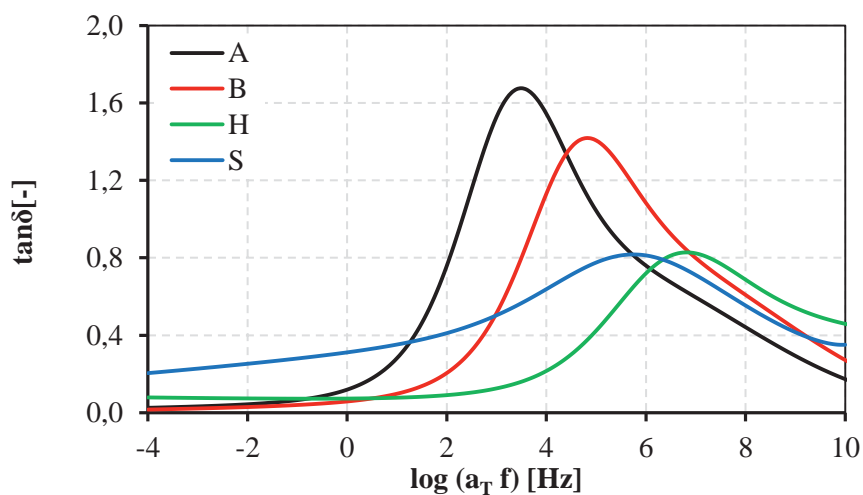

Fig. 5.5: Loss factor mastercurves of the model compounds for 20°C reference temperature, 2.5 % strain.

Another important feature of rubber compounds is the dependence of the moduli on the strain amplitude. Typically the dynamic mechanical moduli exhibit a linear behavior only for small amplitude (< 0.1 %). For larger strains, the so called Payne effect, described in the sec. 1.2.3, takes place. In Fig. 5.6 the strain sweep test performed for the sample S is depicted as a typical example of moduli variation as a function of the strain. In order to quantify the sample non-linearity, the difference, Δ, between the small strain plateau value and the highest strain value, was calculated for both G' and G'' and plotted in Fig. 5.7. The clear difference between the materials results from the different amount and type of filler present in them. In particular, for higher filled systems, like H and S, a larger variation of the moduli is observed, while sample A, on the other hand, shows almost a linear behavior, due to the low filler concentration. For sample B a behavior very similar to compound A is expected, because of their almost identical composition.
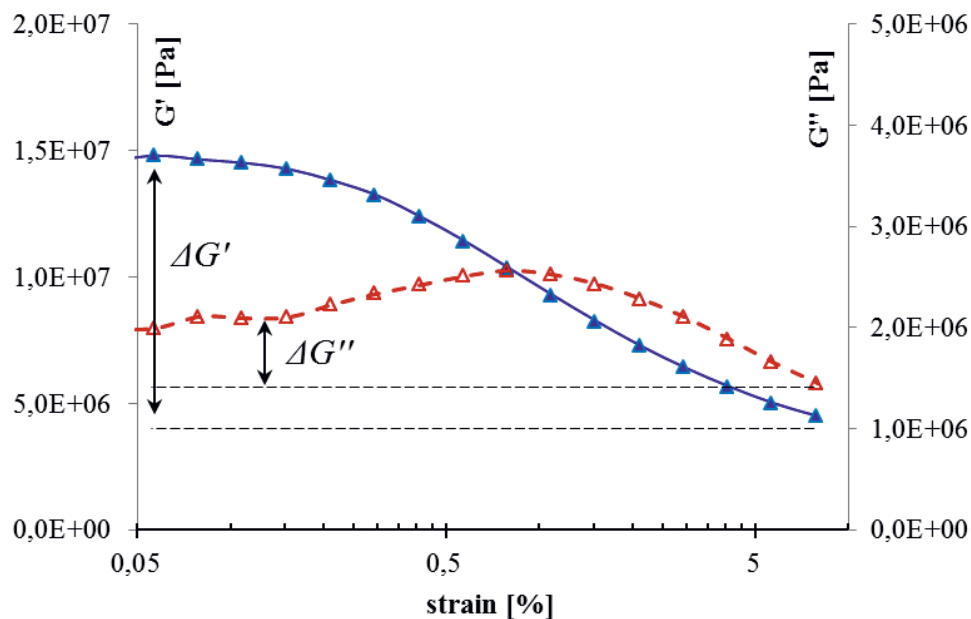

Fig. 5.6:   G' (blu line) and G'' (red dashed line) as a function of strain amplitude for compound S. Measurement carried out at room temperature and 1 Hz excitation frequency.
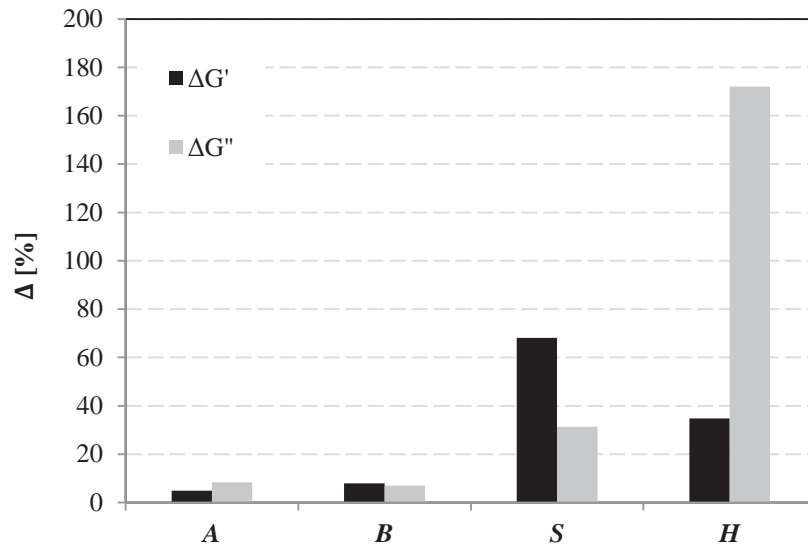
Fig. 5.7: Moduli variation from small strain to high strain expressed in percentage for the investigated compounds, with reference to Fig. 5.6

5.2.   Friction measurements on model surfaces

To understand the basic mechanism and validate the theory concerning the phenomenology of hysteresis rubber friction, it was decided, in the first stage of study, to investigate the friction interaction of rubber compounds sliding over sinusoidal like multi-indenter. In particular, results deal with the effects of the sliding velocity, compound formulation and substrate configuration on the hysteresis part of friction coefficient, μ_H. It is worth to point out that, in order to minimize the adhesive interaction, all measurements have been carried out applying a liquid soap at the interface [117] [118] [119] [120]

The friction coefficient has been measured for different velocities using the 2 mm multi-indenter at 20 °C and 3.5 bar normal pressure. The values, connected with a spline for visualization reasons, are shown in Fig. 5.8. The first evident result is that it is not possible to speak about an absolute friction coefficient, since the friction coefficient is not constant with the sliding velocity. For this reason, to have a comparison between the compounds, the trend of their friction curves should be analyzed. The chart shows that compounds S and H have a lower variation of their friction coefficients compared with the compounds A and B and that H has the lowest friction, over the whole investigated velocity range. Such a different friction behavior among the 4 compounds can be explained on the basis of the correlation between hysteresis friction and the viscoelastic properties of materials. More precisely, considering the measurement velocity range (0.1 to 300 mm/s) and assuming that, for this special substrate, only the macroscopic wavelength is acting, the main excitation frequency, induced by the indenters into the rubber, can be estimated as the ratio between the velocity and the asperity distance. Therefore, if the mastercurves of Fig. 5.5 are taken into account within the resulting frequency range (0.05 to 150 Hz), a correlation can be observed between tanδ and μ (compare Fig. 5.8 and Fig. 5.9). Such result is in line with the publications from Grosch and Schapery, [65] which show the connection between loss factor and friction in case of sinusoidal surfaces and provide a calculation of the characteristic contact length [84]. In particular, compounds S and H, which show in Fig. 5.9 an almost flat trend of tanδ and parallel to each other, with H characterized from a lower values over the analyzed frequency range, show also a similar trend concerning the friction coefficient of Fig. 5.8. Always referring to Fig. 5.9, compounds A and B show an increase of tanδ of about 1 decade with increasing frequency and they both show, as well, a strong increase of their friction as the sliding velocity raises.
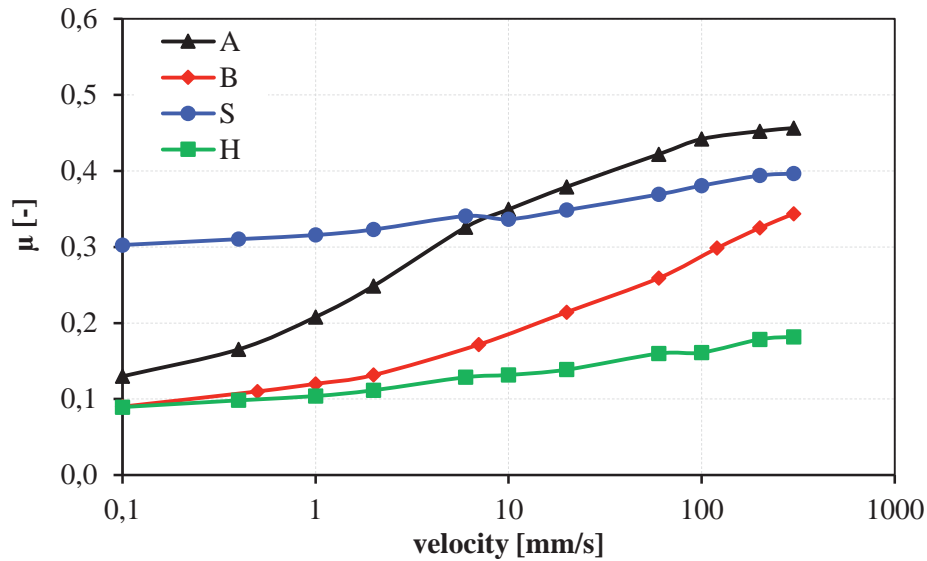
Fig. 5.8: Hysteresis friction coefficient of model compounds sliding over the 2 mm multi-indenter. Values measured at 20°C and 3.5 bar nominal contact pressure.
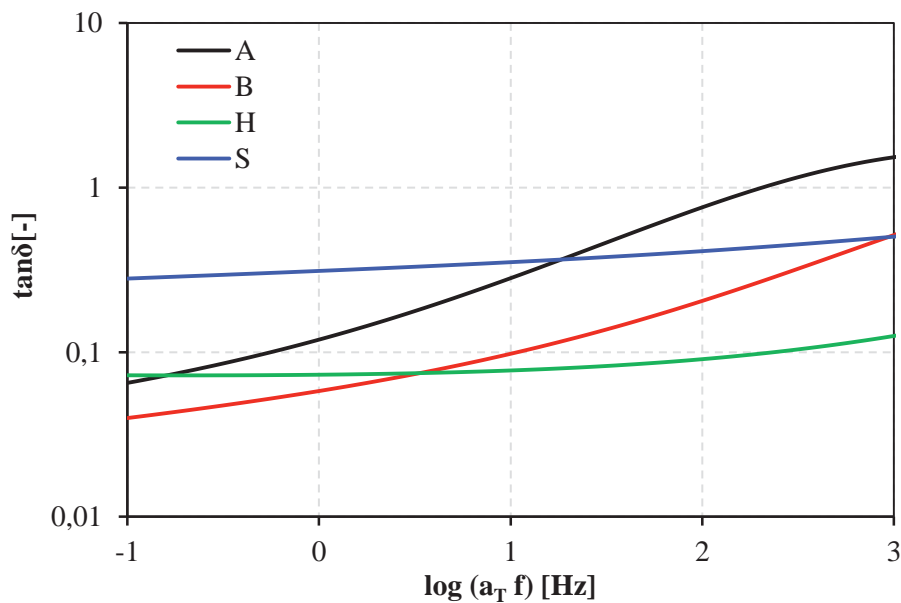
Fig. 5.9: Cut out of tanδ mastercurves from 0.1 Hz to 1000 Hz. Original mastercurves are shown in Fig. 5.5.

Although a sort of correlation between loss factor and friction values exists and is also widely used by the tire community [121] [122], it is worth to point out, that, the description of the hysteresis friction coefficient cannot be entirely based on *tanδ* as a single parameter. Other information, such as indentation depth, contact area, deformation field in the rubber, must to be considered, if a more accurate description of friction is required.

Fig. 5.10: Schematic representation of the hysteresis friction behavior for model substrates with different distance between the asperities. A shifting of the friction curve is expected of a factor equal to the wavelength ratio.
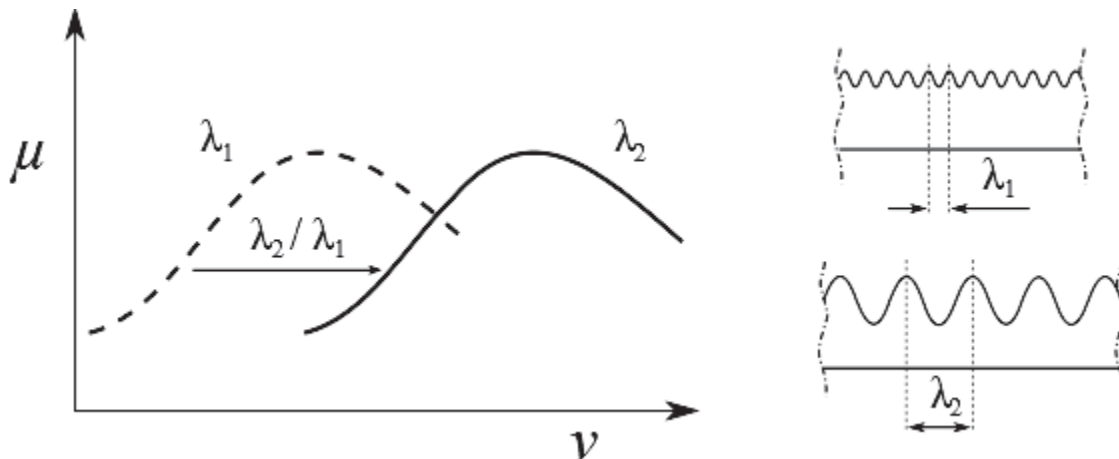
In order to verify the effects of the substrate geometry and the characteristic contact length on the hysteresis friction behavior [65] [84], the model compounds were tested on two different multi-indenters (described in sec. 4.4.1, Fig. 4.6). The theoretical expectation is that for the same indenter aspect ratio but different distance between the asperities, the friction curve would be shifted along the velocity axis of a factor equal to the wavelength ratio. In particular for a smaller wavelength a shifting to lower velocities is expected. Otherwise, if the friction coefficient is plotted against the corresponding frequency of excitation, an overlapping of the curve should be obtained, like schematically illustrated in Fig. 5.10. The measurements concerning the sinusoidal like multi-indenters confirmed the theoretical expectations for both model compounds. Although the effect of the asperity distance was verified under several experimental conditions, in terms of temperature, pressure and velocity, in Fig. 5.11 just the most representative examples have been shown.
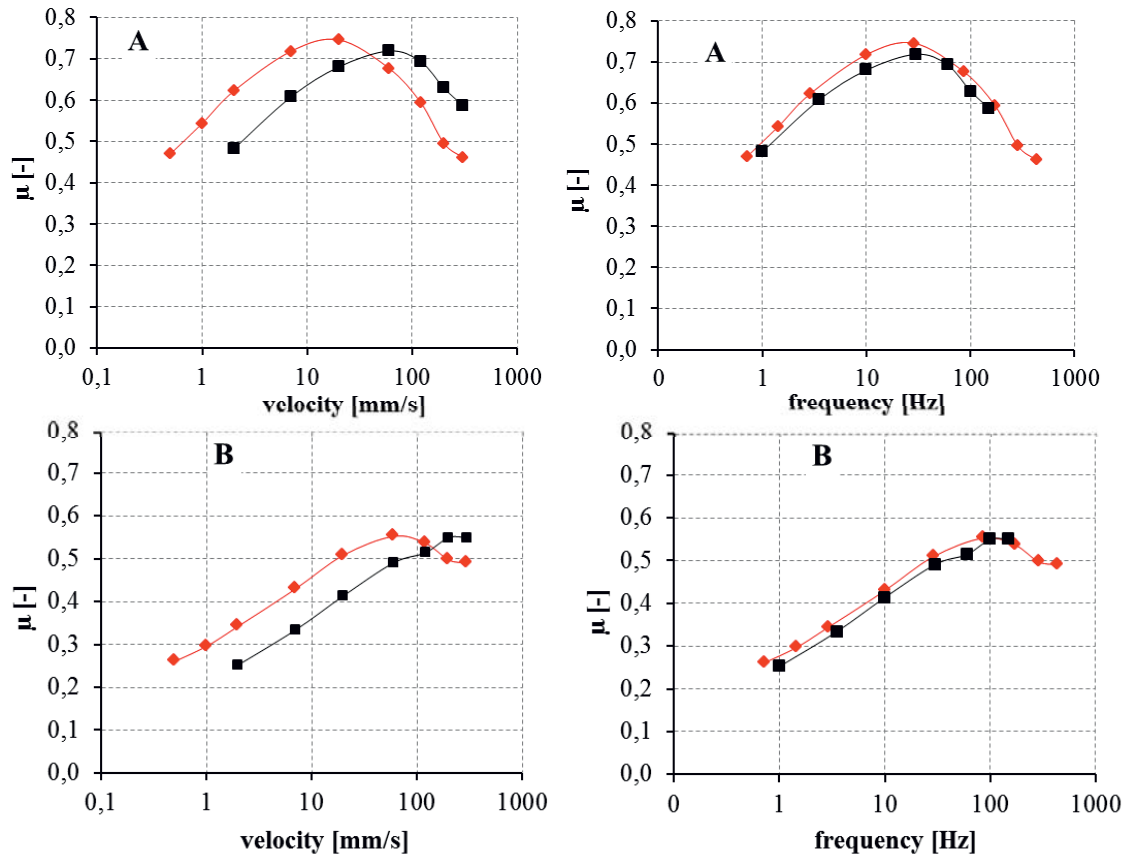
Fig. 5.11: Friction measurements for model compounds A (up) and B (bottom) for the two different multi-indenters and transformation from velocity to excitation frequency. Black squares = 2 mm multi-indenter; red diamonds = 0.7 mm multi-indenter. Compound A tested at 15 °C and compound B tested at 5 °C.

The result shown in Fig. 5.11 is one more evidence of the viscoelastic nature of the hysteresis component of the friction, which then results to be directly affected by the excitation frequency induced by the asperities in the rubber, hence, confirming the reliability of Grosch's theory [65] (see Fig. 2.3).

A topic of interest is, however, how the strain is distributed within the sample during tribological processes. In the following sections this topic will be analyzed by means of advanced measurements technique and finite element methods.

5.2.1. Dual-layer samples

As already observed in the previous section, the model compounds A and B show a different friction behavior despite their similar stiffness. In order to demonstrate that hysteresis friction is related to bulk viscoelastic properties, friction measurements have

been performed using dual-layer samples. These samples consist in two layers of material A and B co-vulcanized in different thickness combinations, as illustrated in Fig. 5.12. In particular compound A was arranged in the layer facing the substrate and compound B located in the remaining part of the sample facing the sample holder. Two different variants have been prepared: one featuring a thinner A-layer, dL-1, and one with a larger A-layer, dL-2. The overall thickness of the specimen was in both cases the same.
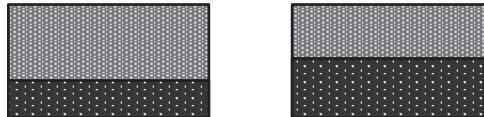
Fig. 5.12: Schematic configuration of the dual-layer samples.

The friction coefficient of sample A, B and the dual-layer has been measured sliding over the multi-indenter2mm surface and compared with each other. The resulting friction curves are plotted in Fig. 5.13. The transition of the measured curves demonstrates that for rubbery materials the viscoelastic dissipation occurring in the bulk is the origin of hysteresis friction and that not only the surface properties affect friction. If the same friction tests are performed using the smaller multi-indenter (Fig. 5.13 Fig. 5.14), the transition of the friction curves has a different trend compared with the bigger multi-indenter. Therefore, the thickness of the material involved by the dynamic excitation cannot be easily determined because it depends on many factors like substrate roughness, rubber stiffness, normal load and velocity.

Fig. 5.13: Friction curves for the dual-layer and single compound samples sliding over the multi-indenter 2 mm. Liquid soap used as lubricant at the interface, the temperature was 20°C and contact pressure 3.5 bar.
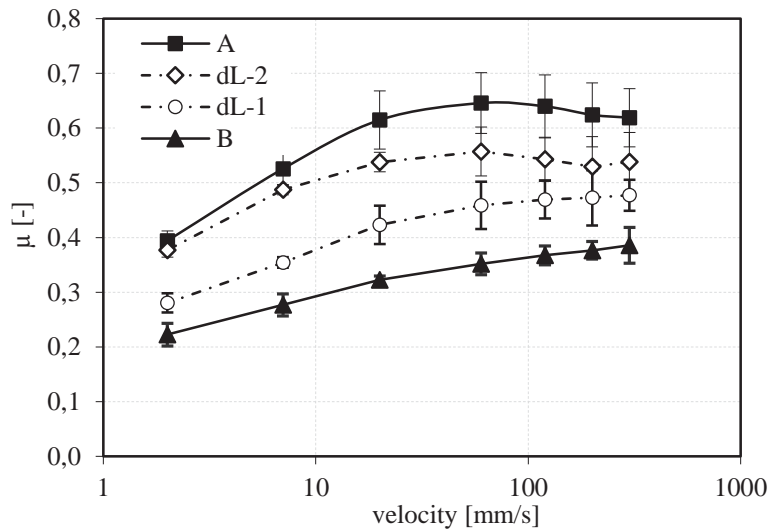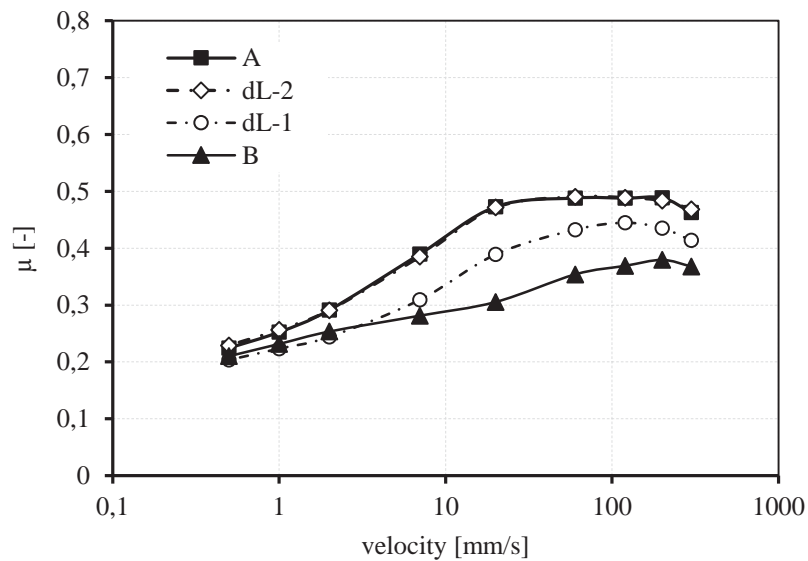

Fig. 5.14: Friction curves for the dual-layer and single compound samples sliding over the multi-indenter 0.7 mm. Liquid soap used as lubricant at the interface, the temperature was 20°C and contact pressure 3.5 bar.

5.2.2. Optical measurements

In order to have information about the deformation occurring in the sample during sliding and the possibility to perform a quantitative estimation of the hysteresis friction, optical metrology measurements have been carried out. The friction tests and the processing of the deformation analysis by the ARAMIS software have been performed according to the methods described in sec. 4.4 and 4.6. In Fig. 5.15 a frame of the sample A sliding at 60 mm/s is shown. The Mises strain has been calculated and graphically represented as a color map (blue for the minimum and red for the maximum value, 10% and higher).
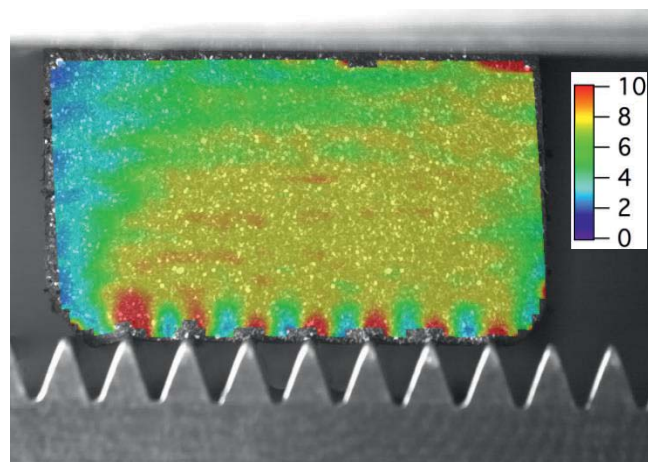
Fig. 5.15:   ARAMIS analysis of the Mises strain for the sample A sliding at 60 mm/s over the multi-indenter 2 mm. The multi-indenter is sliding from left to right while the sample is fixed on top.

From the graphical representation it is possible to see that the highest deformation originates in proximity of the asperities tip and the bulk is characterized by a nearly uniform strain level about 7%. To determine the hysteresis due to the cyclic deformation, it is necessary to calculate the dynamical deformation, which means how the strain field changes with the sliding time when the asperities are moving below the rubber sample. In this special case of the sinusoidal multi indenter, the deformation field is expected to periodically repeat with a time period $T = \lambda/v$, where λ is the distance between the asperities (in this case 2 mm) and v the sliding velocity.

Thanks to the optical metrology technique it was also possible to measure the displacement of a certain material point during sliding, so that the assumption of sinusoidal excitation

could be validated. In particular, two points, aligned to the vertical direction, where chosen and their displacement has been plotted against the sliding time (Fig. 5.16).

Fig. 5.16: Vertical displacement of material points located at increasing distance from the contact interface as a function of the sliding time, with reference to the figure on the left.
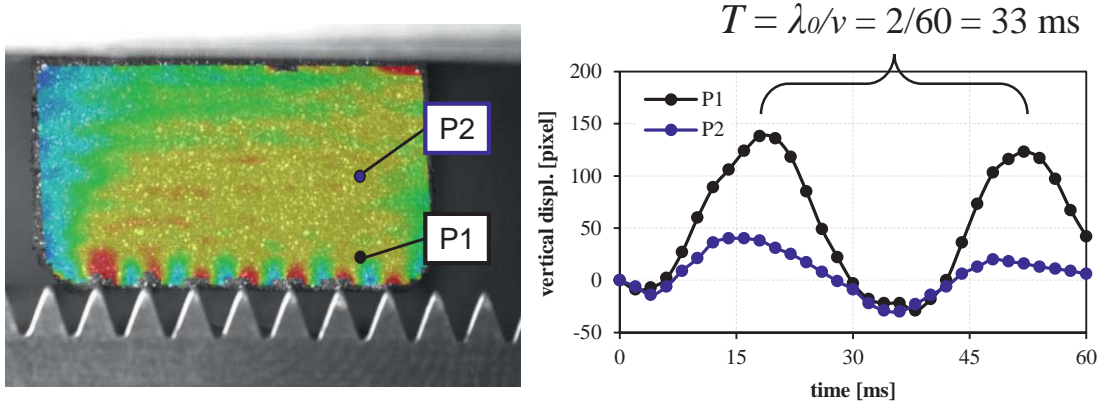
The point P1, located on the bottom area, showed a larger displacement compared with the point P2 located in the bulk. The trend of the curves confirmed, moreover, that a sinusoidal-like excitation occurs during the dynamic indentation and that the period is in good agreement with the theoretical estimation: $T = \lambda/v$. Such validation made it possible to calculate the contribution to hysteresis friction following the guideline described in sec. 2.2.1. The operation has been performed for each element, i, of the mask overlaying the sample surface calculated by the ARAMIS, under the assumptions of constant strain in the thickness direction and linear viscoelastic behavior.

$$\mu_{H,v} \cong \frac{\pi}{F_N \lambda_0} \sum_i V_{si} E''(\varepsilon_i, \omega_0) \varepsilon^2{}_i = 0.06 \tag{60}$$

The hysteretic portion of the friction coefficient, calculated according to Eq. (60), for sample A sliding at 60 mm/s, turned out to be about six times smaller than the value measured by the friction tester (μ_H calculated = 0.06; μ_H measured = 0.38). Such a large difference between the measured and the estimated value could be partially explained if we consider that the resolution of the used equipment is not enough to reach a proper estimation of the deformation field occurring in the sample. Nevertheless the assumption of linear viscoelasticity could also be a strong effect on the real estimation.

85

Moreover, for this analysis, the surface of the indenters was assumed to be completely smooth, even if in reality a fine roughness will be present on the top part of the asperities, which could give additional contribution to raise friction forces. These assumptions will be better clarified in the next paragraphs, where, some additional information can be provided thanks to Finite Element Method calculations.

5.3.   Finite Element Analysis for friction

One of the main outcomes of the investigation described in the previous chapter is that any layer of the sample contributes to friction interaction. Since an accurate detection of the deformation occurring in the specimen turned out to be quite complicated to achieve by the ARAMIS analysis method, it was decided to study the contact mechanisms by use of Finite Element Methods (FEM).

5.3.1.   Material modeling

In case of dynamic problems like sliding friction, the time dependent mechanical behavior of viscoelastic materials, like rubber, has a crucial impact on the accuracy of the FEM solution. Although it is not a trivial task, a good material modeling is necessary to perform accurate and reliable calculations. In the present work a linear viscoelastic material model based on the generalized Maxwell model has been adopted (more details in sec. 3.2.2). The determination of material parameters has been carried out by fitting the mechanical behavior of both quasi static and dynamic tests. In particular, the stress-strain curves have been measured under quasi-static conditions, in three different strain modes. In order to get rid of the Mullins effect, the 5th cycle was selected and then the middle line of the hysteresis load/unload cycle was calculated, so that it could be used as a reference to fit the long term material behavior. In Fig. 5.17 the fitting result, obtained using both Yeoh and Neo-Hooke model, in case of compound A, is shown. The fitting has been optimized up to a strain level of 35% according to the maximum strain level measured by the ARAMIS system. For Yeoh model the following parameters were used: C_{10}: = 0.584; C_{20} = -0.129; C_{30} = 0.075; wile for the Neo-Hooke the only parameter C_{10} was equal to 0.59. Despite Yeoh model can generally better estimate the material properties in different strain modes, Neo-Hooke model in most cases turned out to be accurate enough to get satisfying results. For this reason, Neo-Hooke model has been used for each other compound to describe the long term component. The respective values are presented in Table 5.
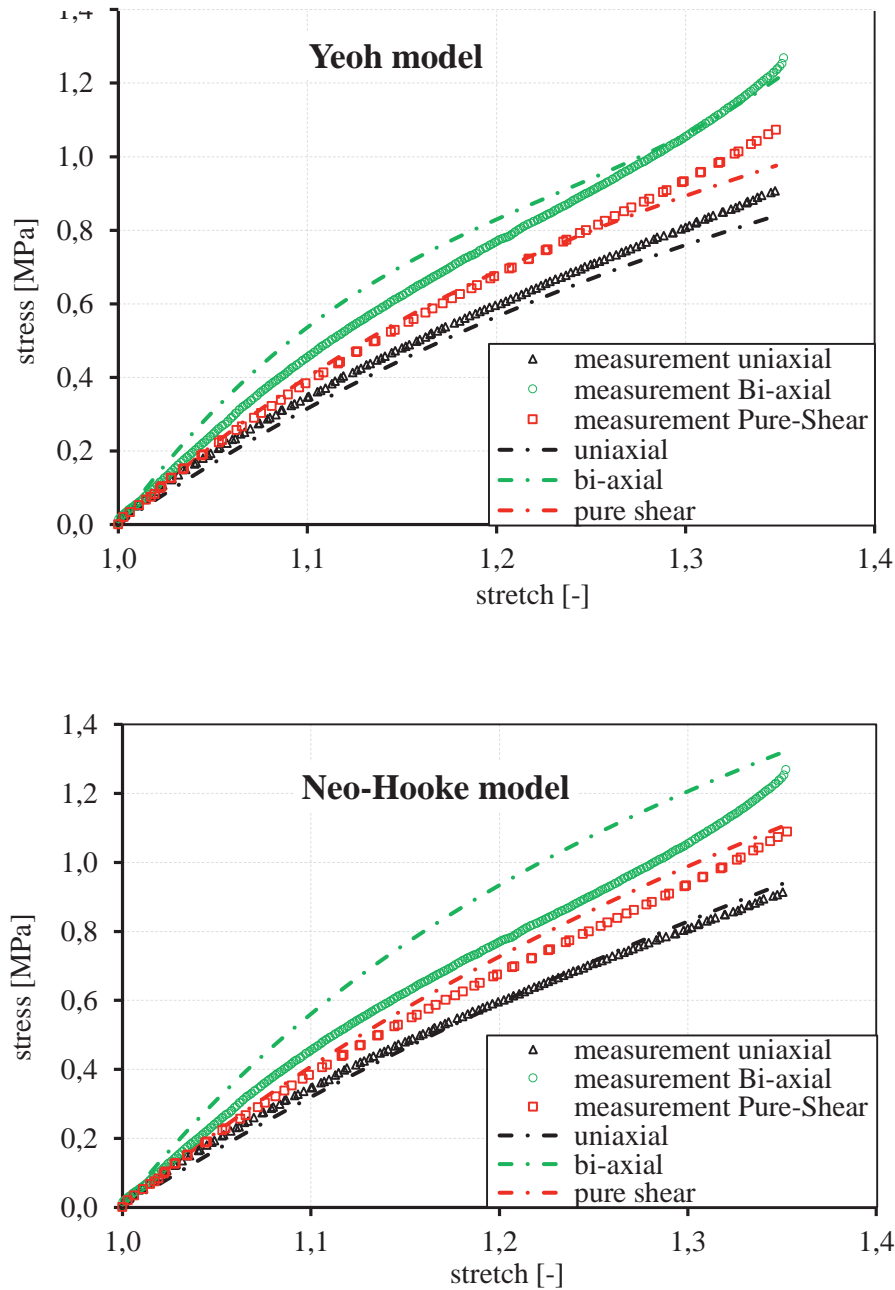
Fig. 5.17: Fitting of the Yeoh model (up) and Neo-Hooke model (down) with the stress-stretch curves measured in uni-axial, bi-axial and pure shear at 20°C for the compound A.

Although quasi static behavior is important to get the general compound stiffness, the part which has the main influence on friction behavior is the viscoelastic one. Based on the formulations described in the theoretical section 3.2. it was possible to determine the time dependent behavior by fitting a Prony series with the dynamic moduli mastercurve in the frequency domain. The fitting have been performed on the high strain mastercurve (2.5% strain) according to the limit of the testing equipment. The resulting best fit of the dynamic mastercurve for different compounds is shown in Fig. 5.18. 70 to 80 elements have been

used for the fitting, depending on the specific compound. The values of g_i and τ_i are listed in Table 7 and Table 8 table in appendix A.

Table 5:   Neo-Hooke parameters for the compounds used in the investigation.

sample	C10
A	0.59
B	0.66
H	1.47
S	0.45

In order to verify that the material model implemented in ABAQUS could reproduce the real material behavior, a crosscheck, between the strain response measured by a machine and the one simulated by FEM under dynamic load, was performed. More specifically, a rubber sample of 10 x 10 x 10 mm was tested under compression mode using Eplexor Gabo with 20 N preload and 30 N peak-to-peak dynamic load at different frequencies. In this way the measured stress-strain response of the material subjected to different strains during the frequency sweep could have been compared with the FEM calculation. These simple tests, besides providing information concerning the accuracy of the material model, allow understanding the complexity of the mechanical behavior of rubbery materials. Taking into account that all samples have been subjected to the same dynamic load, the inclination angle of the loop of Fig. 5.19 represents the material stiffness while the loop area is the hysteresis loss. This means that, at 10 Hz of excitation frequency and 20°C, samples A and B have a similar stiffness but different dissipative behavior as expected, and that sample H is the stiffest among the model compounds.
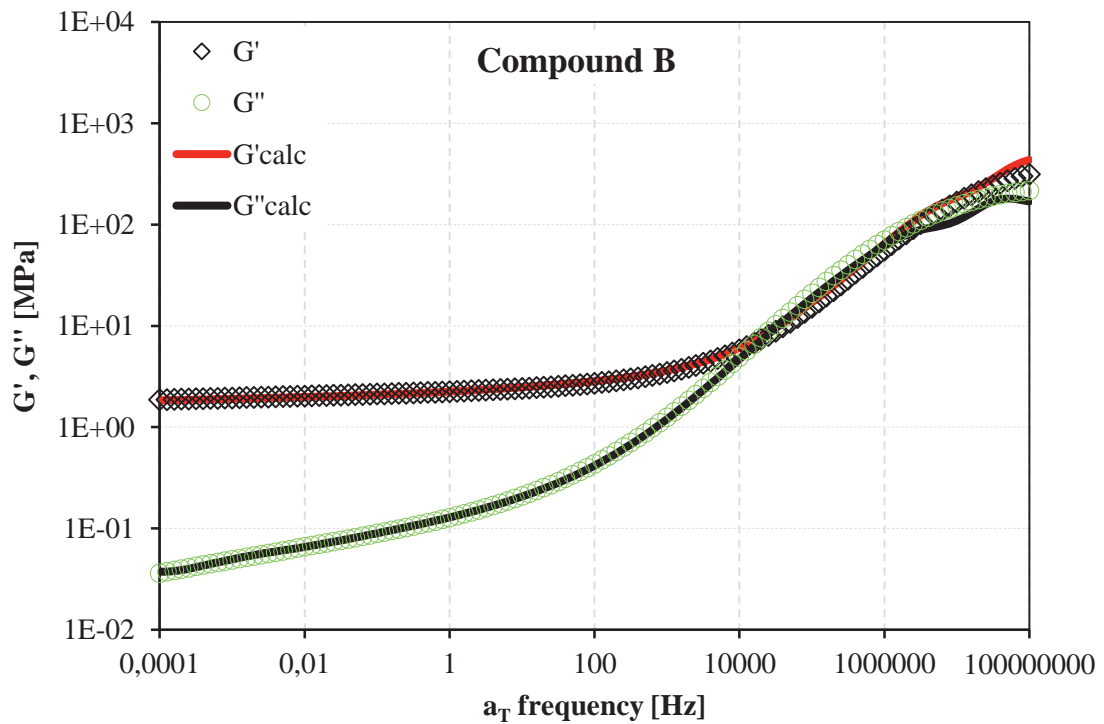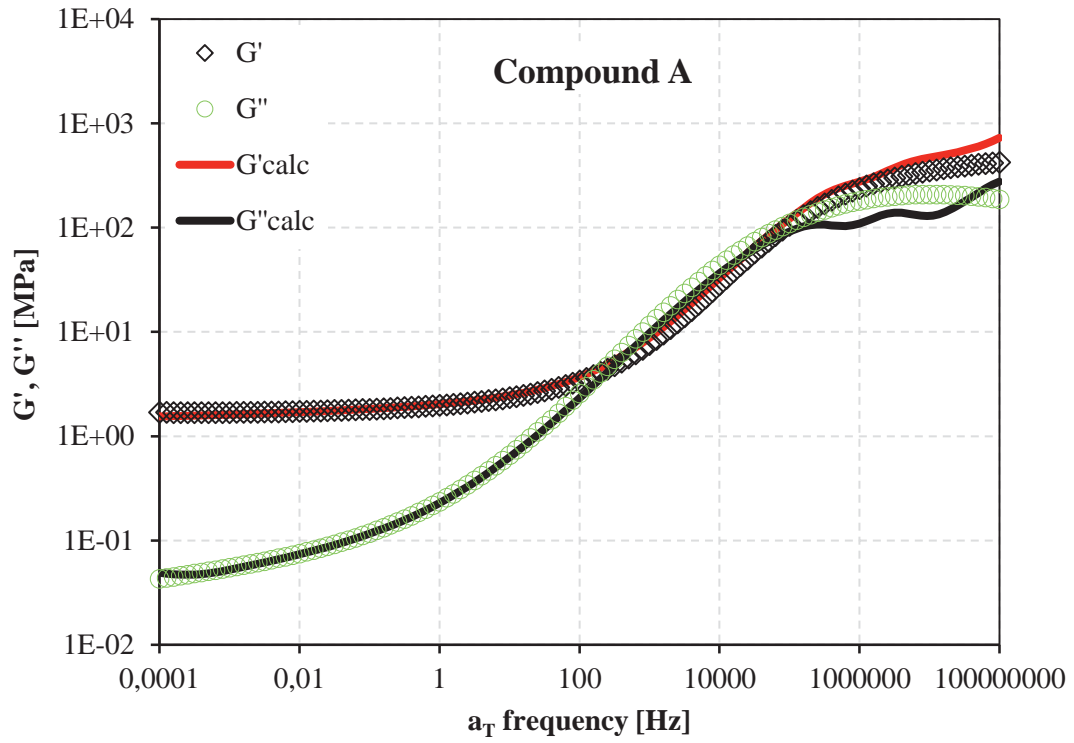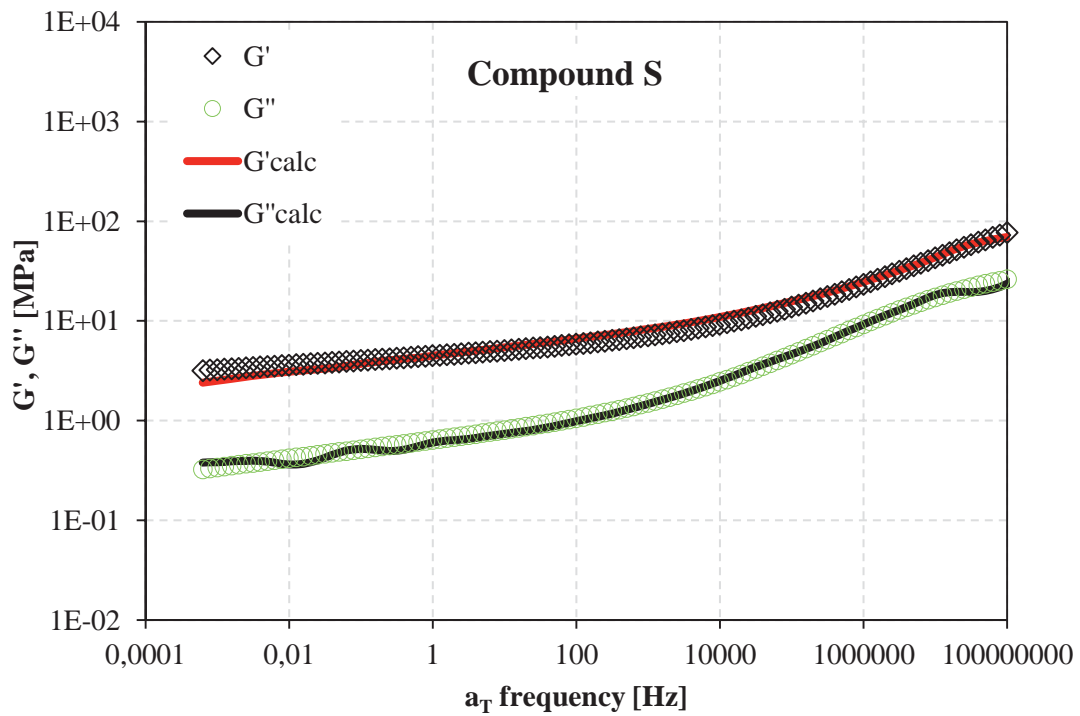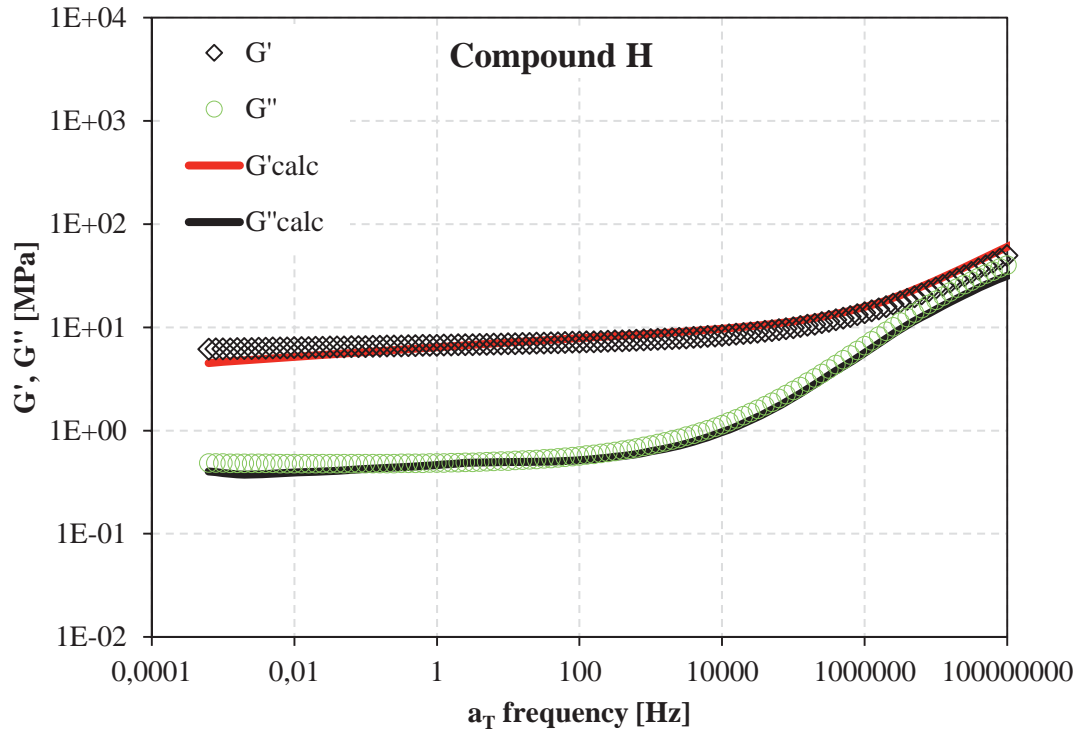
Fig. 5.18: Fitting between the Prony series and G', G'' mastercurve for different compounds. Reference temperature = 25°C; strain level = 2.5 %.
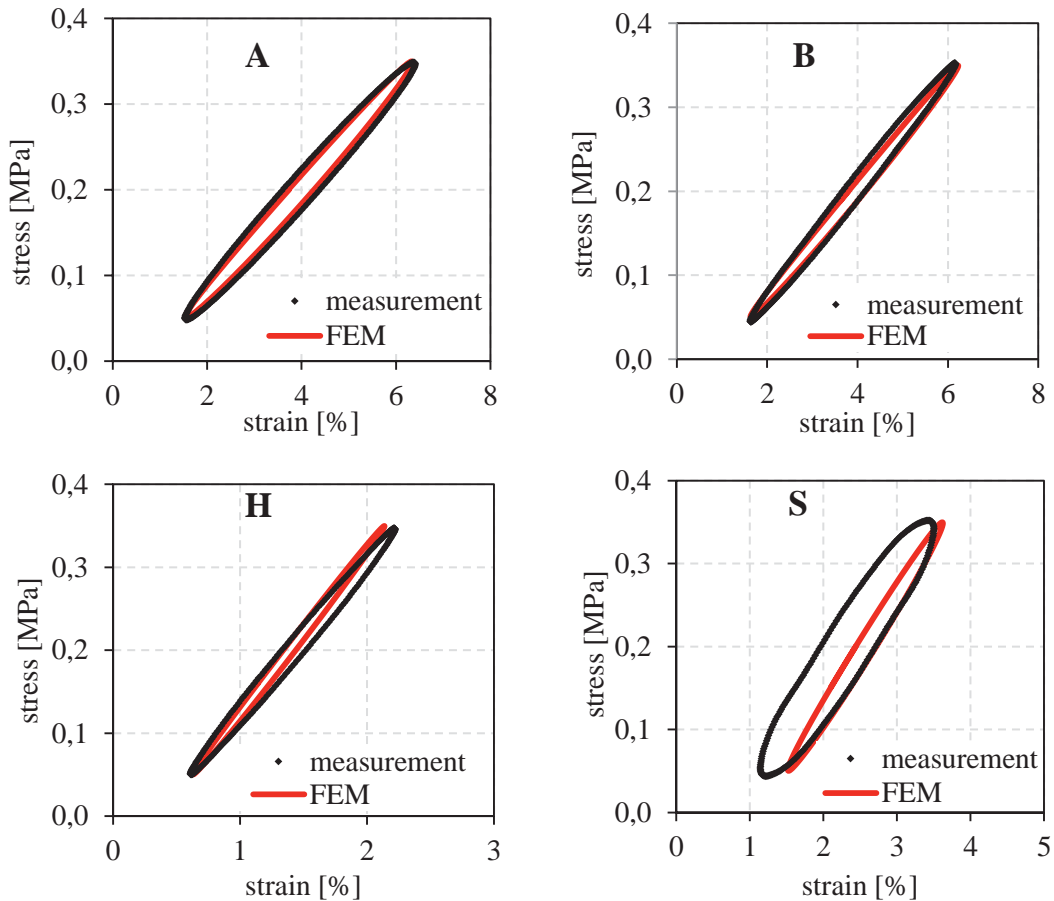
Fig. 5.19: Comparison between Gabo measurement and FEM simulation in case of a dynamic test carried out in compression at the frequency of 10 Hz. Sample A (top left), B (top right), H (down left), S (down right).

The comparison with numerical simulations shows that ABAQUS calculations are capable to predict quite well the material stiffness while the hysteretic prediction is not completely accurate even at relatively small strain amplitudes. This means, despite the fitting of Prony series seems to reproduce the experimental mastercurves with a fair agreement, with a closer look to the curves a small error can be detected. Such small error, especially on G'' induces a consequential mistake on the prediction of the hysteretic behavior of the material. More specifically, if ideal linear viscoelastic behavior is considered, the dissipated energy scales linearly with loss modulus. Therefore a linear correlation is expected between dissipated energy error and loss modulus fitting error.

The difference between the measured and calculated loop area $\varDelta E_{loop}$ has been quantified and compared with the fitting error on G'' in Fig. 5.20. The diagram shows that the experimental results respect a linear trend, thus confirming that the accuracy of the Prony series needs to be extremely good in order to get reliable prediction. Asides this mistake, it

is also important to keep in mind that a linear viscoelastic model cannot be adequate to predict rubber materials behavior in each circumstance.
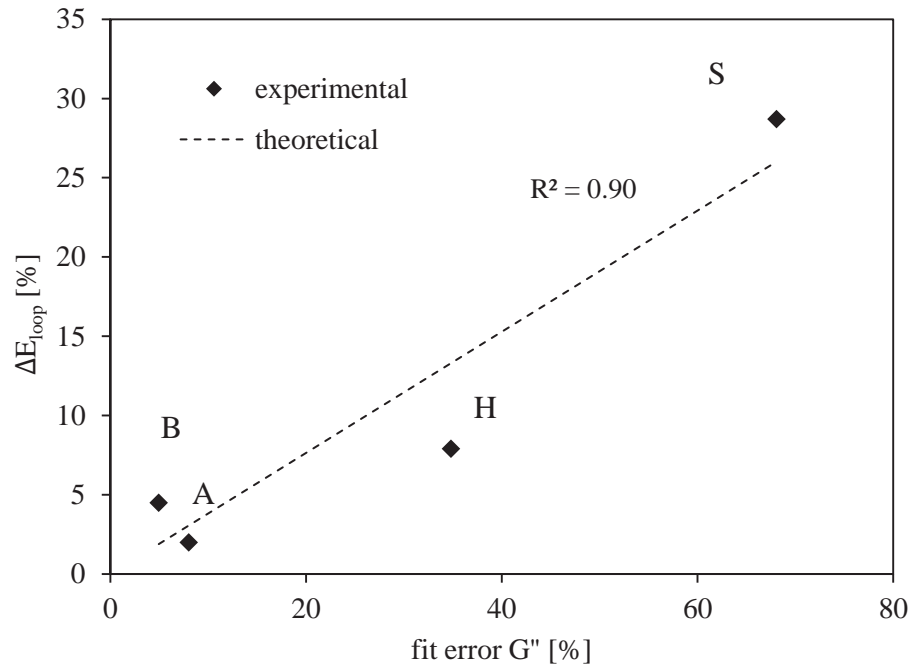
Fig. 5.20: Correlation between error in estimation of dissipated energy and error deriving from the Prony series fitting of the loss modulus.

5.3.2. Simulations for model surfaces

In order to have more details about the hysteresis generating during sliding, FEM simulations, reproducing the friction experiments, have been performed in ABQUS environment. For this purpose, a two dimensional FEM model was developed, based on the measurement set-up features in case of model surfaces. In particular, the multi indenter, used as a substrate for the friction tests, has been modelled as analytical rigid line, reproducing the same geometry of the manufactured component, while the rubber specimen has been modeled as deformable viscoelastic material, consisting of plain stress solid quadratic quadrilateral elements of type CPS8R. The problem was designed in two steps. In the first one the sample is pushed against the indenter with the same pressure applied for the experiment. In the second step, the substrate is horizontally moved at a constant velocity and the sample is let free to move only in the vertical direction. The normal load is

constantly acting as boundary condition on the rubber specimen. It is worth to point out, that, in order to analyze only the hysteretic contribution, a frictionless interaction was set between the two surfaces in contact. The simulation was performed under isothermal conditions, so eventual heat generations induced by energy dissipation within the sample, have not been taken into account.
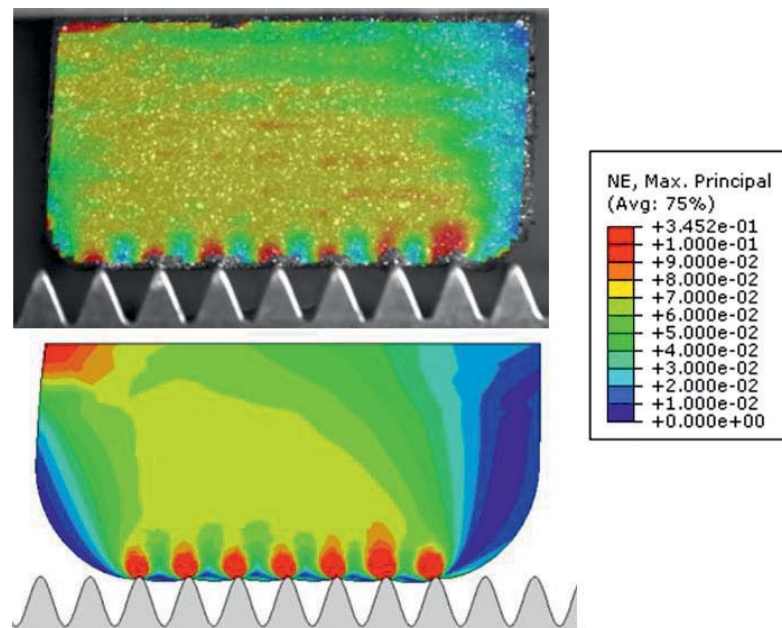
Fig. 5.21: Deformation comparison between ABAQUS simulation and ARAMIS analysis in case of sample A sliding at 60 mm/s over the multi-indenter 2 mm.

The graphical result of the FEM simulation for sample A sliding at 60 mm/s over the multi-indenter 2 mm is shown in Fig. 5.21. Comparing the FEM simulation with the analysis performed by the ARAMIS, it is possible to see that the strain field generated in the sample is qualitatively similar, thus, confirming the good accuracy of the FEM calculation. Besides the deformation picture, a quantitative analysis of the reaction forces acting on the sample and the trend of dissipated energy during sliding time can be performed, as shown in Fig. 5.22. The average friction force is a little bit higher than 20 N, which means a friction coefficient of 0.35, considering 60 N normal load. It is once again important to remark that tangential interactions are not active between the sliding surfaces, so the friction value comes only from the contrasting action exerted by the viscoelastic matrix when it's pushed by the asperities. The hysteretic friction coefficient can, in principle, also be determined based on energetic considerations. Indeed, in case of regular multi-indenter Eq. (61) allows

94

to calculate μ_H considering the dissipated energy and the sliding distance, or better, the number of indentations:

$$\mu_H = \frac{1}{F_N} \frac{E_{diss}}{n\lambda_0} = \frac{1400mJ}{60N * 30 * 2mm} = 0.38 \tag{61}$$

As the two values calculated using different approaches are very similar, the formula based on the correlation between hysteresis friction and dissipated energy has proven to be valuable. Therefore, the underestimation of the friction coefficient calculated by the optical metrology technique comes, most likely, from the low resolution of the ARAMIS analysis.
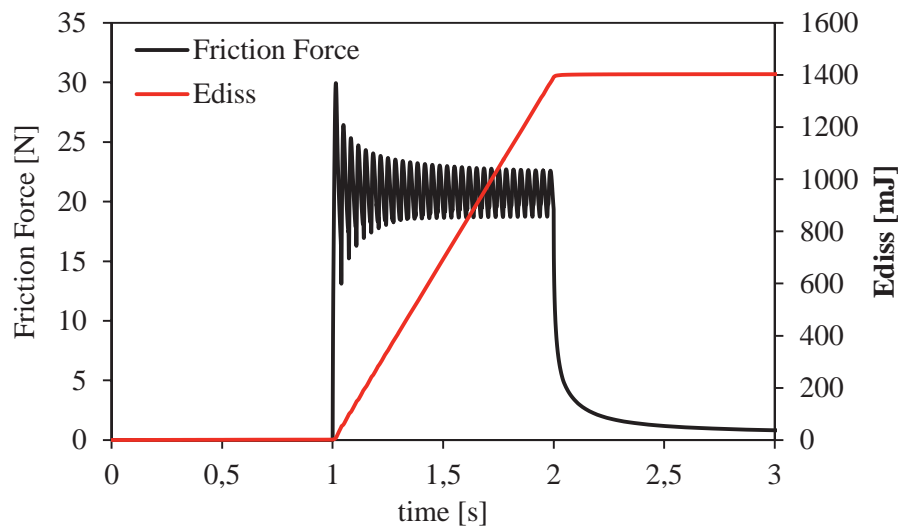
Fig. 5.22: Time evolution of friction force and dissipated energy for a FEM friction simulation of sample A sliding over multi-indenter 2mm. From 0 to 1 s the normal load is applied; from 1 to 2 s sliding stage (60 mm/s); from 2 to 3 s stop driving stage.

The friction coefficient was then calculated for different velocities and for the 4 model compounds, so that a comparison with measurements could be done. The comparison has been split on two different diagrams to avoid overlapping of data points.
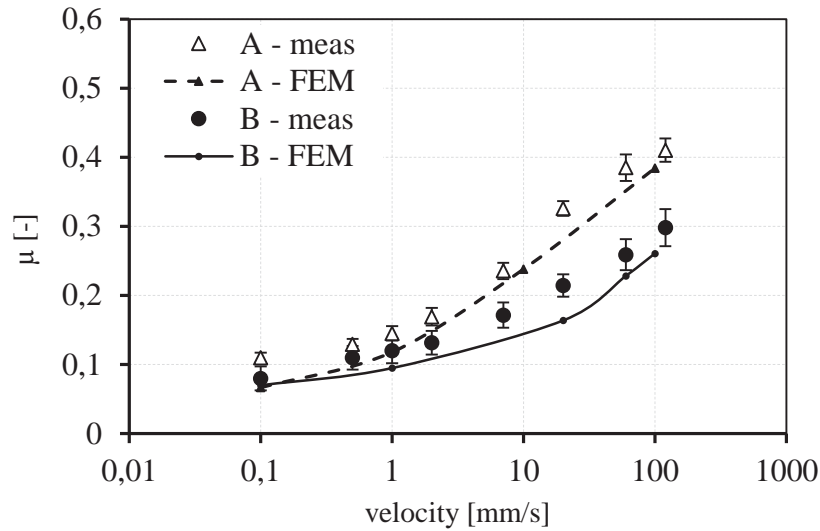
Fig. 5.23: Comparison between measured friction and FEM simulation hysteresis friction for compound A and B at 20°C and 3.5 bar nominal pressure. Multi-indenter 2mm used as substrate.
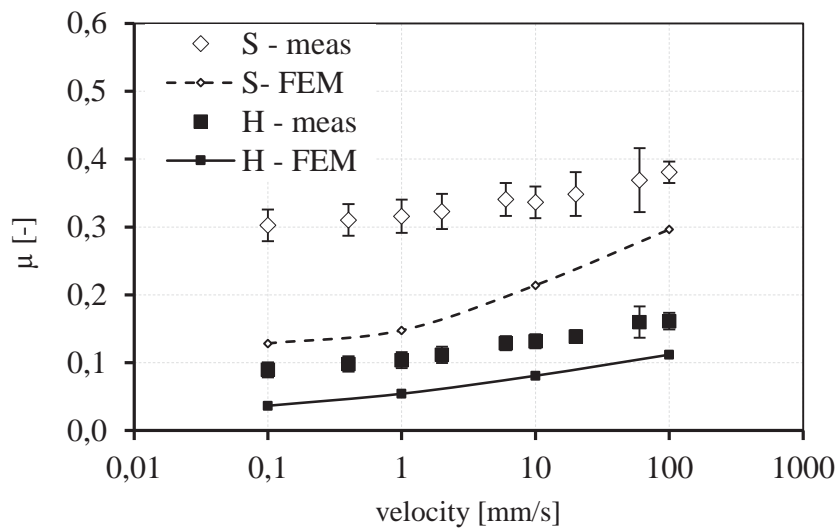
Fig. 5.24: Comparison between measured friction and FEM simulation hysteresis friction for compound S and H at 20°C and 3.5 bar nominal pressure. Multi-indenter 2mm used as substrate.

The prediction of friction values is quite accurate in case of compounds A and B, Fig. 5.23, while an underestimation from 30 to 50% is observed in case of the compounds H and S, Fig. 5.24. The accuracy of the simulation depends, as expected, on the material behavior. Therefore, as previously shown in Fig. 5.20, the material behavior for compounds A and B is better simulated than H and S due to the weakness of the Prony series to describe rubber non-linearity in several cases. The fact that in some cases the gap is smaller than in other

cases depends also on the existence of a possible residual adhesive interaction which can be more or less pronounced according to the wettability and polarity of the compound.

Such result demonstrates that FEM analysis can be used as a good tool to describe the phenomenology of friction interaction but a realistic estimation of the friction properties, for every kind of rubber compound, is still challenging and related to many other variables, like the impossibility to isolate experimentally adhesion and hysteresis.

However, one possibility is to use FEM simulations to verify the effect of different multi-indenter size. Friction curves have been calculated for both model substrates, presented in Fig. 5.25, using compound A.
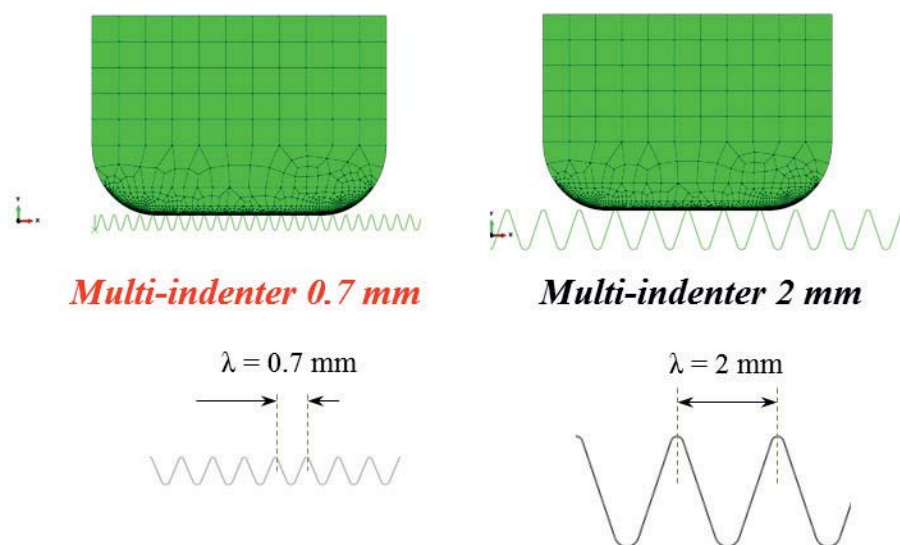
Fig. 5.25: Sketch of the FEM models used to calculate the friction values for the two different multi-indenters: small indenter (left side) and large indenter (right side).

In fact, the simulated friction curves appear separate if the sliding velocity is considered (left plot of Fig. 5.26) but they overlap if the equivalent excitation frequency (right plot of Fig. 5.26), is taken into account.

The result confirms the reliability of FEM simulations, since they are in fair agreement with the experimental findings presented in sec. 5.2, enhancing once again the intuitions of Grosch published in [65].
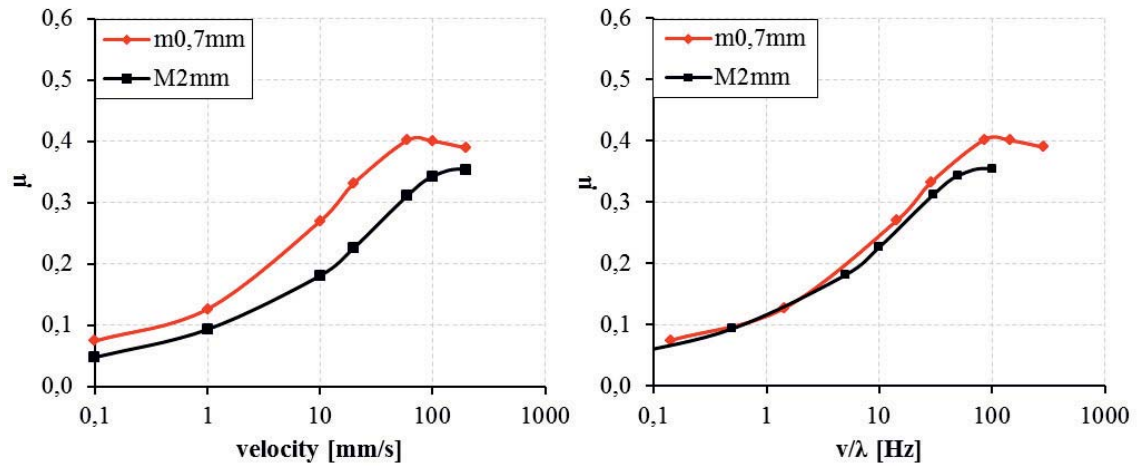
Fig. 5.26: Friction calculation by FEM analysis for two different multi-indenters using sample A with 3 bar nominal contact pressure and 20°C material properties. The transformation from sliding velocity to excitation frequency is shown in the right chart.

5.3.3. Analysis of different roughness scales on hysteresis friction

FEM simulations turned out to be capable to estimate the hysteresis friction in case of model regular surfaces, as long as the material model is capable to describe the viscoelasticity in a proper way. As already explained a fair trend with the Prony series fitting is not enough to predict any other physical behavior which is part of the predicting algorithm (see Fig. 5.20).

However, any surface which is in contact with rubber goods shows a random rough distribution [123] [124] [125] [126]. For this reason, FEA was used to study the friction interaction taking place, at least from a modelistic point of view, when the substrate is made up of different roughness scales or of a superposition of them.
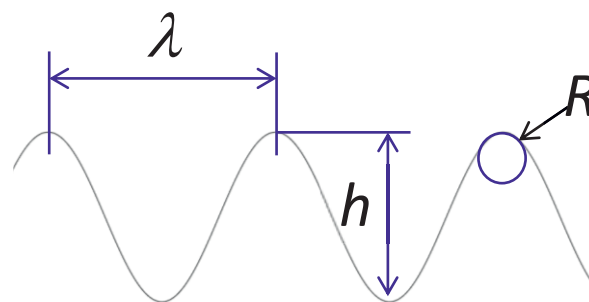
Fig. 5.27: Sketch of the geometrical parameters of a sinusoidal substrate. λ is the asperity distance; h the asperity height and R the asperity radius.

Referring to Fig. 5.27 four sinusoidal substrates have been designed choosing a systematic variation of the length scale so that macro, meso and microscale could be respectively investigated. The geometrical parameters of the surfaces are listed in Table 6. In particular, the *macro* indenter has a wavelength, λ, as well as an asperity height, h, in the millimeter scale. Substrate *meso* has been designed with a wavelength one decade smaller than the *macro*, and an asperity height in the same range. The multi-indenter *micro,* with a wavelength 100 smaller than the *macro* indenter, should represent the µm scale. In this way, it was possible to investigate the hysteresis friction for substrates presenting a roughness on three different length scales and what happens when the scales are combined.

Based on the higher accuracy reached for the material model and on the agreement of its simulations with measured data, compound A was selected to carry out all the FEM calculations for the indenters of Table 6.

Table 6: Geometrical features of the sinusoidal substrates used for FEM calculation

name	h	λ	R	h/λ
		mm		
macro	0.7	1	0.0730	0.7
meso	0.1	0.1	0.0050	1
micro	0.004	0.01	0.0013	0.4

In this case, a good reliability is expected to be provided by the simulations. The nominal contact pressure used was constantly set to 3 bar. The results, shown in Fig. 5.28, demonstrate the impact the substrate morphology has on hysteresis friction. More specifically, it is possible to observe a shifting of the friction peak of a decade if substrates *macro* and *meso* are compared. This effect comes from the factor 10 adopted to rescale the wavelength of sinusoids, which determines a shifting of the frequency of excitation induced in the rubber of a factor 10 as well, with the consequential shifting of the friction curve. This result has been already presented and experimentally verified by measuring with the two different multi-indenters (sec. 5.2), but unlike the case of Fig. 5.26, now it can be seen that the maximum of the friction curves reaches different heights. Such a difference can be explained considering the different shape factor of the asperities, namely the h/λ ratio, which in turn produces a different deformation in the rubber, so a different hysteresis. In particular, *meso* shows higher friction values due to the sharper shape of its tips. A similar effect is observed if *meso* and *micro* substrates are compared. Again a shifting of the friction peak of a factor 10 along the velocity axis occurs and the maximum value is lower due to the lower h/λ ratio. The effect of the asperity shape factor is outlined in Fig. 5.29 where the maximum friction value has been plotted against the respective h/λ ratio. The correlation found confirms that sharper asperities induce higher friction. This result is in line with Popov studies [127], which show a quadratic proportion between friction coefficient and root mean square of the surface gradient.
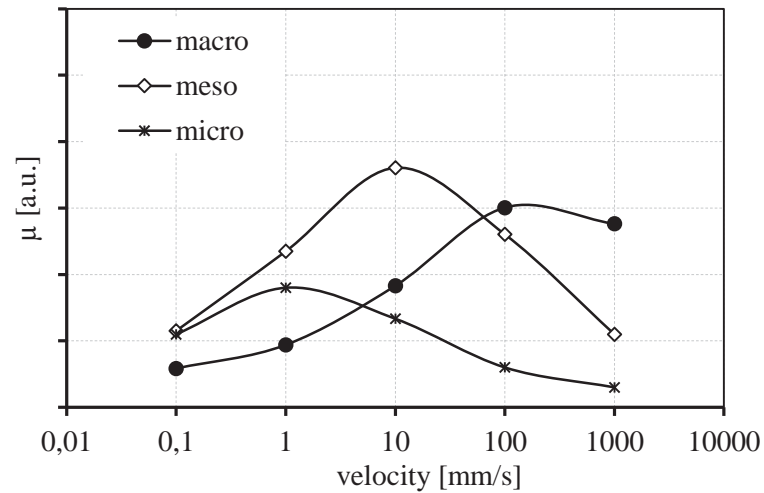
Fig. 5.28: Effects different length scale roughness on the hysteresis friction. Values calculated considering compound A and the sinusoidal substrates of Table 6, with a nominal contact pressure of 3 bar.
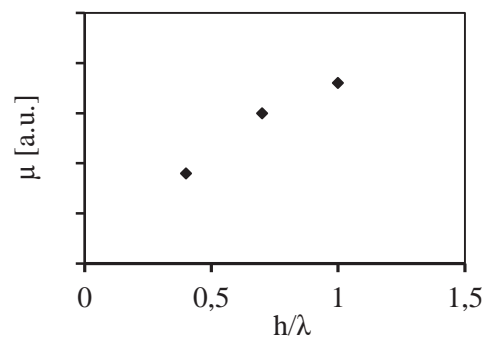
Fig. 5.29: Effect of the shape factor h/λ on the hysteresis friction. Higher h/λ means sharper asperities, so higher hysteresis friction.

At this point the dependence of friction coefficient on substrate geometrical features, in case of a single roughness scale, has been presented, but the effect produced by the superposition of sinusoids still remains an open question.

For this purpose, FEM simulations have been carried out to estimate the friction behavior when two among the presented substrates are summed up, like shown in Fig. 5.30.
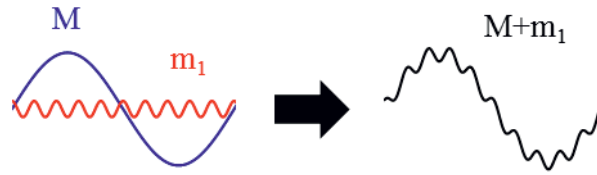
Fig. 5.30:   Example of the superposition of macro and meso sinusoidal substrates.

As preliminary investigation point, substrates *macro* and *micro* have been superposed to see the effects of a generic roughness scale superposition. ABAQUS calculations show that the superposed substrate friction curve has a broader shape as a result of the combination of both macro and micro roughness contribution to friction (see Fig. 5.31). The presence of 4µm height asperities on the macro scale indenters is shifting the grip level on a broader frequency domain. Indeed, as illustrated in Fig. 5.32 a broader hysteresis occurs at macro and micro scale. Moreover, the local pressure distribution, generating in case of superposed scales, is different compared with the case of a uniform single scale substrate, resulting in a different friction behavior.
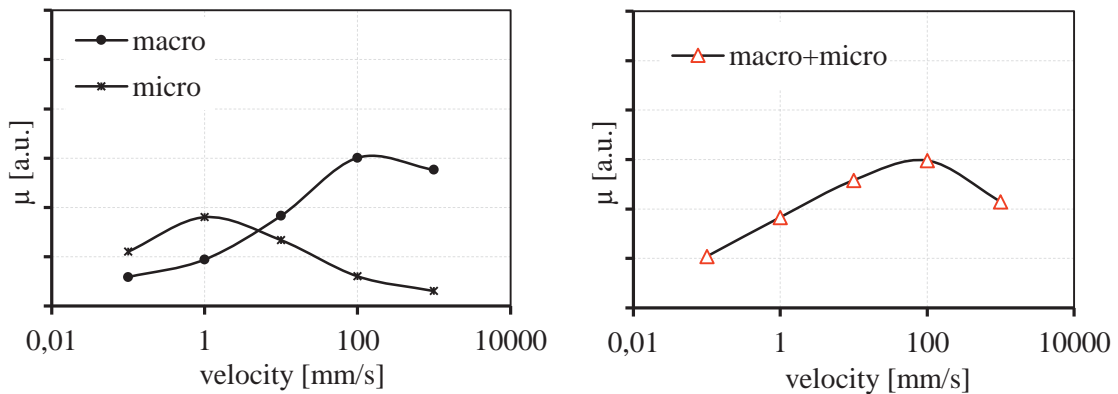
Fig. 5.31:   FEM calculation of hysteresis friction for sinusoidal surfaces *macro* and *micro* (left) and comparison with superposition of *macro+micro* (right).

Based on this result each contribution must be carefully considered [128] to provide pertinent hydrodynamic lubrication regime occurring in each condition [129] [130].
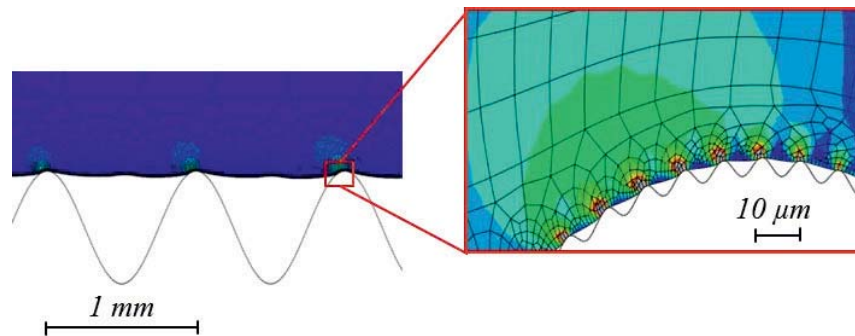
Fig. 5.32: FEM deformation analysis for macro and micro – roughness scale during sliding (indenters moving from right to left). The magnification insert shows the micro hysteresis deformation field occurring simultaneously to the macro hysteresis.

In case of rough surfaces, the identification of one or more roughness scales which are mainly affecting the hysteresis friction coefficient is not an easy task. It seems to be rather useful to consider the whole roughness spectrum, down to the μm scale, since not easily predictable effects take place when two or more scales are present at the same time.

5.3.4. Simulations for rough surfaces

Based on the agreement shown between FEM simulations and friction measurements over sinusoidal surfaces for compound A (correctly modeled by prony series), it was decided to perform FEM simulations for rough surfaces and compare the resulting friction curve with measurements carried out using water and water and soap mixture as a lubricant [131]. In this way, it could be validated the predictability of FEM simulations concerning hysteresis friction, in case of more complex surface textures, and also quantified the hysteresis expected in case of water wet friction. For this purpose, the same model used for sinusoidal surfaces has been adopted and extended introducing a rough profile as a rigid substrate. The surface profile was now not generated by CAD design, but using the list of points measured by whitelight interferometer microscopy. The analysis on model sinusoidal surfaces showed that hysteresis friction is strongly affected by the roughness spectra of the substrate over which the rubber is sliding. In particular, when more scales are present at the same time the resulting friction curve showed to be affected by each scale. In order to generate the rough surface in ABAQUS, whitelight measurements using a lateral resolution of 0.5 µm and a vertical one of 0.2 µm have been performed. Then a profile in the middle of the sliding zone has been selected as representative of the surface.

The two different pavers selected for the investigation are shown in Fig. 5.33. The granite paver shows a smaller roughness compared with the brick paver, which is similar to an asphalt surface, as it presents mineral aggregates bound together with a concrete matrix, laid in layers and compacted. The macroscopic difference between the substrates can be noticed observing bottom part of Fig. 5.33, where a 3D render of a magnification of 10 mm x 10 mm area is shown.

Fig. 5.33: Substrates used for the investigation: granite paver (left side), brick paver (right side). 3D Magnification render for a 10 x 10 mm² area on the bottom part.

The height difference correlation (HDC) function has been evaluated for both surfaces [110] [73] and reported in Fig. 5.34. The chart shows that the fractal dimension, indicated as the slope of the functions in the range between 10^{-5} and 10^{-3}, is similar for both substrates, and that the brick is rougher, since its function is lying about one decade above the granite one.
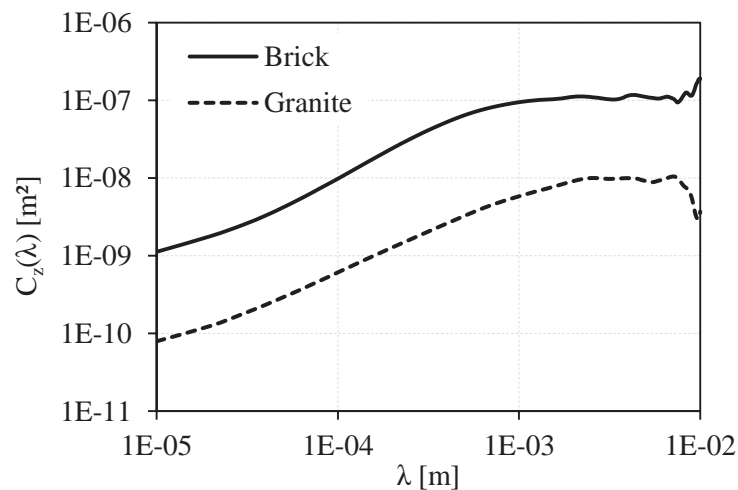
Fig. 5.34: Height difference correlation (HDC) functions for the brick and granite substrates.

FEM simulations have been performed using a representative line scan of the substrate with a two dimensional approach. During the sliding on this kind of surfaces the deformation, and so the hysteresis, occurs on different length scales, as shown in the Fig. 5.35, where an example of compound A, sliding over the granite at 10 mm/s is shown.
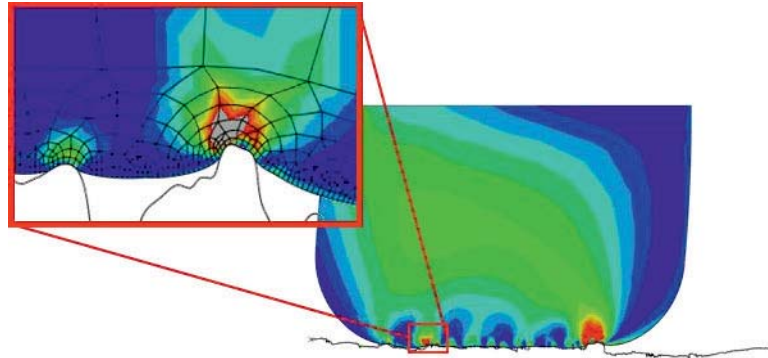
Fig. 5.35: Visualization of the deformation occurring in the sample on different length scales. Compound A sliding at 10 mm/s over the granite.

The hysteresis friction coefficient has been calculated in ABAQUS environment for both rough surfaces, using compounds A and H, in order to have one result for each of material class. The same compounds have been tested with the friction machine using water and water + 5% soap as lubricant, at 3 bar contact pressure and 20°C temperature. The results are shown in Fig. 5.36.

Similarly to what observed for friction simulations over model substrates, the simulations performed on rough surfaces agree with experimental results whenever the fitting error of the Prony series could be considered negligible (Fig. 5.19, Fig. 5.20).
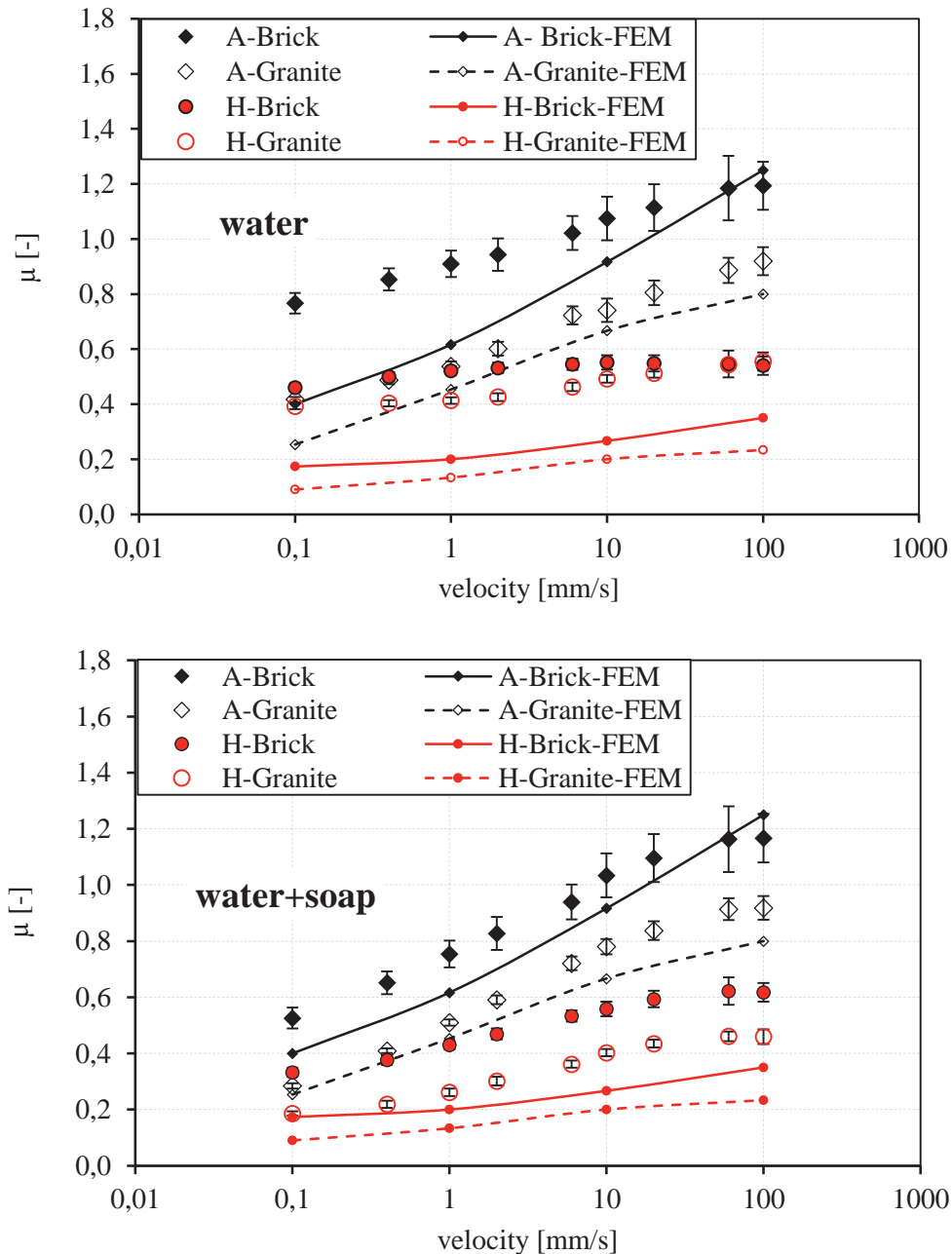
Fig. 5.36: Comparison between the hysteresis friction calculated by FEM simulation and friction measurements carried out using water (top) and water + 5% soap (bottom). Compounds A and H tested over Granite and Brick with 3 bar contact pressure and 20°C.

Despite some discrepancy, the overall trend of the friction curves predicted by the FEM is anyway in agreement with the measurements, especially for water + soap case. Therefore, in agreement with other literature data, it has been confirmed that water-soap mixtures are useful to have experimental measurements mainly related to hysteresis [131] [71] [132]. In case of pure water, as per Persson hypothesis the bias between the simulation and the

experimental results could be related to dewetting phenomena. This means, that, when water is present at the interface, it is not possible to determine a universal contribution of the hysteresis to wet friction, as it might depend on substrate, compound, velocity and temperature.

5.3.4.1. *Friction master curves for dry and hysteresis friction*

All measurements and simulation carried out so far were done considering a temperature of 20°C. In principle simulation, under isothermal conditions, can be performed for any temperature, as long as the material properties can be defined for those chosen temperature. Hence, it was decided to reproduce the friction curve for 60°C temperature so that FEA methods could be validated even for a situation where the material exhibits completely different properties. The material parameters required for modeling have been defined in the same way like for 20°C models; that means, quasi-static behavior combined with viscoelastic mastercurves. The difference in the new simulation is that 60° temperature was adopted as a reference temperature. For the following investigation only compound A and the granite surface have been taken into account.
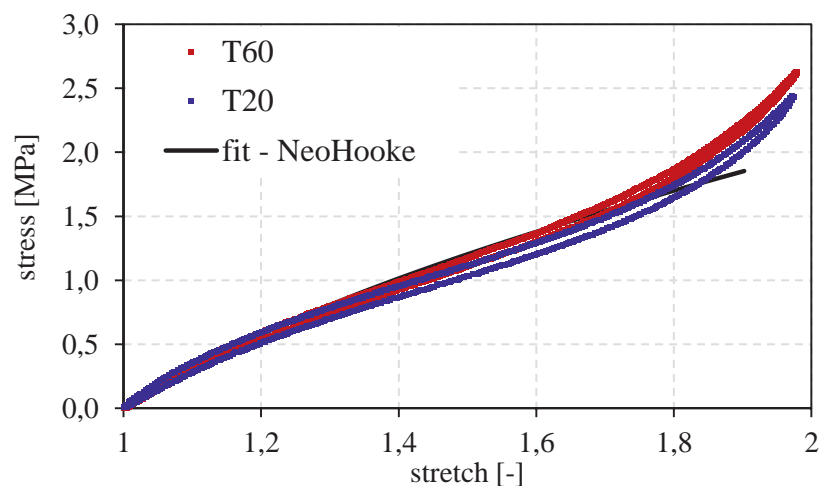
Fig. 5.37: Stress-strain test at 20°C and 60°C under uni-axial mode, crossbar speed 5 mm/min. The Neo-Hooke model has been used to fit the 60°C test with $C_{10} = 0.57$.

The quasi-static behavior is not changing that much when temperature is changed from 20 °C to 60 °C, as shown in Fig. 5.37. The fitting of Neo-Hooke model with the experimental

stress-strain curve has been optimized up to 60% strain, in line with the expected larger strain.

The viscoelastic behavior has been again fitted again using the Prony series in frequency domain. Comparing the mastercurves calculated for 60°C and 20°C, a shifting to higher frequency of the values is observed. The plot in Fig. 5.38 shows in a clear way the difference between two temperatures and the fitting of the 60°C mastercurve. The applied WLF shifting factors are shown in Fig. 5.39.
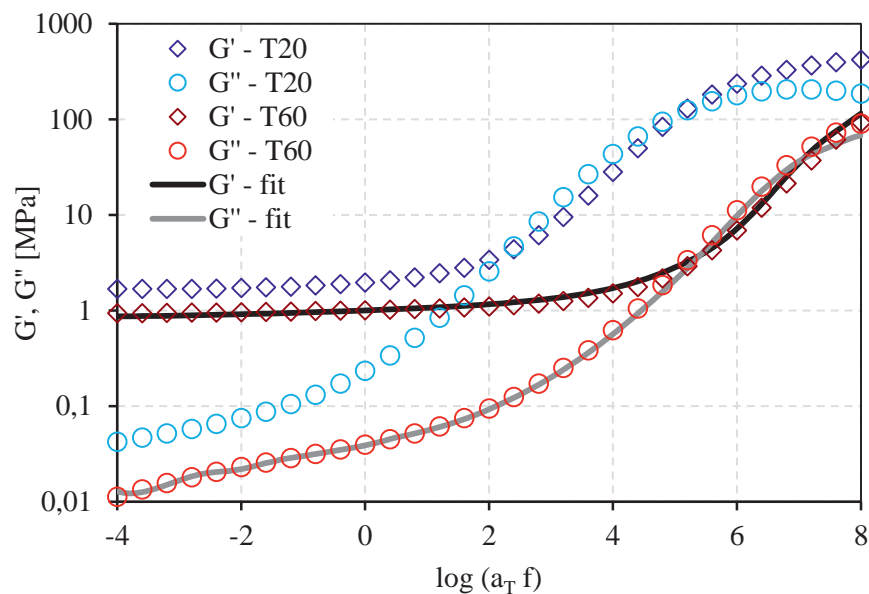
Fig. 5.38: Comparison between storage and loss modulus mastercurves of the compound A for a reference temperature of 20°C and 60°C. A Prony series with 70 elements has been used for the fitting of the 60°C curves.

Once the set of material parameters was obtained, it has been possible to calculate the hysteresis friction coefficient over 4 velocity decades, applying 3 bar of nominal contact pressure. The resulting friction curve is shown in Fig. 5.40, and compared with the experimental points, measured using a mixture of water and soap, at both 60°C and 20°C. Besides a small underestimation of the measured values, the hysteresis friction prediction performed by ABAQUS turned out to be quite accurate. Comparing the friction behavior obtained for 20°C and 60°C, a reduction of the friction values takes place at higher temperature as expected, due to more elastic behavior (or equivalently less dissipative). In fact, keeping in mind the viscoelastic nature of hysteresis friction, widely demonstrated in

the previous sections, it is clear that the shifting of the viscoelastic mastercurves to higher frequencies implies a shifting of the friction curve to higher velocities.
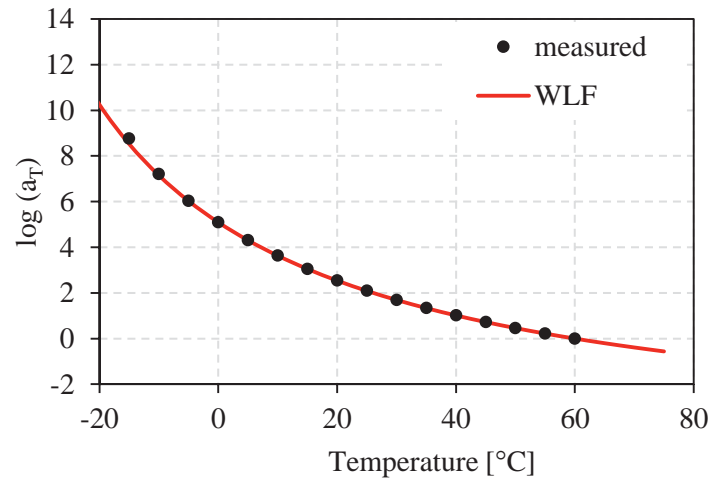
Fig. 5.39: Comparison between the WLF function and the shifting factors applied for the mastercurve of Fig. 5.38, with 60°C reference temperature. Coefficients to use for WLF: C1= 5.03; C2 = 119.3.
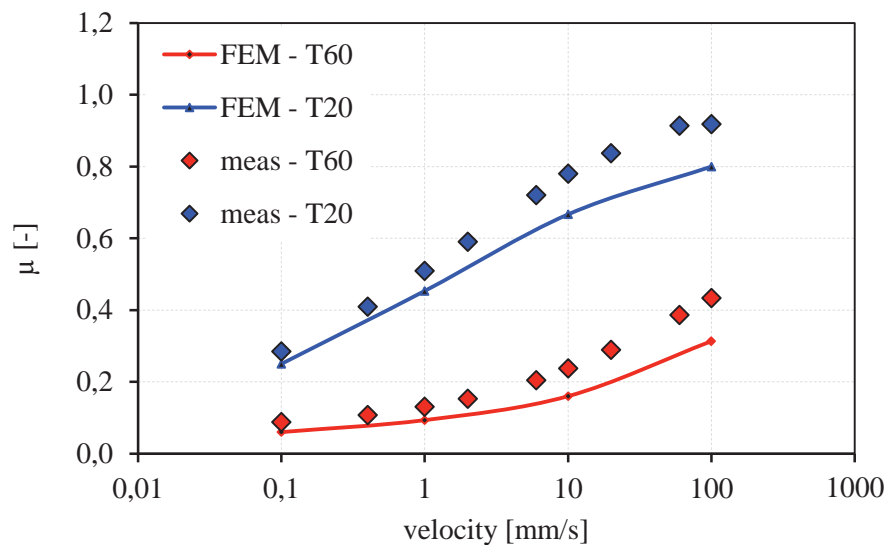
Fig. 5.40: Comparison between measurement (water + soap) and hysteresis friction calculated by FEM for 20°C and 60°C, compound A with a nominal contact pressure of 3 bar.

For this reason, it has been possible to construct a friction mastercurve by shifting the isothermal friction segments along the velocity axis according to the WLF coefficients retrieved by dynamic mechanical measurements of Fig. 5.39 [117] [74] [133]. This procedure allows extrapolating the friction coefficient in a velocity range which is outside

the machine range but interesting for several applications, like tire braking. Applying the WLF shifting factors to the curves of Fig. 5.40 a smooth and continuous curve is obtained, see Fig. 5.41. As it is possible to see, the FEM simulation was submitted also for very high velocity (450 and 3000 mm/s) in case of 60 °C. The overlapping of the high speed-60°C points with the low speed-20°C values proves the capability of FEM to predict the friction coefficient trend over the whole mastercurve range. Still from mastercurves of Fig. 5.41, it is possible to observe the strong change hysteresis friction undergoes with the sliding velocity. In particular, at very slow velocities (<1 mm/s) and high temperature, the higher elastic behavior and the reduced frequency of excitation produce a friction coefficient of about 0.2. On the other side, for high velocity (> 1 m/s) and 20°C the material finds itself a condition close to the glass transition, so in a very dissipative state, thus producing a μ between 0.7 and 0.9. It is worth to remember that the considerations carried out so far deal with the hysteresis component of the friction coefficient and so just the measurements performed using water and detergent have been shown.
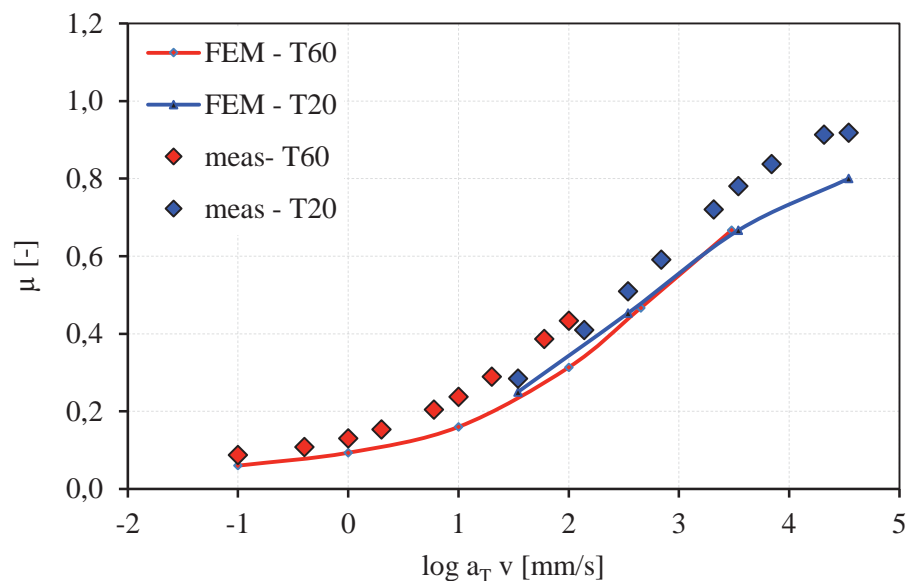
Fig. 5.41: Comparison between measured and FEM calculated friction mastercurve.

The principle of the time-temperature superposition was applied to reconstruct the mastercurve also for dry measurements, as shown in Fig. 5.42. The difference between the dry measurements and the water+soap is usually interpreted as adhesive friction, under the assumption that dry friction raises only from hysteresis and adhesion. Therefore a fitting of the dry master curve has been performed summing up to the hysteresis friction, calculated

111

by FEM, the analytical formulation of Eq. (20), which describes the adhesive component according to Le Gal and Klüppel model [83]. The result, shown in Fig. 5.42, was obtained using the following fitting parameters for the adhesive part: $\tau_{s0} = 13$kPa, $v_c = 10$ mm/s. The ratio E_∞/E_0 was set equal to 296, according to the measured G' mastercurve, and always from the mastercurve the relaxation time spectra has been calculated so that the exponent n could have been estimated. Besides some differences, regarding the investigated velocity range, the comparison with Le Gal simulations of Fig. 5.42 shows strong analogies. In fact, in both cases SBR compounds and rough granites have been used but in the current investigation 60°C temperature, instead of 20°C, was chosen as reference temperature and data have been extrapolated through master curve at larger speeds. From the model point of view, the main difference is that the ratio between real and nominal contact area, A_c/A_0, has been estimated according to the method described in literature, while analytical formulations were used by Le Gal and that the hysteresis friction is directly predicted by ABAQUS, so no fitting parameters are anymore required like in case of analytical models [134][73]. The difference between measurement and calculation in dry conditions may be related from the underestimation of the hysteresis calculation compared with the lubricated conditions.

Nevertheless, the capability of the models to describe rubber friction confirmed the widespread idea that the overall friction can be considered, with good approximation, as the sum of hysteresis and adhesion [71][135].
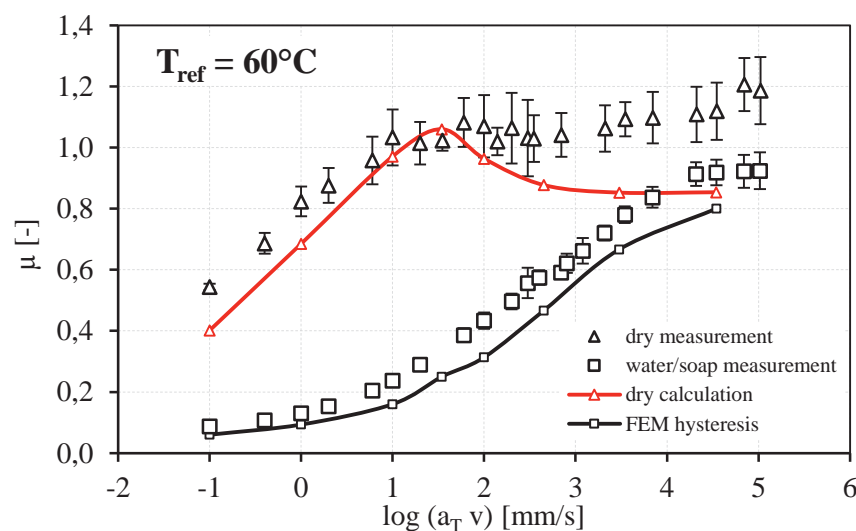
Fig. 5.42: FEM calculation of dry and hysteresis friction master curves in case of compound A and rough granite at $T_{ref} = 60$°C. The dry friction is calculated summing up the hysteresis friction calculated by FEA and the adhesion analytical model.
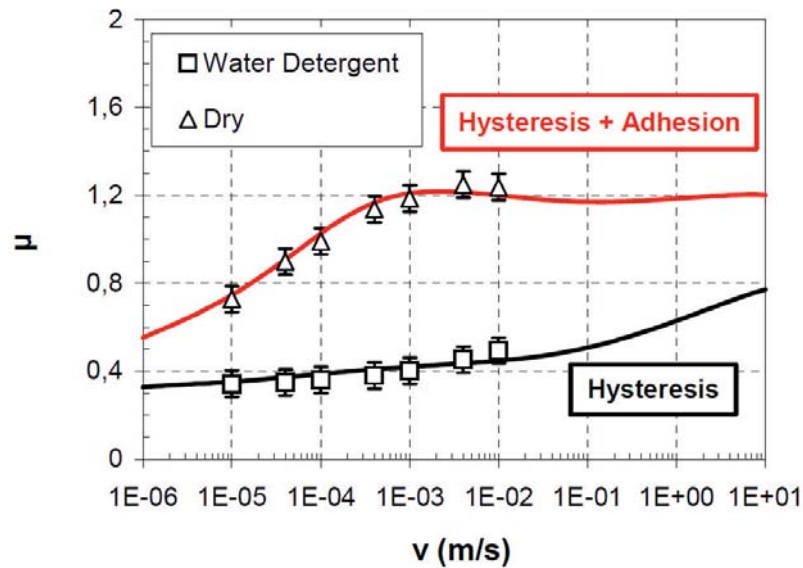
Fig. 5.43: Friction simulations and measurements of SBR rubber and rough granite at 20°C, from Le Gal [73] [85].

Analogously to Le Gal and Persson studies, the adhesive contribution alone can also be calculated, see Fig. 5.45, based on contact area and interfacial shear strength contributions (Fig. 5.44). Considering adhesive fiction given by the product of A_c/A_0 and τ_s, it is clear that for low speeds small adhesion is observed, because of small interfacial shear strength. On the other side, for high speeds the decrease of real contact area for more than one decade causes a strong reduction of friction as well, besides the fact that the shear strength reaches its maximum.
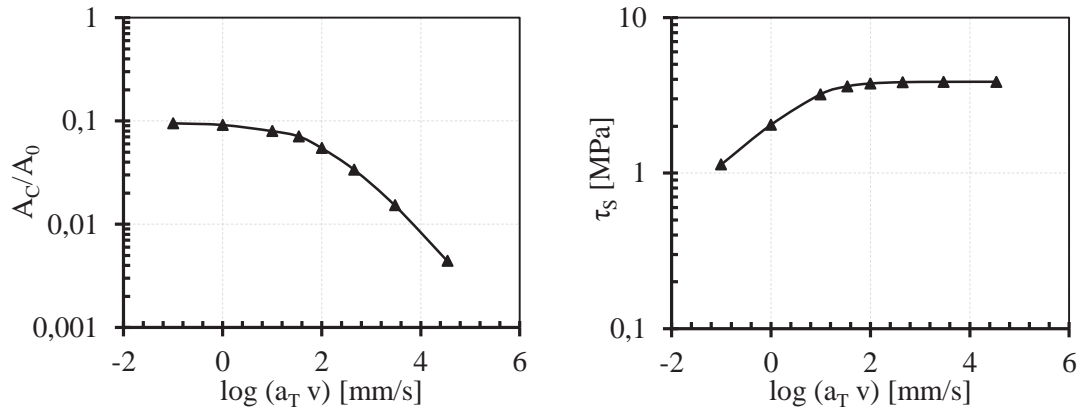
Fig. 5.44: Ratio between real and nominal contact area as a function of the sliding velocity (left); interfacial shear strength as a function of the velocity (right).
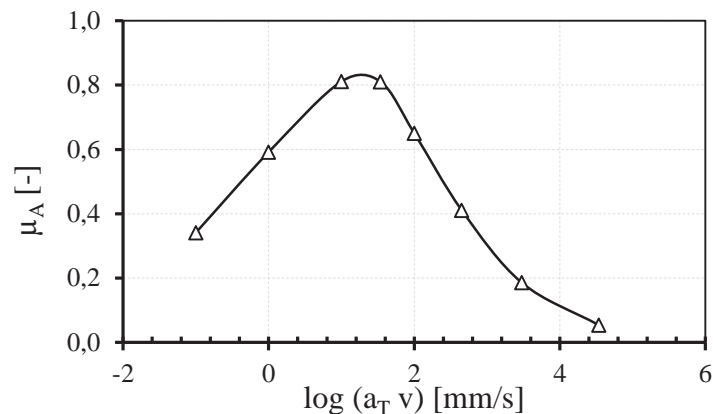
Fig. 5.45: Adhesive friction in case of the compound A sliding over granite at 3 bar nominal contact pressure, for a temperature of 60°C.

Once adhesive and hysteresis friction are both known, their relative contribution to the overall friction for the investigated velocity range can be estimated. Fig. 5.46 shows that in low velocity range, $v < 10$ mm/s, adhesion is dominant, while for velocities larger than 1 m/s hysteresis is mainly responsible for the friction resistance. It is reasonable to expect higher adhesive contribution at slow sliding velocities, because of the larger contact area, while as the sliding velocity increases, the hysteresis contribution becomes larger and larger due to the more frequent and stronger excitation exerted by the substrate's roughness. Nevertheless, the adhesion contribution at high speeds is probably underestimated because a too high contact area reduction is observed in case of ABAQUS simulations if compared with the previously mentioned analytical models. In any case, the exact distinction between the above mentioned velocity ranges cannot be generally valid because, as seen, it strongly depends on compound, substrate and temperature, taken into examination.
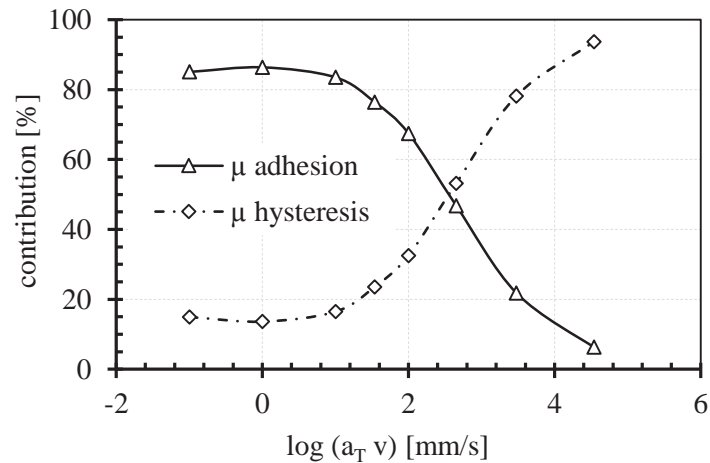
Fig. 5.46: Contribution of adhesive and hysteresis friction to the overall friction, referring to Fig. 5.42.

Although thanks to time-temperature superposition it is possible to estimate the friction coefficient over a broad velocity range, it should be noted that this approach is valid only under isothermal assumption. In case of real applications, where the sliding velocity can be higher than 100 mm/s, significant amount of mechanical energy is dissipated, or to be more precise, is converted into heat and therefore temperature increases could take place in the rubber body. Since viscoelastic properties are strongly dependent on temperature, it could happen that the friction coefficient undergoes strong changes compared to the isothermal case. In the following section this topic will be further discussed and a preliminary estimation of temperature increase will be provided in case of both sinusoidal and rough substrates.

5.4.   Estimation of heat build-up during wet friction

The frictional energy, produced during sliding of a rubber block on rigid asperities, is mainly converted into heat. In case of dry friction, at high enough sliding velocity, low thermal conductivity of rubber and short contact time lead to negligible heat diffusion and therefore temperature increases are observed [136] [137]. If a lubricant is present at the contact interface, such as water, the work expended by the asperities to deform rubber would still cause energy dissipation, but the high thermal diffusivity of the liquid medium will cool down the system. Hence, in order to estimate in a proper way the temperature increase generating during wet friction, besides the dissipated energy density distribution, also the heat transfer between rubber and liquid medium should be taken into analysis.

For the calculation of heat build-up generating in the sample during wet friction, an infinite heat transfer coefficient was considered and the local energy dissipation was assumed to be exponential, on the basis of the FEM simulation results. These assumptions allowed to find a solution for the heat flow differential equation presented in [138] for the case of semi-infinite solid with heat generated within it:

$$\frac{\partial^2 T}{\partial y^2} - \frac{1}{\kappa}\frac{\partial T}{\partial t} + \frac{\dot{Q}}{K} = 0 \tag{62}$$

Where T is the temperature, expressed as a function of the time, t, and space, y; $\dot{Q}$ is the rate of heat production per unit time and volume, κ is the thermal diffusivity and K the thermal conductivity. Assuming the heat production rate to be exponential like, $Q = Q_0\, e^{-\alpha y}$ and that the surface is kept at constant temperature, the following boundary condition apply:

$$T = const = 0 \text{ at } y = 0 \tag{63}$$

The resulting increase ΔT is then equal to:

$$\Delta T = -\frac{Q_0}{K\alpha^2}\, erf\,\frac{y}{2\sqrt{\kappa t}} + \frac{Q_0}{K\alpha^2}\left\{1 - e^{-\alpha y} + \frac{1}{2}e^{\kappa\alpha^2 t - \alpha y}\, erfc\left[\alpha\sqrt{\kappa t} - \frac{y}{2\sqrt{\kappa t}}\right] - \frac{1}{2}e^{\kappa\alpha^2 t + \alpha y}\, erfc\left[\alpha\sqrt{\kappa t} + \frac{y}{2\sqrt{\kappa t}}\right]\right\} \tag{64}$$

Thanks to ABAQUS simulations it was possible to compute the local distribution of the dissipated energy density in the sample for any time during the sliding regime. In order to determine the rate of dissipated energy density, w, the increase of dissipated energy gained during a certain sliding time was divided by the time frame itself. Such operation has been performed for the case of sinusoidal surface, as well as for the granite substrate, for both 10 mm/s and 100 mm/s sliding velocity.

The trend of the dissipated energy density along the vertical sample direction turned out to be exponential like. Hence the exponential function $Q_0 \, e^{-\alpha y}$ has been used to fit such trend giving an R² of about 0.9. Assuming the whole amount of energy loss to be converted into heat generation, it has then been possible to quantify the parameters, Q_0 and α, necessary to determine the heat rate production and solve the thermal equation.

The values used for thermal diffusivity and thermal conductivity have been taken from literature measurements performed on similar SBR based compounds [139] $\kappa = 1.46 \times 10^{-7}$ m²/s, $K = 0.232$ W/mK. The temperature increase expected to take place during sliding, because of hysteresis friction, has been calculated and it is shown in Fig. 5.47. The plot shows that in case of sliding over the granite substrate the temperature increase is less than 1°C and the steady state is reached in about 20 seconds. In case of the multi-indenter the temperature evolution is different. Indeed, higher temperature increase is observed and the steady state is reached for time longer than 100 seconds. The same procedure performed for a sliding velocity of 10 mm/s showed no temperature increase, in line with literature results [136]. Of course this is a simplified solution because the energy dissipation rate is assumed to be constant with the sliding time, while in the real case an iterative calculation, which considers the change of material properties due to sample temperature variation, should be performed.
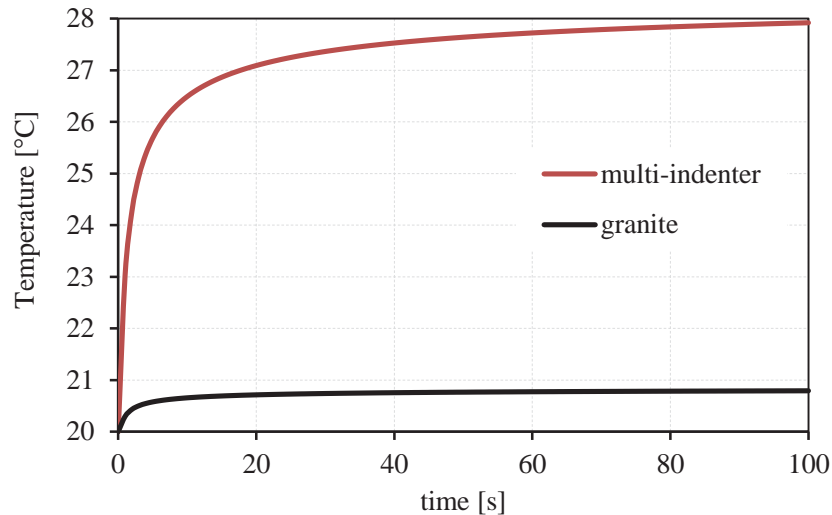
Fig. 5.47: Evolution of specimen temperature increase due to hysteresis during sliding
friction. The sliding velocity is 100 mm/s.

However, in order to validate the theoretical calculations presented so far, IR thermal camera measurements have been carried out in order to determine the specimen temperature during sliding friction tests. The camera was positioned in front of the specimen substrate assembly and the rubber block temperature has been recorded while moving the substrate, as shown in Fig. 5.48. It is worth to point out that the measurements have been carried out using a thin film of liquid at contact interface so that heat build-up deriving from dry friction interactions could be avoided.

Fig. 5.48: Experimental set-up for the IR thermal camera measurements during sliding
friction.

The acquired images, shown in Fig. 5.49, demonstrate that, at least qualitatively, the measured heat build-up is in line with the theoretical estimation. In fact, as predicted by the theoretical model, in case of 10 mm/s negligible temperature increase is observed for both

118

granite and multi-indenter surface; while for 100 mm/s sliding speed the sample shows higher temperature increase when sliding over the multi-indenter than the granite.
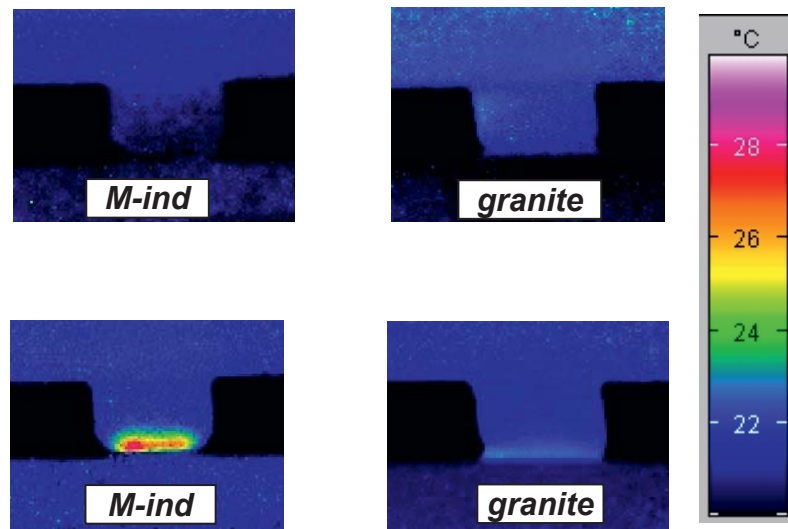
Fig. 5.49:   IR pictures of samples during sliding at 10 mm/s (top) and 100 mm/s (bottom).

The maximum temperatures reached at the steady state have been quantified thanks to the IR pictures and compared with the theoretical estimation. The chart illustrated in Fig. 5.50 shows that, despite the simplifications adopted for the theoretical model, the heat build-up calculation turned out to be realistic and quite close to the measured one. This means, that in some cases a certain amount of sliding time is required to see relevant temperature effects and that, anyway, if a lubricant is present the temperature increase is limited compared with dry cases [137] [140].
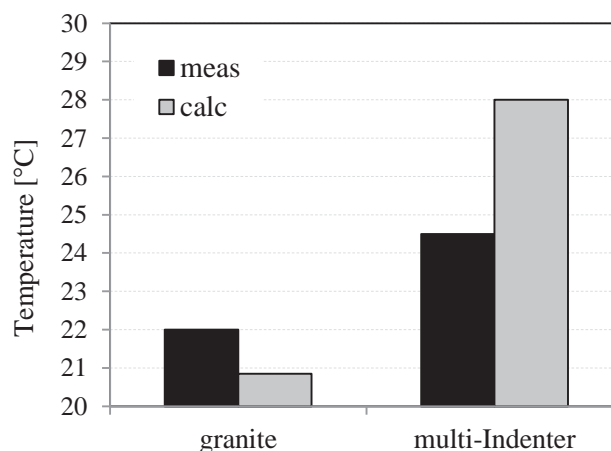
Fig. 5.50:   Comparison between temperature increases measured by IR-camera and calculated by theoretical model. Sample A sliding at 100 mm/s.

6. Summary and conclusions

The main topic of the thesis was the investigation of contact mechanics and friction, with a particular interest in the fundamental interactions occurring between rubber and rough rigid substrates during sliding. According to the state of the art, rubber friction has been treated as a sum of adhesion and hysteresis. The latter contribution was mainly investigated by use of both specific experimental tests and finite element models, in order to gain a deeper understanding of the mechanisms originating hysteresis friction.

Starting from the basics of rubber friction, in the first part of the work, Grosch studies have been retraced, so that his widely accepted theories could be experimentally validated. More specifically, friction measurements have been carried out using wavy regular substrates with different geometries and, in order to minimize the adhesive contribution, a lubricant has been used. The velocity dependence of the friction coefficient showed a correlation with the rubber compounds dynamic mechanical properties, thus confirming the viscoelastic nature of hysteresis friction. In particular, according to Grosch hypothesis, a correspondence, between the excitation frequency of a dynamic test and the one exerted by the asperities during friction, could be found considering sliding velocity and asperity distance.

The connection between bulk viscoelasticity and friction properties is also confirmed by experiments carried out using the dual layer samples. These specifically designed samples, consisting of two different co-vulcanized rubber layers, showed that, contrary to the most materials, where only surfaces are important for contact problems, bulk properties play a relevant role in rubber friction. In particular, the rougher the substrate the thicker will be the layer of material involved. Moreover, an advanced optical image correlation technique was used to detect the deformation induced by the indenters in the sample. Simplified estimations, performed combining the optical analysis with viscoelastic measurements, confirmed hysteresis to be caused by dissipative mechanisms, although the system resolution turned out to be a limiting parameter for a comprehensive investigation.

A finite element model (FEM) was then developed to investigate the friction problem. A visco-hyperelastic material model, based on the generalized Maxwell model, has been used to evaluate hysteresis friction. The model was built with no tangential interaction between rubber and substrate, so that the pure contribution coming from hysteresis could be

investigated. The finite element analysis (FEA) performed for several model compounds sliding over model wavy substrates confirmed the experimental findings and the strong connection between viscoelasticity and friction. Based on the realistic prediction provided by FEA, a preliminary study on the substrate geometry effects has been carried out. Model sinusoidal substrates have been designed with a systematic variation of asperity distance and height. Besides the aspect ratio of the asperities also the superposition of two sinusoids has been studied. The simulations show that the asperity distance is mainly responsible for the shifting of the friction peak along the velocity axis, while the ratio height to distance rules the amount of friction. If substrates with a different length scale are superposed, the friction curve becomes a mixture of the single substrates, resulting in a broader distribution of the friction coefficient as a function of the sliding velocity. How exactly the friction value is affected by the different scales is still an area of investigation which could be explored in future works. One possibility could be to perform dedicated measurements which validate the correlation between friction and geometrical parameters of the superposed substrates.

In order to investigate the pure hysteresis contribution in case of substrates with complex textures, FEA simulations have been also performed for friction on rough surfaces. The substrate has been modelled as a rigid profile in a two dimensional model. The FEM friction prediction turned out to be in line with the measurements carried out under lubrication, confirming, through experimental evidences, the hysteresis friction theory also for rough surfaces. In addition, the FEM simulation could be submitted for a speed range higher than the equipment capability under isothermal conditions. The friction coefficient calculated at high velocities could be reproduced by the experimental results applying the time-temperature superposition, namely, the shifting of the friction curves according to the WLF parameters retrieved from dynamic mechanical measurements. The overlapping obtained between the data measured at high velocities and high temperature with the points measured at low velocities and low temperature confirmed the validity to construct friction mastercurve, as highlighted from other authors. Of course the accuracy of the simulations is highly dependent on the material parameters adopted for the FEM, which must be determined through complex modelling fitting procedure. As a result, the reproducibility of the measurements has been achieved only for those compounds showing reduced nonlinearity and accompanied by a consequential smaller error on the fitting procedure. Future investigations might consider the improvement of the material model currently used

which, being valid only for linear viscoelasticity and small strains, has difficulties in replicating some real applications.

Besides lubricated measurements, also dry friction measurements have been carried out, to verify the overall friction to be given by the sum of adhesion and hysteresis. The adhesion term, formulated following the contact theory developed by Klüppel/Heinrich and validated by Le Gal, was taken into consideration to reproduce a fit example of the overall dry friction coefficient. The agreement observed with the literature results, confirmed the validity of the FEM simulations developed in the current work, which has the advantage to predict the hysteresis contribution without the necessity to fit experimental friction data. Moreover, compared to previous literature results, the velocity range considered for the comparison between measurements and model prediction has been widely extended, thanks to the friction mastercurve procedure. However, it is worth to point out that the adhesion model still requires two fitting parameters and therefore the dry friction cannot be predicted yet. Further investigations on surface energy effects on adhesion mechanisms would certainly be helpful to reach a deeper understanding of the interfacial shear strength which is included in the adhesion friction theory.

In conclusion the heat build-up produced during hysteresis friction has been for the first time estimated using an analytical model which uses input parameters deriving from FEA. The model is based on the assumption that the whole amount of dissipated energy is converted into thermal energy, resulting in a temperature increase of the rubber specimen. In agreement with the flash temperature theory from Persson, the calculations show that such temperature increase can vary depending on the sliding velocity. In particular, heat build-up occurs only for sliding velocities larger than 10 mm/s, even if the liquid present at the interface is cooling down the rubber surface compared with dry conditions. Experimental measurements carried out using IR technology confirmed the temperature increase predicted by the theoretical approach formulated in the present work. This means, that in future works, coupled thermo-mechanical models, capable to calculate iteratively the material properties change due to temperature increase, might be necessary if high sliding speeds need to be simulated.

APPENDIX

The list of the Prony series parameters used for the material model implemented in FEA are listed in the tables below.

Table 7: Prony series parameters for compound A and B

ID elem.	A		B	
	g_i	τ_i	g_i	τ_i
1	1,39E-05	1,00E+05	1,37E-05	1,00E+05
2	1,03E-05	5,92E+04	1,35E-05	5,92E+04
3	1,58E-05	3,50E+04	1,32E-05	3,50E+04
4	1,55E-05	2,07E+04	1,27E-05	2,07E+04
5	1,48E-05	1,23E+04	1,20E-05	1,23E+04
6	1,41E-05	7,26E+03	1,07E-05	7,26E+03
7	1,13E-05	4,29E+03	7,55E-06	4,29E+03
8	1,24E-05	2,54E+03	6,96E-06	2,54E+03
9	8,80E-06	1,50E+03	5,57E-06	1,50E+03
10	9,49E-06	8,90E+02	6,40E-06	8,90E+02
11	8,10E-06	5,27E+02	8,63E-06	5,27E+02
12	9,42E-06	3,12E+02	9,43E-06	3,12E+02
13	1,06E-05	1,84E+02	1,19E-05	1,84E+02
14	1,18E-05	1,09E+02	1,13E-05	1,09E+02
15	1,29E-05	6,46E+01	1,34E-05	6,46E+01
16	1,39E-05	3,82E+01	1,24E-05	3,82E+01
17	1,48E-05	2,26E+01	1,50E-05	2,26E+01
18	1,58E-05	1,34E+01	1,29E-05	1,34E+01
19	1,71E-05	7,92E+00	1,51E-05	7,92E+00
20	1,87E-05	4,69E+00	1,69E-05	4,69E+00
21	2,06E-05	2,77E+00	1,83E-05	2,77E+00
22	2,29E-05	1,64E+00	1,93E-05	1,64E+00
23	2,54E-05	9,71E-01	2,04E-05	9,71E-01
24	2,83E-05	5,75E-01	2,20E-05	5,75E-01
25	3,23E-05	3,40E-01	2,38E-05	3,40E-01
26	3,69E-05	2,01E-01	2,60E-05	2,01E-01
27	4,30E-05	1,19E-01	2,83E-05	1,19E-01
28	4,99E-05	7,05E-02	3,08E-05	7,05E-02
29	6,15E-05	4,17E-02	3,35E-05	4,17E-02
30	7,61E-05	2,47E-02	3,73E-05	2,47E-02
31	9,38E-05	1,46E-02	4,13E-05	1,46E-02
32	1,19E-04	8,64E-03	4,60E-05	8,64E-03
33	1,47E-04	5,12E-03	5,09E-05	5,12E-03
34	1,93E-04	3,03E-03	5,94E-05	3,03E-03
35	2,64E-04	1,79E-03	6,93E-05	1,79E-03
36	3,63E-04	1,06E-03	8,08E-05	1,06E-03
37	5,01E-04	6,27E-04	9,66E-05	6,27E-04
38	7,07E-04	3,71E-04	1,13E-04	3,71E-04
39	1,00E-03	2,20E-04	1,39E-04	2,20E-04
40	1,36E-03	1,30E-04	1,76E-04	1,30E-04
41	2,05E-03	7,69E-05	2,27E-04	7,69E-05
42	2,95E-03	4,55E-05	3,00E-04	4,55E-05
43	4,26E-03	2,69E-05	4,11E-04	2,69E-05
44	6,22E-03	1,59E-05	5,76E-04	1,59E-05
45	8,98E-03	9,43E-06	7,98E-04	9,43E-06

46	1,15E-02	5,58E-06	1,17E-03	5,58E-06
47	1,53E-02	3,30E-06	1,68E-03	3,30E-06
48	2,22E-02	1,96E-06	2,38E-03	1,96E-06
49	2,21E-03	1,16E-06	3,33E-03	1,16E-06
50	8,50E-02	6,85E-07	4,57E-03	6,85E-07
51	4,42E-03	4,05E-07	6,22E-03	4,05E-07
52	6,43E-04	2,40E-07	9,36E-03	2,40E-07
53	1,41E-02	1,42E-07	1,61E-02	1,42E-07
54	1,20E-04	8,40E-08	2,29E-03	8,40E-08
55	1,31E-01	4,97E-08	6,08E-02	4,97E-08
56	1,76E-04	2,94E-08	4,87E-03	2,94E-08
57	3,56E-05	1,74E-08	6,48E-04	1,74E-08
58	6,83E-04	1,03E-08	1,27E-02	1,03E-08
59	5,27E-02	6,09E-09	1,20E-04	6,09E-09
60	4,91E-03	3,61E-09	1,83E-01	3,61E-09
61	1,35E-02	2,13E-09	1,76E-04	2,13E-09
62	2,32E-01	1,26E-09	3,56E-05	1,26E-09
63	6,77E-02	7,47E-10	6,83E-04	7,47E-10
64	8,23E-03	4,42E-10	6,54E-02	4,42E-10
65	3,01E-05	2,62E-10	4,85E-03	2,62E-10
66	2,98E-05	1,55E-10	1,20E-02	1,55E-10
67	3,01E-01	9,16E-11	2,90E-01	9,16E-11
68	1,75E-04	5,42E-11	1,07E-01	5,42E-11
69	6,91E-05	3,21E-11	7,86E-03	3,21E-11
70	6,81E-05	1,90E-11	3,01E-05	1,90E-11
71	1,01E-05	1,12E-11	2,98E-05	1,12E-11
72	2,21E-04	6,65E-12	1,97E-01	6,65E-12
73	2,28E-04	3,94E-12	1,75E-04	3,94E-12
74	1,37E-04	2,33E-12	6,91E-05	2,33E-12
75	1,37E-04	1,38E-12	6,81E-05	1,38E-12
76	1,37E-04	8,15E-13	1,01E-05	8,15E-13
77	1,37E-04	4,83E-13	2,21E-04	4,83E-13
78	1,37E-04	2,86E-13	2,28E-04	2,86E-13
79	1,37E-04	1,69E-13	1,37E-04	1,69E-13
80	1,37E-04	1,00E-13	1,37E-04	1,00E-13

Table 8:   Prony series parameters for compound S and H

	S		H	
# elem.	g_i	τ_i	g_i	τ_i
1	6,07E-04	1,00E+05	8,48E-04	1,00E+04
2	4,45E-04	5,86E+04	4,56E-04	5,67E+03
3	4,74E-04	3,44E+04	4,49E-04	3,22E+03
4	2,73E-11	2,02E+04	6,81E-04	1,82E+03
5	6,20E-04	1,18E+04	1,31E-04	1,03E+03
6	5,75E-04	6,93E+03	5,42E-04	5,86E+02
7	4,67E-04	4,06E+03	2,64E-05	3,33E+02
8	5,87E-04	2,38E+03	7,25E-04	1,89E+02
9	3,07E-04	1,40E+03	3,01E-04	1,07E+02
10	8,01E-05	8,19E+02	2,95E-04	6,06E+01
11	1,49E-05	4,80E+02	6,70E-04	3,44E+01
12	6,49E-05	2,81E+02	6,82E-05	1,95E+01
13	2,04E-04	1,65E+02	8,24E-04	1,11E+01
14	3,92E-04	9,67E+01	1,02E-04	6,27E+00
15	8,81E-04	5,67E+01	7,27E-04	3,55E+00

124

16	5,97E-04	3,33E+01	1,94E-04	2,02E+00
17	3,58E-04	1,95E+01	7,83E-04	1,14E+00
18	3,95E-04	1,14E+01	4,83E-05	6,48E-01
19	8,77E-04	6,70E+00	9,96E-04	3,68E-01
20	2,64E-05	3,93E+00	2,32E-04	2,08E-01
21	2,28E-03	2,30E+00	6,84E-04	1,18E-01
22	2,00E-04	1,35E+00	3,76E-04	6,70E-02
23	4,63E-04	7,92E-01	6,05E-04	3,80E-02
24	1,04E-03	4,64E-01	3,28E-04	2,15E-02
25	3,87E-04	2,72E-01	8,37E-04	1,22E-02
26	9,53E-04	1,60E-01	6,17E-05	6,93E-03
27	7,14E-04	9,35E-02	9,95E-04	3,93E-03
28	4,04E-04	5,48E-02	3,44E-04	2,23E-03
29	1,05E-03	3,22E-02	3,73E-04	1,26E-03
30	6,48E-04	1,89E-02	1,20E-03	7,16E-04
31	6,90E-04	1,11E-02	5,28E-05	4,06E-04
32	9,10E-04	6,48E-03	1,12E-03	2,30E-04
33	8,89E-04	3,80E-03	5,97E-04	1,31E-04
34	8,14E-04	2,23E-03	1,03E-03	7,41E-05
35	9,35E-04	1,31E-03	8,79E-04	4,20E-05
36	1,29E-03	7,66E-04	1,31E-03	2,38E-05
37	9,24E-04	4,49E-04	1,53E-03	1,35E-05
38	1,46E-03	2,63E-04	1,92E-03	7,66E-06
39	1,29E-03	1,54E-04	1,63E-05	4,34E-06
40	2,04E-03	9,05E-05	8,02E-03	2,46E-06
41	1,82E-03	5,30E-05	6,19E-04	1,40E-06
42	2,39E-03	3,11E-05	1,17E-03	7,92E-07
43	1,94E-03	1,82E-05	1,38E-02	4,49E-07
44	5,72E-03	1,07E-05	3,69E-03	2,55E-07
45	2,49E-03	6,27E-06	1,81E-02	1,44E-07
46	2,62E-03	3,68E-06	3,77E-03	8,19E-08
47	1,07E-02	2,15E-06	3,37E-02	4,64E-08
48	2,14E-03	1,26E-06	1,46E-05	2,63E-08
49	9,67E-03	7,41E-07	5,74E-02	1,49E-08
50	1,29E-02	4,34E-07	1,31E-04	8,46E-09
51	1,03E-02	2,55E-07	7,73E-02	4,80E-09
52	1,47E-02	1,49E-07	4,67E-04	2,72E-09
53	1,90E-02	8,75E-08	9,92E-02	1,54E-09
54	1,95E-02	5,13E-08	3,53E-04	8,75E-10
55	1,42E-02	3,01E-08	1,21E-01	4,96E-10
56	2,08E-02	1,76E-08	4,52E-02	2,81E-10
57	3,42E-02	1,03E-08	7,16E-05	1,60E-10
58	3,60E-02	6,06E-09	1,08E-02	9,05E-11
59	1,32E-02	3,55E-09	2,47E-01	5,13E-11
60	2,30E-02	2,08E-09	1,44E-01	2,91E-11
61	4,55E-02	1,22E-09	6,73E-02	1,65E-11
62	7,46E-03	7,16E-10	9,35E-03	9,35E-12
63	1,72E-02	4,20E-10	1,36E-05	5,30E-12
64	4,63E-03	2,46E-10	4,53E-04	3,01E-12
65	1,66E-01	1,44E-10	4,50E-04	1,71E-12
66	1,03E-02	8,46E-11	4,47E-04	9,67E-13
67	1,76E-02	4,96E-11	4,45E-04	5,48E-13
68	3,51E-02	2,91E-11	4,44E-04	3,11E-13
69	4,06E-02	1,71E-11	4,44E-04	1,76E-13
70	3,71E-01	1,00E-11	4,44E-04	1,00E-13

125

Bibliographic references

[1]   F. P. Beer and R. Johnston, Vector Mechanics for Engineers (Sixt ed.), McGraw-Hill, 1996.

[2]   J. L. Meriam and L. G. Kraige, Engineering Mechanics (fifth ed.), John Wiley & Sons, 2002.

[3]   R. C. Hibbler, Engineering Mechanics (Eleventh ed.), Pearson, Prentice Hall, 2007.

[4]   H. Tanaka and A. Kageyu, "Structure and Biosynthesis Mechanisms of Natural-cis-Polyisoprene," *Rubber Chem. Tech.,* no. 56, p. 299, 1983.

[5]   G. Bristow, "Mastication of Elastomers," *Trans. IRI,* no. 38, pp. 29,104, 1962.

[6]   A. Roberts, Natural Rubber, Science and Technology, New York, Kuala Lampur: Oxford University Press, 1988.

[7]   W. J. Mc Gill and D. A. Joosk, "A Theory of Green Strength in Natural Rubber," in *Rubber con '87*, Harrogate, GB, 1987.

[8]   D. S. Campbell and K. N. G. Fuller, "Factors Influencing the Mechanical Behavior of Raw Unfilled Natural Rubber," *Rubber Chem. Technol.,* no. 57, p. 104, 1984.

[9]   P. C. Killgoar jr., M. A. Lemieux and R. J. Tabar, "A low Modulus, High Fatigue Life Elastomer Compound for Suspension Applications," *Rubber Chem. Technol.,* no. 54, p. 347, 1981.

[10]   P. B. Lindley and A. Stevenson, "Fatigue Resistance of Natural Rubber in Compression," *Rubber Chem. Technol.,* no. 55, p. 337, 1982.

[11]   D. E. Wingrove, *Natural Rubber, Neoprene, Ethylene-Propylene-Diene Blends in White Sidewall Compounds,* Chicago: 122nd ACS-Meeting, Rubber Div., 1982.

[12]   G. Kraus and J. T. Gruver, "Rheological Properties of Cis-Polybutadiene," *J. Appl. Polym. Sci.,* no. 9, p. 739, 1965.

[13]   R. Casper, J. Witte and G. Kuth, *Syntheticher Kautschuk,* Weinheim: Ulmann's Encyklopädie der technischen Chemie, 4h Ed., Vol. 13 Verlag Chemie, 1977.

[14]   E. F. Engel, "International Institute of Synthetic Rubber Producer - Annual Meeting," Munich, 1972.

[15]   H. E. Adams et al., "The Impact of Lithium Initiators on the Preparation of Synthetic Rubbers," *Rubber Chem. Technol.,* no. 45, p. 1252, 1982.

[16]   R. H. Campbell and R. H. Wise, "Vulcanization," *Rubber Chem. Technol.,* no. 37, pp. 635-649, 1964.

[17]   W. Hofmann, Vulcanizing and Vulcanizing Chemicals, New York: MacLaren London-Palmerton, 1967.

[18]   M. Porter: in: N. Kharash (Ed), "Mechanisms of Reactions of Sulfur Compounds," *Interscience Res. Foundation, Santa Monica,* vol. 3, p. 145, 1968.

[19]   M. Amin, H. Osman and E. Abdel-Bary, "Effect of Some Vulcanizing Systems on the Electrical Conductivity of Butadiene Rubber," *Kautschuk Gummi Kunststoffe,* no. 35, p. 1049, 1982.

[20] T. Kempermann, "The Relationship between Heat Build-up and the Chemistry of Crosslinking Systems," *Rubber Chem. Technol.,* no. 55, p. 391, 1982.

[21] D. Parkinson, Reinforcement of Rubbers, London: Monograph IRI, Lakeman and Co., 1957.

[22] G. Kraus, Reinforcement of Elastomers, New York: Inerscience Publ., 1965.

[23] J. A. C. Harwood and A. R. Payne, *Rubber Chem. Technol.,* no. 43, pp. 6,687, 1970.

[24] E. M. Dannenberg, "The Effects of Surface Chemicals Reactions on The Properties of Filler Reinforced Rubbers," *Rubber Chem. Technol.,* no. 48, pp. 410-444, 1975.

[25] R. G. Mancke, R. A. Dickie and J. O. Ferry, *J. Polym. Sci.,* vol. 6, no. 2, p. 162, 1968.

[26] P. De Gennes, Scaling Concepts in Polymer Physics, Ithaca: Cornell University Press, 1979.

[27] M. Doi and S. F. Edwards, The Theory of Polymer Dynamics, New York: Oxford University Press, 1986.

[28] M. Rubinstein and R. Colby, Polymer Physics, New York: Oxford University Press, 2003.

[29] P. J. Flory, Principles of Polymer Chemistry, Ithaca, NY: Cornell University Press, 1953.

[30] L. R. G. Treloar, Physics of Rubber Elasticity, Oxford University Press, 1975.

[31] L. H. Sperling, Introduction to Physical Polymer Science, 2nd Ed., USA: John Wiley & Sons, Inc., 1992.

[32] C. M. Blow, Rubber Technology And Manufacture, London: Butterwonns, 1971.

[33] J. D. Ferry, Viscoelastic Properties of Polymers, 3rd Ed., New York: Wiley & Sons, 1980.

[34] A. V. Tobolsky, Properties and Structures of Polymers, New York: John Wiley & Sons, 1960.

[35] A. N. Gent, "Mechanical Properties of Rubber," in *The Pneumatic Tire*, The National Highway Traffic Safety Administration, 2005, pp. 65-67.

[36] W. M. Hess and W. K. Klamp, "The Effect of Carbon Black and Other Compounding Variables on Tire Rolling Resistance and Traction," *Rubber Chem. Technol.,* no. 5, p. 390, 1986.

[37] D. Moore, The Friction of Pneumatic Tires, Amsterdam: Elsevier Scientific Pub. Co., 1975.

[38] N. McCrum and C. Buckley, Principles of Polymer Engineering, 2003, pp. 117-176.

[39] N. W. Tschoegl, The Phenomenological Theory of Linear Viscoelastic Behavior, Berlin: Springer, 1989.

[40] J. C. Maxwell, "On The Dynamical Theory of Gases," *Philos. Trans. R. Soc.,* no. 157, pp. 49-88, 1980.

[41] T. H. Courtney, Mechanical Behavior of Materials, Waveland Press Inc., 2005.

[42] E. Wiechert, "Gesetze der Elastischen Nachwirkung für Constante Temperatur," *Annalen der Physik,* no. 286, pp. 335–348, 546–570, 1893.

[43] J. Ferry, Viscoelastic Properties of Polymers, New York: John Wiley & Sons, 1960.

[44] D. Gutierrez-Lemini, Engineering Viscoelasticity, Springer, 2013.

[45] R. Young and P. Lovell, Introduction to Polymers (2 ed.), Nelson Thornes, 1991.

[46] W. J., Properties And Behavior of Polymers, John & Sons, 2012.

[47] D. E. Hall and J. C. Moreland, "Fundamentals of Rolling Resistance," *Rubb. Chem. Technol.,* vol. 3, no. 525, p. 74, 2000.

[48] S. Mihara, Reactive Processing of Silica-Reinforced Tire Rubber New Insight into The Time And Temperature Dependance of Silica Rubber Interaction, University of Twente, Enschede, NE: PhD Thesis, 2009.

[49] K. H. Nordsiek, "The Integral Rubber Concept - an Apprach to an Ideal Tire Tread Rubber," *Kautschuk Gummi Kunststoffe,* vol. 38, no. 3, 1985.

[50] L. R. Evans and J. D. MacIsaac, "Effects of Tire Rolling Resistance Levels on Traction, Treadwear, and Vehicle Fuel Economy," *NHTSA Tire Fuel Efficiency Consumer Information Program Development,* 2009.

[51] M. Williams, R. Landel and J. Ferry, "The Temperature Dependance of Relaxation Mechanism in Amorphous Polymers and Other Glass-Forming Liquids," *J. Am. Chem. Soc.,* vol. 77, no. 20, pp. 3701-3706, 1955.

[52] R. G. and E. F. T. White, "The Yield Beahvior of Glassy Polymers," in *The Physics of Glassy Polymers (R. N. Haward ed.), Chapt. 3*, London, Applied Science Publishers, 1972.

[53] A. R. Payne, "The Role of Hysteresis in Polymers," in *Reinforcement of Elastomers (Kraus G.) Chapter 3*, New York, Interscience Publisher, 1965, pp. 36-49.

[54] A. R. Payne, *Rubber Plast. Age,* vol. 42, no. 963, 1961.

[55] L. Mullins, *Rubber Chem. Technol.,* vol. 21, pp. 281-300, 1948.

[56] F. Bueche, *J. Appl. Polym. Sci.,* vol. 4, pp. 107-114, 1961.

[57] E. M. Dannenberg, *Rubber Chem. Technol.,* vol. 48, p. 410, 1975.

[58] Z. Rigbi, *Adv. Polym. Sci.,* vol. 36, p. 21, 1980.

[59] G. R. Hamed and S. Hatfield, "On the Role of Bound Rubber in Carbon-Black Reinforcement," *Rubber Chem. Technol.,* vol. 62, pp. 143-156, 1989.

[60] J. A. C. Harwood and A. R. Payne, "Stress Softening in Natural Rubber Vulcanizates. Part III. Carbon black-filled Vulcanizates," *J. Appl. Polym. Sci.,* vol. 10, no. 2, pp. 315-324, 1966.

[61] L. Mullins, in *Reinforcement of Elastomers (Kraus G. ed.)*, New York London Sidney, Interscience Publishers, 1965.

[62] B. N. J. Persson and M. Scaraggi, "On the transition from boundary lubrication to hydrodynamic lubrication in soft contacts," *Journal of Phys. Condens. Matter,* vol. 21, no. 18, 185002, 2009.

[63] H. W. Kummer, "Unified Theory of Rubber and Tire Friction," *State University Engineering Res. Bullet in B-94,* 1966.

[64] J. A. Greenwood and D. Tabor, "The Friction of Hard Sliders on Lubricated Rubber: The Importance of Deformation Losses," *Proceedings of The Physical Society,* vol. 71, no. 6, pp. 989-1001, 1958.

[65] K. A. Grosch, "The Relation between Friction and Visco-Elastic Properties of Rubber," *Proc. R. Soc. Lond.,* no. 274, pp. 21-39, 1963.

[66] E. Fina, P. Gruber and R. S. Sharp, "Hysteretic Rubber Friction: Application of Persson's Theories to Grosch's Experimental Results," *Journal of Appl. Mech,* vol. 12, no. 81, 121001, 2014.

[67] Y. Beautru and M. Kane, "Influence of Road Surface Microtexture on Thin Water Film Traction," in *7th International Conference on Maintenance and Rehabilitation of Pavements and Technological Control*, France, 2012.

[68] T. J. Goda, "Effect of Track Roughness Generated Micro-hysteresis on Rubber Friction in Case of (apparently) Smooth Surfaces," *Tribology International,* no. 93, pp. 142-150, 2016.

[69] B. Persson and O. Albohr, "On the Nature of Surface Roughness With Application to Contact Mechanics, Sealing, Rubber Friction and Adhesion," *Journal of Phys.: Condens. Matter,* no. 17, pp. 1-62, 2005.

[70] G. W. Flintsch, I. L. Al-Qadi, V. J. C. A. and R. Davis, "Effect of HMA Properties on Pavement Surface Characteristics," in *Pavement Evaluation Conference*, Roanoke, Virginia, 2002.

[71] B. N. J. Persson, "Theory of Rubber Friction and Contact Mechanics," *Journal of Chem. Phys.,* vol. 8, no. 115, pp. 3840-3843, 2001.

[72] M. Klüppel and G. Heinrich, "Rubber Friction on Self-affine Road Tracks," *Rubber Chem. Technol.,* vol. 73, no. 4, pp. 578-606, 2000.

[73] A. Le Gal, "Investigation and Modelling of Rubber Stationary Friction on Rough Surfaces," PhD dissertation, Leibniz University of Hannover, 2007.

[74] B. Lorenz, B. N. J. Persson, G. Fortunato, M. Giustiniano and F. Baldoni, "Rubber Friction for Tire Tread Compound on Road Surfaces," *Journal of Phys. Condens. Matter,* no. 25, 095007, 2013.

[75] W. M. W. Derjaguin and Y. Toporov, "Effects of Contact Deformations on The Adhesion of Particles," *J. Colloid Interface Sc.,* no. 53, pp. 314-326, 1975.

[76] K. Kendall, "Rolling Friction and Adhesion between Smooth Solids," *Wear,* no. 33, pp. 351-358, 1975.

[77] M. Barquins and D. Wehbi, "Study of Adherence of Elastomers by Cyclic Unloading Experiments," *Journal of Adhesion,* vol. 20, pp. 55-74, 1986.

[78] J. Charmet, D. Vallet and M. Barquins, "Surface and Bulk Properties in Adherence of Elastic-Viscoelastic Solids," *ACS symposium,* Chapt. 3, pp. 42-65, 2009.

[79] X. H. Shi and Y. P. Zaho, "Comparison of Various Adhesion Contact Theories and the Influence of Dimensionless Load Parameter," *Journal of Adhesion Science and Technology,* vol. 18, no. 1, pp. 55-68, 2004.

[80] P. De Gennes, "Soft Adhesives," *Langmuir,* no. 12, pp. 4497-4500, 1996.

[81] A. N. Gent and A. J. Kinloch, *J. Polym. Sci.,* vol. 9, no. 652, p. 171, 1971.

[82] B. N. J. Persson and E. A. Brener, "Crack Propagation in Viscoelastic Solids," E71, 036123 2005.

[83] A. Le Gal and M. Klüppel, "Investigation and Modelling of Adhesion Friction on Rough Surfaces," *Kautschuk Gummi Kunststoffe,* no. 59, pp. 308-315, 2006.

[84] R. A. Schapery, *Tire Sci. Technol.,* vol. 3, no. 6, p. 98, 1978.

[85] A. Le Gal and M. Klüppel, "Investigation And Modeling of Rubber Stationary Friction on Rough Surfaces," *Journal of Phys. Condens. Matter,* no. 20, 015007, 2008.

[86] J. Reinelt and P. Wriggers, "Multi-scale Approach for Frictional Contact of Elastomers on Rough Rigid Surfaces," *Lecture notes in applied and computational mechanics: Elastomer Friction,* vol. 51, pp. 53-94, 2010.

[87] K. Falk and M. Kaliske, "Multiscale Rubber Friction Homogenization for Rough Surfaces," in *Constitutive Models for Rubber IX*, Prague, 2015, pp. 99-105.

[88] P. Wagner and P. Wriggers, "Multiscale FEM Approach for Hysteresis of Rubber on Rough Surfaces," *Comput. Methods Appl. Mech. Engrg.,* no. 296, pp. 150-168, 2015.

[89] J. Altenbach and H. Altenbach, Einführung in die Kontinuumsmechanik, Stuttgart: Teubner, 1994.

[90] G. A. Holzapfel, Nonlinear Solid Mechanics: A Continuum Approach for Engineering, Chichester: John Wiley & Sons, 2000.

[91] R. S. Rivlin, "Large Elastic Deformations of Isotropic Materials.," *Proceedings of the Royal Society of London. Series A,* no. 240, pp. 459-508, 1948.

[92] R. S. Rivlin, "Large Strain Deformations of Isotropic Materials," *Transactions of Royal Society of London Series A,* no. 241, p. 379, 1948.

[93] F. T. Wall, "Statistical Thermodynamics of Rubber," *Journal of Chem. Phys.,* no. 10, p. 485, 1942.

[94] L. R. G. Treloar, "Stress-strain Data for Vulcanised Rubber Under Various Types of Deformation," *Transactions of the Faraday Society,* vol. 40, p. 59, 1944.

[95] R. W. Ogden, "Nearly isochoric elastic deformations: application to rubber like solids," *Journal of the Mechanics and Physics of Solids,* no. 26, pp. 37-57, 1978.

[96] E. M. Arruda and M. C. Boyce, *MIT Internal Report. available through Boyce M.C,* 1991.

[97] E. M. Arruda and M. C. Boyce, "A Three-Dimensional Constitutive Model for the Large Stretch Behavior of Rubber Elastic Materials," *Journal of the Mechanics and Physics of Solids,* no. 41, p. 389, 1993.

[98] O. H. Yeoh, "Characterization of Elastic Properties of Carbon Black Filled Rubber Vulcanizates," *Rubber Chem. Technol.,* no. 63, pp. 792-805, 1990.

[99] O. H. Yeoh, "Some Forms of the Strain Energy Function for Rubber," *Rubber Chem. Tech.,* vol. 66, p. 754, 1993.

[100] M. Kaliske and H. Rothert, "Formulation and Implementation of Three-dimensional Viscoelasticity at Small and Finite Strains," *Computational Mechanics,* vol. 19, pp. 228-239, 1997.

[101] S. M. Goh, M. N. Charalambides and J. G. Willimas, "Determination of the Constitutive Constants of Non-Linear Viscoelastic Materials," *Mechanics of Time-Dependent Materials,* vol. 8, no. 3, pp. 255-268, 2004.

[102] J. Ciambella, M. Destrade and R. Ogden, "On the Abaqus FEA Model of Finite Viscoelasticity," *Rubber Chem. Technol.,* vol. 82, no. 24, pp. 184-193, 2009.

[103] P. M. Mohd Afandi, "Visco-Hyperelastic Model for Soft Rubber-like Materials," *Sains Malaysiana,* vol. 43, no. 3, pp. 451-457 , 2014.

[104] O. Zienkiewicz and R. Taylor, The Finite Element Method, London: McGraw-Hill Co., 1989.

[105] P. Seshu, Textbook of Finite Element Analysis, PHI Learning Private Limited, 2003.

[106] Simulia, ABAQUS Theory Manual, ch. 2.2.1, 2009.

[107] Simulia, ABAQUS Analysis User Manual, 29.2.1.

[108] B. I. 37, *Determination of Tensile Stress-strain Properties,* 2005.

[109] ARAMIS, *User Manual v6.1, GOM GmbH.*

[110] A. Le Gal, X. Yang and M. Klüppel, "Evaluation of Sliding Friction and Contact Mechanics of Elastomers Based on Dynamic-mechanical Analysis," *J. Chem. Phys. ,* no. 123, 014704, 2005.

[111] J. J. Aklonis and W. MacKnight, Introduction to Polymer Viscoelasticity, 2nd ed., New York: Wiley-Science, 1983.

[112] A. J. Marzocca, S. Cerveny and J. Mendez, "Some considerations concerning the dynamic mechanical properties of cured styrene–butadiene rubber/polybutadiene blends," *Polym Int,* no. 49, pp. 216-222, 2000.

[113] C. Roland and C. A. Trask, *Rubber Chem. Technol.,* no. 62, p. 896, 1989.

[114] R. H. Schuster, H. M. Issel and V. Peterseim, *Rubber Chem. Technol.,* no. 69, p. 769, 1996.

[115] N. Tokita, *Rubber Chem. Technol.,* no. 50, p. 292, 1977.

[116] R. Joseph, K. E. George, D. J. Francis and K. Thomas, *Int. J. Polym. Mater.,* no. 12, p. 53, 1987.

[117] L. Busse, I. Boubakri and M. Klüppel, "Friction Master Curves for Elastomers Sliding on Granite in Simulation Compared to Experiment at Various Temperatures," *Kautschuk Gummi Kunststoffe,* vol. 64, no. 5, pp. 35-39, 2011.

[118] B. Lorenz, B. N. J. Persson and S. Dieluweit, "Rubber friction: Comparison of theory with experiment," *Eur. Phys. J. E,* no. 34, p. 129, 2011.

[119] M. Y. El-Sherbiny, A. T. Hasouna and A. W. Y., "Friction Coefficient of Rubber Sliding Against Flooring Materials," *Journal of Engineering and Applied Science,* vol. 7, no. 1, pp. 121-126, 2012.

[120] B. N. J. Persson, U. Tartaglino, E. Tosatti and O. Albohr, "Rubber Friction on Wet Rough Substrates at Low Sliding Velocity: The Sealing Effect," *Kautschuk Gummi Kunststoffe,* no. 10, pp. 532-537, 2004.

[121] K. H. Nordsiek, "The Integral Rubber Concept - an Approach to an Ideal Tire Tread Rubber," *Kautschuk Gummi Kunststoffe,* vol. 38, no. 3, pp. 178-185, 1985.

[122] M. J. Wang, *Rubber Chem. Technol.,* no. 71, p. 520, 1997.

[123] J. M. Bennett and L. Mattsson, Introduction to Surface Roughness and Scattering, Optical Society of America, 1989, pp. 1-33.

[124] J. Takadoum, Materials and Surface Engineerng in Tribology, John Wiley & Sons, 2013.

[125] M. Lee, Remarkable Natural Material Surfaces and Their Engineering Potential, Springer International Publishing, 2014.

[126] B. Bhushan, Introduction to Tribology, John Wiley & Sons, 2013.

[127] V. L. Popov, L. Li, Y. S. Chai and M. Popov, "Generalized law of friction betweeen elastomers and differently shaped rough bodies," *Sci. Rep.,* vol. 4, p. 3750, 2014.

[128] S. Wang, "Effects of Surface Roughness on Sliding Friction in Lubricated-Point Contacts: Experimental and Numerical Studies," *Journal of Tribology,* no. 129, p. 809, 2007.

[129] R. Stribeck, "Ball Bearings for any Loads," *Zeitschrift Des Vereins Deutscher Ingenieure,* no. 45, pp. 73-79, 1901.

[130] R. Striebeck, "Article on the Evaluation of Ball-Bearings," *Zeitschrift Des Vereins Deutscher Ingenieure,* no. 45, pp. 1421-1422, 1901.

[131] A. D. Roberts, *Journal of Physics,* vol. 4, p. 423, 1971.

[132] A. Lang and M. Klüppel, "Hysteresis and Adhesion Friction of Carbon Based Elastomer Nanocomposites: Theory, Experiment and Applications," in *Constitutive Models for Rubber VIII*, London, Tailor & Francis group, 2013, pp. 59-64.

[133] A. Le Gal, L. Guy, G. Orange, Y. Bomal and M. Klüppel, "Modelling of Sliding Friction for Carbon Black and Silica Filled Elastomers on Road Tracks," *Wear,* no. 264, pp. 606-615, 2008.

[134] L. Busse, A. Le Gal and M. Klüppel, "Modelling of Dry and Wet Friction of Silica Filled Elastomers on Self-Affine Road Surfaces," in *Lecture Notes in Applied Computational Mechanics, no. 51, Elastomere Friction*, Springer, 2010, pp. 1-26.

[135] A. Lang and M. Klüppel, "Modelling Predictions and Experimental Investigations of Rubber Friction and Tire Traction," in *4th International Tyre Colloquium*, Surrey, UK, 2015.

[136] B. N. J. Persson, "Rubber Friction: Role of The Flash Temperature," *Journal of Phys. Cond. Matter,* vol. 18, no. 32, 7789-823, 2006.

[137] G. Fortunato, V. Ciaravola, L. B. and B. Persson, "General Theory of Frictional Heating with Application to Rubber Friction," *Journal of Phys. Cond. Matter,* vol. 27, no. 8, 175008, 2015.

[138] H. S. Carslaw und J. C. Jaeger, Conduction of Heat in Solids, pp. 78-79, Oxford University Press, 1959.

[139] J. Fritzsche and M. Klüppel, "Simulation of The Internal Sample Temperature of Rubber Components During Cyclic Deformation," *Kautschuk Gummi Kunststoffe,* pp. 44-51, 6 2011.

[140] D. K. Wilborn, "A Temperature Study of Pneumatic Tires During Highway Operation," *National Technical Information Service,* 1972.

[141] J. Brandrup, E. H. Immergut and G. E. A., Polymer Handbook, John Wiley & Sons, 1988.

[142] E. Rabinowicz, Friction and wear of materials, 2nd ed., John Wiley & Sons, 1995.

[143] L. Busse and M. Klüppel, "Friction Master Curves for Rubber on Dry and Wet Granite: Experiments and Simulations," *Kautschuk Gummi Kunststoffe,* vol. 5, no. 64, p. 35, 2011.

Curriculum Vitae

Name	Gianfredo Romano
Nationality	Italy
Place and date of birth	Napoli, 02 December 1988

Education

2013 - 2016	Ph.D. student – Mechanical engineering
	D.I.K. e.V. and Leibniz Universität, Hannover
2010 – 2012	M. Sc. - Materials engineering
	Università degli studi di Napoli Federico II, Napoli
2007 – 2010	B. Sc. – Materials science and engineering
	Università degli studi di Napoli Federico II, Napoli